FEASIBILITY STUDY OF SEDIMENTARY ENHANCED GEOTHERMAL SYSTEMS USING RESERVOIR SIMULATION

by

Jae-Kyoung Cho

A thesis submitted to the Faculty and the Board of Trustees of the Colorado School of Mines in partial fulfillment of the requirements for the degree of Master of Science (Petroleum Engineering).

Golden, Colorado

Date: _____

Signed: _____

Jae Kyoung Cho

Approved: _____

Luis E. Zerpa

Thesis Advisor

Golden, Colorado

Date: _____

Signed: _____

Erdal Ozkan

Professor and Head

Department of Petroleum Engineering

ABSTRACT

The objective of this research is to evaluate the preliminary feasibility of commercial geothermal projects, from a sedimentary reservoir with low permeability that requires productivity enhancement, using numerical reservoir simulation. The performance of a sedimentary geothermal reservoir is investigated in terms of reservoir hydraulics and thermal evolution.

To build a reliable benchmark for simulation study, validation of the numerical reservoir model with respect to an analytical model is presented, and the process to achieve an acceptable match between the numerical and analytical solutions is described. The analytical model used in this study is based on the work of Gringarten (1978), which consists of a conceptual geothermal reservoir, considering an injection and production well doublet in a homogeneous porous media. A commercial thermal reservoir simulator (STARS from Computer Modeling Group, CMG) is used in this work for numerical modeling. In order to reproduce the analytical model results, the numerical simulation model is modified to include the same assumptions of the analytical model. Simulation model parameters that make the numerical results deviate from the analytical solution, such as the grid block size, time step and no-flow boundary are identified and investigated.

An analytical tracer test model proposed by Shook (2000) is numerically modeled. This model allows us to predict the time when the temperature of the produced water decreases by capturing a tracer component at production well. Reservoir simulation models with different porosity and permeability distribution are tested to see the effects of reservoir inhomogeneity and anisotropy. In particular, premature thermal breakthrough due to the presence of high permeability streak in a reservoir model is simulated. In an effort to apply the knowledge we obtained from the analytical solutions, the effects of reservoir rock and water properties, as a function of pressure and temperature, are investigated. Especially, water density, viscosity and rock heat capacity play a significant role in reservoir performance.

The Permian Lyons formation in the Denver Basin is selected for this preliminary study. Well log data around the area of interest are collected and borehole temperature data are analyzed to estimate the geothermal potential of the target area and it follows that the target formation has a geothermal gradient as high as 72 °C/km. Based on the well log data, hypothetical reservoir simulation models are build and tested to access the hydraulic and thermal performance. It turns out that the target formation is marginally or sub-marginally commercial in terms of its formation conductivity. Therefore, the target formation may require reservoir stimulation for commercially viable power generation.

Lastly, reservoir simulation models with average petrophysical properties obtained from the well log analysis of the target formation are built. In order to account for overburden and underburden heat transfer for confined reservoirs, low permeability layers representing shale cap/bed rocks are attached to

the top and bottom of the reservoir layers. The dual permeability concept is applied to the reservoir layers to model induced fracture networks by reservoir stimulation. The simulation models are tested by changing fracture conductivity and shape factor. The results show that a balance between hydraulic and thermal performance should be achieved to meet the target flow rate and sustainability of 30 years' uninterrupted operation of geothermal electricity power generation. Ineffective reservoir stimulation could result in failing to create a producing reservoir with appropriate productivity index or causing premature thermal breakthrough or short-circuiting which advances the end of geothermal systems. Therefore, Enhanced Geothermal Systems (EGS) should be engineered to secure producing performance and operational sustainability simultaneously.

TABLE OF CONTENTS

LIST OF FIGURES

LIST OF TABLES

ACKNOWLEDGEMENT

I would like to express my deepest gratitude and appreciation to my advisor, Dr. Luis E. Zerpa for his guidance and support, and providing me with the best environment to focus on this research. I thank my thesis committee members, Dr. Alfred Eustes and Dr. Xiaolong Yin for their valuable suggestions and comments on the research. I am also thankful to the Petroleum Engineering Department staff including Denise Winn-Bower and Terri Snyder for their help.

Acknowledgements are made to Korea National Oil Corporation for the financial support. I also appreciate the Computer Modeling Group (CMG) for letting me use the CMG STARS license.

My Special thanks to Younki Cho, as my best friend, for the discussions we shared on my research and a variety of topics.

Finally, I would like to thank my family for their endless support and endurance. Thanks to my mother in Korea who is always there for me. Above all, I would like to thank my wife, Jiyoun Park who supports and encourage me all the time. Thanks to my lovely daughter and son, Yunseo and Yunseong.

CHAPTER 1
INTRODUCTION

1.1 Motivation of the Research

The motivation of this study is to evaluate the feasibility of sedimentary enhanced geothermal systems (SEGS) using numerical reservoir simulation technology. The sedimentary EGS have a great potential for energy production. Unlike conventional convection-dominated high-enthalpy systems, EGS are not limited to volcanic or tectonic areas that are less extensive than sedimentary basins in their areal dimension (Bundschuh and Arriage, 2010). MIT (MIT, 2006) reported that the US can extract 200,000 × 10^{18} Joules out of an EGS total potential of 13,000,000 × 10^{18} Joules for energy utilization.

Sedimentary formations with high temperature gradient at depths ranging from 2.0 to 6 km can be potential candidates for commercial enhanced geothermal energy production. The permeability of economically viable potential target formations at such depths is expected to be in the range of 1 mD to 100 mD. There is a wide range of variation in petrophysical properties of rock and fluid depending on geologic settings. In tight formations, fluid flow does not occur naturally at the required flow rates. In this case, reservoir enhancement techniques can be used for the creation of a reservoir, allowing the access to a huge amount of dormant energy.

Figure 1-1 shows that Colorado has a high geothermal potential. Most of the promising basins with high geothermal gradient are located in the areas where oil and gas activities are abundant (i.e., Denver basin and Raton basin). Therefore, technologies tested and proved in oil and gas industry including reservoir characterization and simulation, formation evaluation, well completion and stimulation, can be effectively applied for the development of sedimentary geothermal systems in the basins in the state of Colorado.

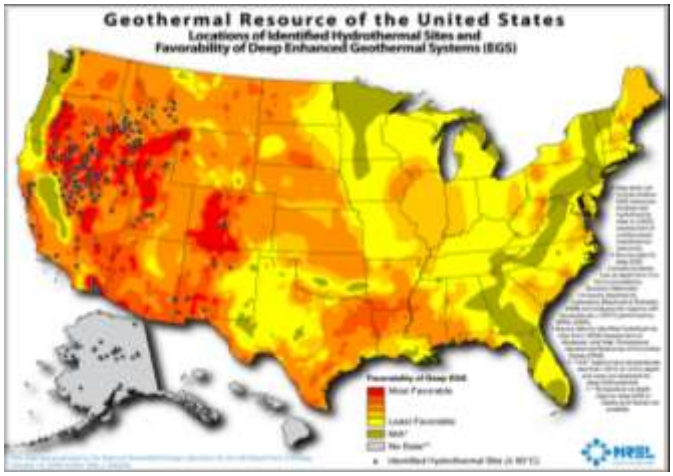

Figure 1-1 Geothermal resources of the United States (http://energy.gov/eere/geothermal/geothermal-maps).

1.2 Objectives

The purpose of this research is to evaluate the feasibility of sedimentary enhanced geothermal systems (SEGS) using numerical reservoir simulation. This study starts with comparison of an analytical solution to numerical simulation results for a conceptual geothermal doublet model. In-depth comparison of an analytical solution to numerical simulation is made to propose a benchmark for further numerical simulation study. The result of comparison applies to simulation models characterized with well log data from a potential target area. The performance of various reservoir simulation models is investigated in terms of reservoir hydraulics and thermal evolution in order to evaluate the feasibility of sedimentary geothermal systems.

Primary objectives of the research include the followings:

- Investigate thermal evolution of a geothermal doublet system using analytical models and a commercial reservoir simulator,
- Evaluate the effects of grid-size, time-step and reservoir boundary on the numerical results with respect to analytical solutions for a geothermal doublet system,
- Apply a tracer test model to predict thermal breakthrough time for a doublet system,
- Evaluate the effects of reservoir rock and fluid properties on thermal performance of a doublet system.
- Develop reservoir simulation models characterized using well log data from a target formation, to evaluate the feasibility of sedimentary geothermal systems.
- Evaluate different development schemes in terms of reservoir hydraulics and thermal performance, including vertical, horizontal wells and hydraulically fractured models,
- Evaluate the effect of induced fracture networks (or pre-existing natural fractures) on thermal and hydraulic performance.

1.3 Method of Study

A numerical reservoir simulation model representing a single doublet system is tested with respect to an analytical solution. The analytical solution predicts the thermal front breakthrough time of a doublet system in homogeneous reservoirs with constant rock and fluid properties under steady state condition. The reservoir lifetime (i.e., the time when injected cold water front reaches a production well) obtained from a numerical simulation model is compared to that of the analytical solution. As is often the case with analytic solutions, the analytical solution used in this research also involves limiting assumptions. Hence, the numerical reservoir simulation model is modified to incorporate the same assumptions in order to reproduce the results of the analytical solution. Numerical simulation models are validated with respect to the analytic

solution in terms of reservoir hydraulics and thermal evolution. To strike a balance between accuracy and computation costs, the effects of grid structure, reservoir dimension, gird block size and time-step are studied and the optimum grid configuration is proposed. The thermal breakthrough time obtained from the analytical solution is used as a benchmark against which numerical simulation models are tested to evaluate the hydraulic and thermal performance. Key reservoir parameters in geothermal reservoir engineering such as temperature gradient, porosity and permeability are obtained or simulated on the basis of the well log data. The effects of well configuration, overburden and underburden heat loss and stimulation are also discussed. The performance of each configuration in terms of hydraulics and thermal behavior is assessed with respect to the performance of a simple doublet.

CHAPTER 2
LITERATURE REVIEW

Gringarten and Sauty (1975) derived a mathematical model for predicting temperature behavior at production well for an idealized geothermal doublet – one recharging well and one production well. The mathematical formulation is derived from the partial deferential equation of heat conduction in solids (Carslaw and Jaeger, 1989). Under a potential flow theory, they applied the heat conduction equation to a flow channel bounded by two streamlines. Their formulation assumes 1) constant fluid properties including viscosity, compressibility and the product of density and heat capacity 2) an idealized reservoir of laterally infinite geometry with a constant thickness 3) instantaneous thermal equilibrium between the rock and the water 4) no thermal conduction in the horizontal direction and infinite thermal conduction in the vertical direction. The solution can be used as a design criterion for a geothermal system development since the temperature behavior at production well defines the overall system performance. For more complex well configurations, it can be used as a benchmark against which the performance of other types of well configuration is compared.

Shook (2000) proposed a mathematical model of a tracer injection test for geothermal applications. The model correlates thermal breakthrough time with injected water breakthrough time. In a trace test, a slug of tracer is carried into the reservoir with the injection stream. The tracer travels in the porous media and reaches the production well. The time when the injected tracer is captured (tracer or water breakthrough time) at the production well is directly correlated with the time when the heat front swept by the injected cold water arrives at the production well (thermal breakthrough time). The interstitial velocity and the heat front velocity has a constant ratio, which is defined as the retardation factor. The retardation factor is a function of porosity and the product of density and heat capacity of rock and water. Higher retardation factor means that the heat front velocity is become slower compared to the interstitial velocity of water. This model can be a useful tool for a field scale application of a tracer test since the thermal breakthrough time can be estimated before it actually happens. In addition, a tracer test can be used to capture anisotropic aspects of formations.

Allis et al. (2011) presented a discussion on the potential of geothermal systems in a stratigraphic reservoirs in the Western U.S. at depths of 3-5 km. They presented permeability data, obtained from oil and gas activity, of the Rocky Mountains and Great Basin of the US. They showed that a lower Paleozoic carbonate section has permeability up to 70 md while siliciclastic reservoirs have an average permeability of 30 md, both at depths of 3-5 km. This implies that such carbonate reservoir with an average permeability of 70 md could be developed with higher thermal recovery without reservoir enhancement. Moreover, it is suggested that more heat energy could be produced from the stratigraphic carbonate reservoir since the heat

sweep efficiency is higher in a stratigraphic reservoir and heat capacity of carbonate is higher than that of siliciclastic reservoirs.

Morgan (2009) discussed the geothermal potential of the Raton Basin in Colorado. Bottom-hole temperature (BHT) data, mostly from coal-bed methane extraction, were collected and analyzed. Three different correlations were used to correct the BHT recorded in well log headers. The geothermal potential was evaluated based on the thermal gradient calculated form the collected bottom-hole temperature. It was shown that the formation has the mean geothermal gradient of 49 ± 12 ^{o}C/km. In the most promising area, the formation temperature of 150 °C was expected at depth of 1600 m.

Satman (2011) investigated into the sustainability of geothermal doublets in a confined aquifer with no natural hydrothermal convection. He presented a field application study of the Lund geothermal heat pump project based on the work done by Bjelm and Alm (2010). The field application shows that the temperature decline at the producer follows the Gringaten and Sauty (1975) solution.

Butler et al. (2004) presented the results of numerical simulation of enhanced geothermal systems using a commercial simulation software package. The hypothetical simulation models incorporate the parameters obtained from the Desert Peak EGS in Nevada. The models consisted of different well patterns including a doublet, triplet and five-spot configuration. Instead of using thermal breakthrough time as a performance criterion, they tried to evaluate the performance using the net electrical power generation over the reservoir lifetime. The permeability enhancement by hydraulic fracturing was simulated using dual porosity model.

Deo et al. (2013) discussed thermal performance of sedimentary EGS using reservoir simulation. Five different simulation models were considered: sandwich, single layer, low temperature, low permeability and short circuit model. Interestingly, lower permeability model shows the best thermal performance because there is less permeability difference between the cap/bed rock and reservoir, facilitating heat transfer from the sealing units (Deo et al. 2014). This research implies that we are chasing two goals conflicting with each other: thermal and hydraulic performance. Therefore, balancing thermal and hydraulic performance is the most crucial element for successful sedimentary EGS.

Suarez and Viggiano (1992) discussed the electric potential of geothermal heat extraction. The volumetric power generation potential of a geothermal reservoir can be estimated using thermodynamic properties of the reservoir. Especially, the use of heat capacity of the fluid and rock systems results in a practical method for estimating the geothermal potential of electricity generation in terms of how many electric megawatt can be produced from geothermal systems. They proposed the energy conversion efficiency defined as the geothermal energy-electricity conversion factor. The conversion efficiency for the Los Azufres geothermal field in Mexico was proposed at around 2.5%. The conversion efficiency included reservoir heat efficiency and heat-to-electricity conversion efficiency.

Du et al. (2010) proposed using the dual porosity concept for modeling hydraulic fracturing induced fracture networks in shale gas reservoir. It was pointed out that comprehensive method incorporating stress regime, natural fractures and heterogeneity of the reservoirs is not available up to date. There are advantages using a dual porosity model compared to a conventional single grid model using gird refinement. It saves computational time and costs. It is capable of incorporating heterogeneity in petro-physical properties and Langmuir isotherm, etc. The transient behavior inside the matrix block can be captured with matrix subdivision. Taylor et al. (2014) used dual permeability numerical simulation to capture the fluid flow in hydraulic fractures and natural fractures which created or rejuvenated by fracturing treatment. Microseismic data was used to delineate a stimulated reservoir volume (SRV).

CHAPTER 3
ANALYTICAL AND NUMERICAL MODELING

This chapter discusses an analytical and numerical solution for predicting thermal behavior at production well in a geothermal doublet. This solution enables us to predict thermal breakthrough time – the time when the produced water temperature starts decreasing. Here, numerical simulation models are built to reproduce the result of the analytical solution. The numerical models incorporate the restricting assumptions that the analytical solution bases on. Comparing the numerical results to the analytical solution helps us build a benchmark against which further simulations models can be evaluated.

3.1 Analytical modeling of geothermal doublet systems

A conceptual sedimentary geothermal reservoir, consisting of an injection and production well doublet in a homogenous porous media, is considered (Figure 3-1). The performance of geothermal doublets is described by two key factors: the thermal performance of the reservoir (the time for thermal breakthrough at the production well and the temperature behavior after the thermal breakthrough time), and the pressure profile in the reservoir (the pressure drive required to maintain a desired flow rate between the injection and production wells). Gringarten (1978) discussed analytical models for both of these factors.

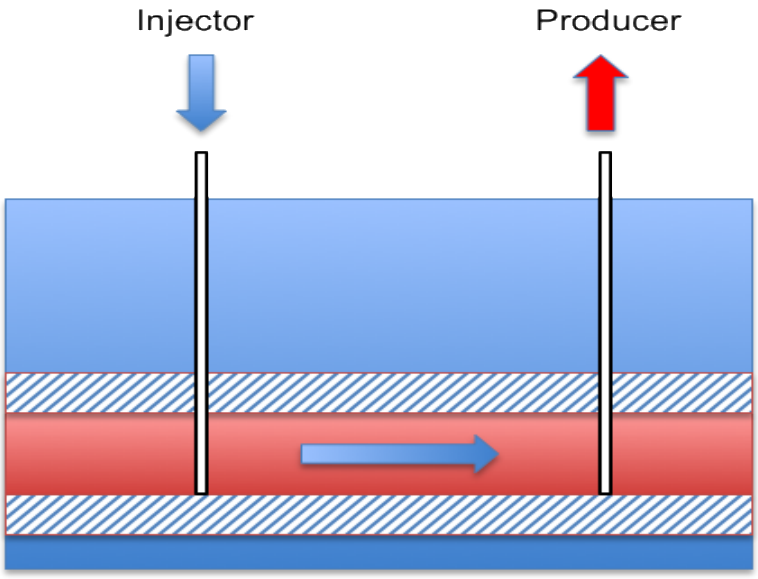

Figure 3-1 Geothermal doublet system.

The assumptions made in the derivation of the Gringarten and Sauty's analytical model are:

- Infinite horizontal aquifer with uniform thickness and constant rock and fluid properties,
- Sealed aquifer by cap/bed rocks,

- Constant injection rate equal to production rate (i.e., steady-state condition),
- Initially, rock and fluid are in thermal equilibrium at same temperature,
- Horizontal heat conduction is neglected,
- Vertical heat conduction from cap/bed rock can be considered,
- Volumetric heat capacity of water and rock are constant.

With vertical heat conduction from cap/bed rocks neglected, the time for thermal breakthrough in the geothermal doublet reservoir is described by Eq. 3.1,

$$\frac{\rho_w C_{p,w}}{\rho_a C_{p,a}} \frac{Q\Delta t}{D^2 h} = \frac{\pi}{3} \tag{3.1}$$

The pressure drive between the wells in the reservoir (or more accurately, the pressure difference between the injection and production well), is described by Gringarten (1978) as the pressure drawdown in the production well. Muskat (1946) describes how to relate the pressure difference between the wells. The result is:

$$\Delta p = \frac{\mu Q}{\pi k h} ln\left(\frac{D}{r_{well}}\right) \tag{3.2}$$

Table 3-1 Rock and fluid properties used in the base case for comparison between analytical and numerical models

Parameter	Value
Porosity, ∅	0.15
Reservoir thickness, h	50 m
Rock heat capacity, ρC_r	2,769 kJ/m^3^{o}C
Water heat capacity, ρC_w	3922.4 kJ/m^3/^{o}C
Water viscosity, μ_{avg}	0.26e-4 Pa-s
Well radius, r_{well}	0.108 m (8.5” diam.)
Reservoir lifetime, Δt	30 years

The analytical solution (Eq. 3.1) was used to calculate the well spacing required for a thermal breakthrough of 30 years (i.e., geothermal reservoir lifetime) at different production/injection flow rates. This is because commercial geothermal systems usually target at 30 years of sustainable production with the inlet temperature of a binary power plant remained within a given design range. Figure 3-2 shows the results, indicating that a well spacing from 1 to 2 km is required to meet the reservoir lifetime constraint of 30 years. It can be observed that flow rate scales with the square of well spacing, and that the reservoir lifetime is independent of formation permeability.

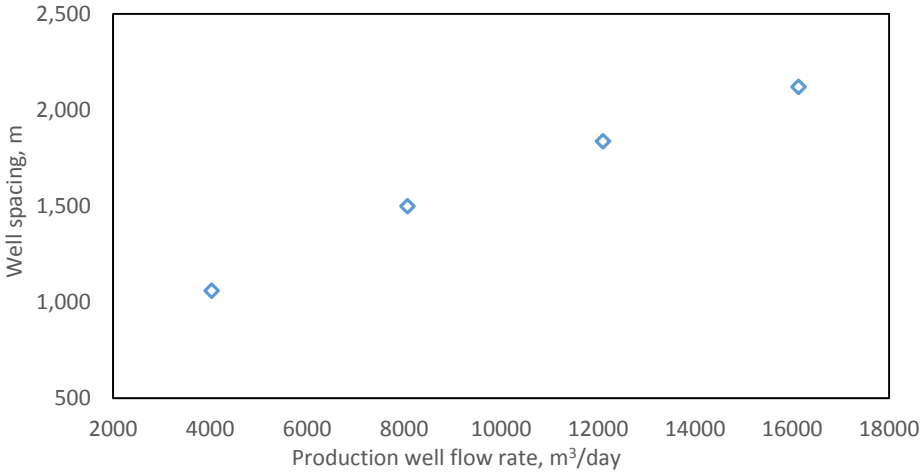

Figure 3-2 Plot of well spacing as function of production/injection flow rate, obtained using parameters presented in Table 3-1.

3.2 Numerical modeling of a geothermal doublet system

A commercial thermal reservoir simulator (STARS from Computer Modeling Group, CMG) is used in this work of numerical modeling. Figure 3-3 shows the 3-dimensional geothermal reservoir model, indicating the location of the injection/production wells. The value of the parameters used during the development of this model is listed in Table 3-2. The rock and fluid properties were defined and modified such that the numerical model reproduces the assumptions of the analytical model listed in the previous section. For example, the water properties are held constant throughout the simulation, and thermal conductivity is neglected.

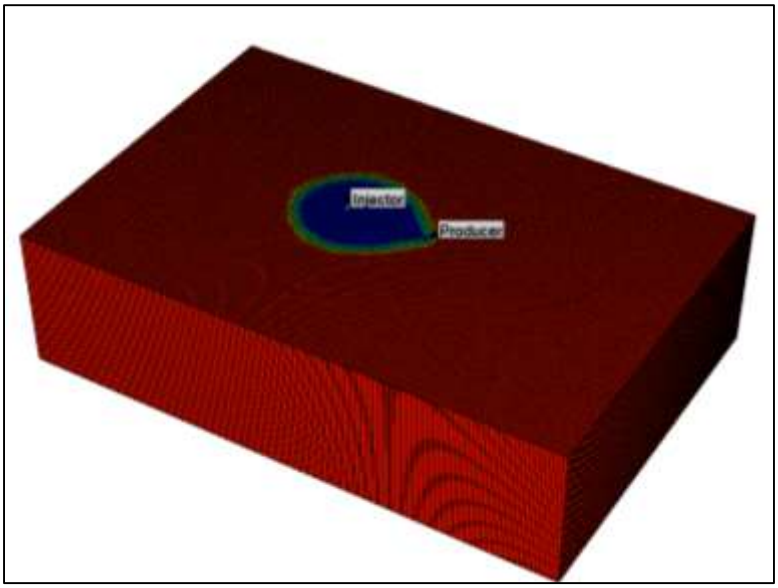

Figure 3-3 Initial numerical simulation model of a geothermal doublet system.

Table 3-2 Parameters of numerical model of the sedimentary geothermal doublet system

Grid type	Cartesian
Grid resolution (m)	10 - 10 - 50
Reservoir dimensions (m)	4500 – 3000 - 50
Top depth of reservoir (m)	3000
Porosity	0.15
Permeability I	100
Water viscosity (cp)	0.26
Water density (kg/m^3)	918.6
Volumetric Water heat capacity (kJ/m^3-K)	3922.4
Water compressibility (1/kPa)	0
Water thermal conductivity	0
Rock compressibility	0
Volumetric Rock Heat Capacity (kJ/m^3-k)	2,769
Rock thermal conductivity	0
Overburden/underburden heat loss	0
Injection/production rate (m^3/day)	8068
Reservoir Temperature (ºC)	160
Injection Temperature (ºC)	80

3.3 Comparison of analytical and numerical results

The comparison between the analytical and numerical models is made in terms of reservoir hydraulics, numerical grid-size, no-flow boundary and time-step.

3.3.1 Reservoir hydraulics

This section considers the hydraulic behavior of the reservoir in terms of productivity index PI (a measure of the production capacity of a well), which is the ratio of the flow rate to the required pressure drawdown of the production well. Since the reservoir rock is considered homogeneous, with constant properties (porosity and permeability), the numerical solution is not affected significantly by the spatial and temporal discretization (i.e., grid block size and time step) used. Also, because the constant injection rate is equal to production rate, a steady-state flow condition is achieved quickly between the pair of well within the reservoir. Using an initial simulation model (Figure 3-3) with modeling parameters listed in Table 3-2, the reservoir hydraulics in terms of average productivity index is calculated using Eq. 3.2 and is summarized in Table 3-3. Figure 3-4 shows average reservoir pressure and bottomhole pressure at each well over the entire lifetime for 100 mD case. Due to the assumptions of the model (i.e., constant rock and fluid properties, constant injection and production, etc.), the reservoir reaches a steady state condition immediately. From a series of simulation cases with different values of rock permeability, the numerical

solution approximates the analytical solution with an average absolute error lower than 5.0%, which is considered acceptable. The productivity index obtained from the numerical simulation is in good agreement with that of the analytical model with their relative error percentage less than 5 %. Figure 3-5 shows that productivity index is proportional to *kh* value which means that the more permeable the formation is, the less pressure drawdown it requires.

In addition, the numerical models adopt three different grid-size (100 × 100, 50 × 50 and 10 × 10 in meters) and two different maximum time-step (1000 and 30 in days). The reservoir hydraulics in terms of productivity index is summarized in Table 3-4. As discussed previously, the effects of grid-size and time-step on pressure are not remarkable since the reservoir model achieve a steady state quickly and assumes no compressibility.

Table 3-3 Average reservoir productivity index from the simulation and analytic model

Permeability, mD		50	100	200	400
kh, m		2500	5000	10000	20000
Numerical	Avg. Res Pressure	28502	28502	28502	28502
	Injector BHP (kPa)	44031	36264	32394	30447
	Producer BHP (kPa)	12958	20727	24608	26554
	PI (L/s-bar)	0.60	1.20	2.40	4.80
Analytical	PI (L/s-bar)	0.61	1.22	2.44	4.89
Relative error (%)		1.47	1.39	1.66	1.81

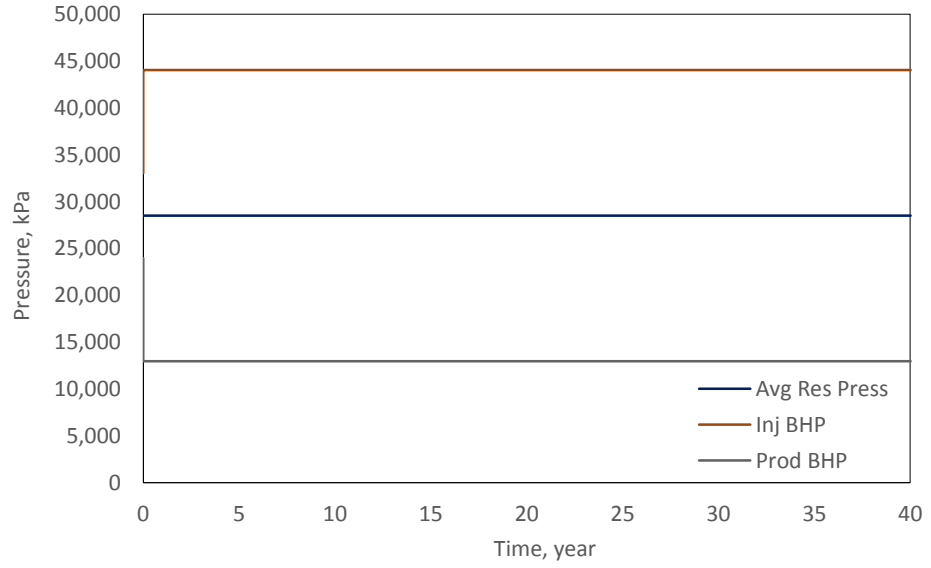

Figure 3-4 Average reservoir pressure and bottomhole pressure at injector and producer.

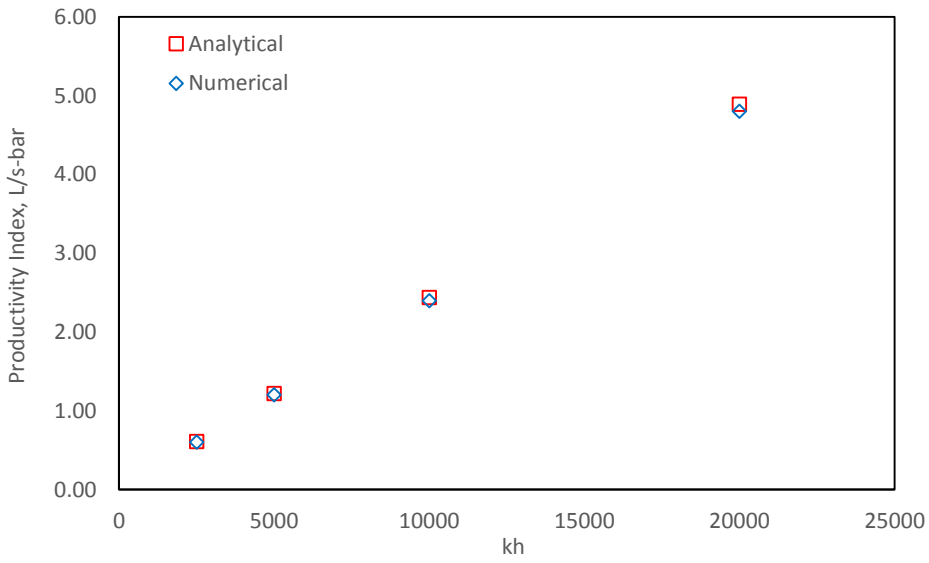

Figure 3-5 Comparison of average reservoir productivity index obtained from the numerical model and analytical solution.

Table 3-4 Pressure difference between the injector and producer, and average productivity index, obtained from the analytical and numerical model

Time-step		1000	30	1000	30	1000	30
Grid-size		100 × 100		50 × 50		10 × 10	
Permeability, mD		200		200		200	
kh, m		10000		10000		10000	
Numerical	Avg. Res Pressure	28500.8	28502.1	28502.1	28502.1	28502.1	32385.3
	Injector BHP (kPa)	32392.0	32393.8	32387.9	32387.9	32393.8	28502.0
	Producer BHP (kPa)	24623.2	24607.6	24619.5	24619.5	24607.6	24616.6
	PI (L/s-bar)	2.40	2.399	2.403	2.403	2.399	2.405
Analytical	PI (L/s-bar)	2.44	2.440	2.440	2.440	2.440	2.440
Relative error (%)		1.649	1.661	1.512	1.512	1.661	1.449

3.3.2 Effect of numerical grid size on thermal breakthrough time

All types of numerical simulation methods based on spatial and temporal discretization inevitably involves numerical error and additional numerical dispersion which makes the results deviate from the mathematical solutions. There can be many reasons for this but in this study we are interested in the size of the grid-blocks and time step. We can improve numerical accuracy by increasing the number of grid-block and tightening the time-step. However, it takes more time to reach a solution. Therefore, there is the need to achieve a compromise between accuracy and computational costs for practical application. For the purpose of the preliminary study, an analytical solution is used to evaluate the appropriateness of the numerical solution. The degree of numerical dispersion is tested with different grid-block size.

As previously discussed, the effect of grid size and time-step on the reservoir hydraulics, due to the steady-state assumption, is not significant. Unlike this, the effect of grid-block size plays a significant role on the thermal behavior since cold water is injected into a hot reservoir to displace hot fluids towards the production well, the system is constantly under unsteady-state conditions in terms of energy balance. The injected cold water absorbs heat from the surrounding rocks and the surrounding rocks loose heat by the flowing cold water. Consequently, there exists discontinuity at the thermal front where the temperature across has a sharp change. This abrupt change in temperature exacerbates numerical dispersion.

The thermal evolution of the reservoir, obtained from the numerical model, is affected by the spatial discretization or grid block size because of the magnitude of numerical dispersion. Figure 3-6 shows the bottomhole temperature (BHT) change over time at the location of the production well obtained with different grid block sizes. The typical behavior of temperature as a function of time observed in each solution presents a constant temperature equal to the initial reservoir temperature, followed by a decline in temperature because of arrival of colder water to the production well. The time when the temperature begins to decrease is known as the thermal breakthrough time. After this time the temperature at the location of the production well starts decreasing, approaching the end of geothermal reservoir lifetime.

The numerical solution obtained changes with the grid-block size of the simulation model. The case with the coarser grid (100 x 100 m) presents an earlier thermal breakthrough time and a lower temperature decline rate. While the case with the finer grid (2.5 x 2.5 m) presents a longer thermal breakthrough time with a more sharper thermal front arriving to the production well. A higher temperature decline rate corresponds to a sharper thermal front, which indicates lower numerical dispersion. By decreasing gird block-size, the thermal breakthrough time increases, and the relative error between the numerical and analytical solution decreases. The maximum time-step size used in the numerical simulation is 30 days. The reservoir dimension, grid-block size and the total number of grid blocks are listed in Table 3-5.

Table 3-6 summarizes the numerical results obtained with different grid block sizes and presents a comparison with the analytical solution. At this point, the relative error is significantly high (> 20%) to be considered acceptable.

3.3.3 Effect of reservoir no-flow boundary on thermal breakthrough time

We further improve the numerical solution by considering the effect of the distance of no-flow reservoir boundaries from the wells. Figure 3-7 shows a comparison between the base reservoir model, with reservoir dimensions used in the previous section, and an enlarged reservoir model, where the no-flow boundaries are further apart from the wells. Table 3-7 summarizes the numerical results obtained with different reservoir model dimensions for a grid-block size of 50 x 50 m, and presents a comparison with the analytical solution. The thermal breakthrough time is extended by increasing the reservoir dimension, and the relative error between the numerical and analytical solution is alleviated. By increasing the reservoir model size,

the effect of no-flow boundaries on the numerical solution has decreased, and the numerical solution more approximates the analytical solution. There is a reservoir model dimension where further increase in the reservoir dimension does not improve the solution significantly.

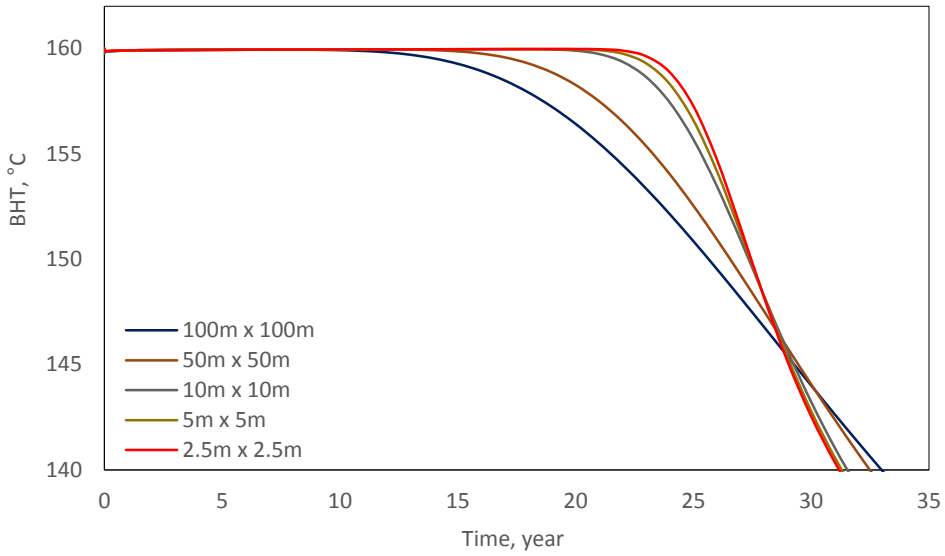

Figure 3-6 Plot of BHT at the production well location as function of time, showing effect of model grid-block size (in meters) on calculated thermal breakthrough time.

Table 3-5 Computational time and number of grid-blocks for various grid-block size

Grid block size (m)	Reservoir dimension (m)	Number of grid blocks
100 x 100	4500 x 3000	1,350
50 x 50	4500 x 3000	5,400
10 x 10	4500 x 3000	135,000
5 x 5	4500 x 3000	540,000
2.5 x 2.5	4500 x 3000	3,240,000

Table 3-6 Comparison of thermal breakthrough time of analytical solutions and numerical results for various grid-block size

Grid block size (m)	Reservoir size (m)	Well spacing (m)	Thermal breakthrough time (year)		Relative error (%)
			Analytical	Numerical	
100 x 100	4500 x 3000	1500	30	16	46.7
50 x 50	4500 x 3000	1500	30	19	36.6
10 x 10	4500 x 3000	1500	30	22	26.6
5 x 5	4500 x 3000	1500	30	23	23.3
2.5 x 2.5	4500 x 3000	1500	30	24	20

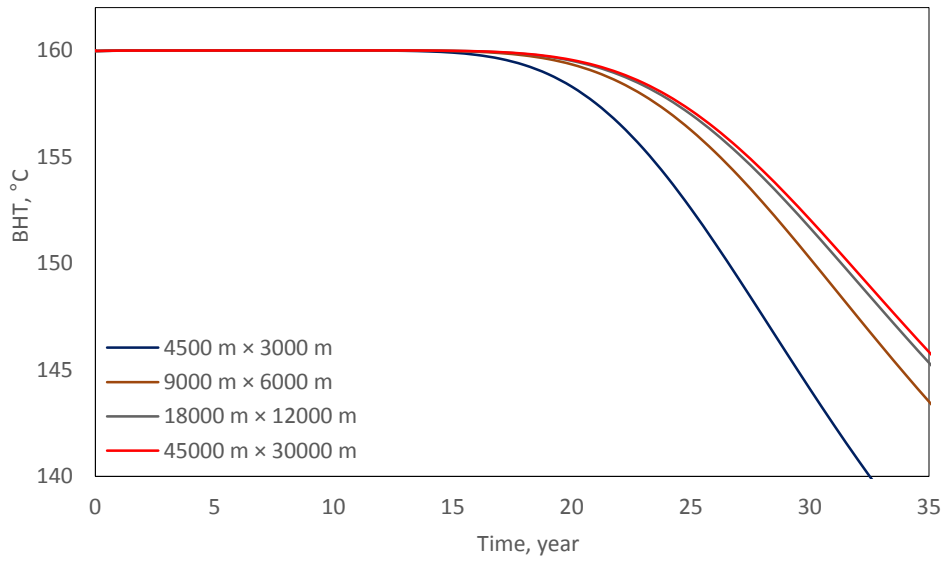

Figure 3-7 BHT at production well over reservoir lifetime for 4 different reservoir areal dimensions – 4,500 m × 3,000 m, 9,000 m × 6,000 m, 18,000 m × 12,000 m and 45,000 m × 30,000 m.

Table 3-7 Summary of numerical results of thermal breakthrough time obtained with different model dimensions for a grid-block size of 50 x 50 m, and comparison with analytical solution

Reservoir size (m)	Thermal breakthrough time (years)		Relative error (%)
	Analytical solution	Numerical solution	
4,500 × 3,000	30	19	36.7
9,000 × 6,000	30	21	30.0
18,000 × 12,000	30	22	26.7
45,000 × 30,000	30	22	26.7

Figure 3-8 shows the streamline between the injection and production well. The smallest reservoir size model (Figure 3-8 (a)) shows that the streamline is compressed in the north-south direction due to the reservoir boundary. As the reservoir size grows (Figure 3-8 (b), (c) and (d)), the streamline becomes close to a perfect circle as the flow path is not interrupted by no-flow boundary. Infinite acting reservoir without no-flow boundary is an important assumption implied in the derivation of the analytical solution (Eq. 3.1). This is because the analytical solution is derived by solving heat conduction equation for a potential flow – non-viscous, incompressible and irrotational velocity field, governed by the Laplace equation. Therefore, the numerical solution approaches the analytical solution in a reservoir with a larger dimension since it mitigates the flow boundary effect.

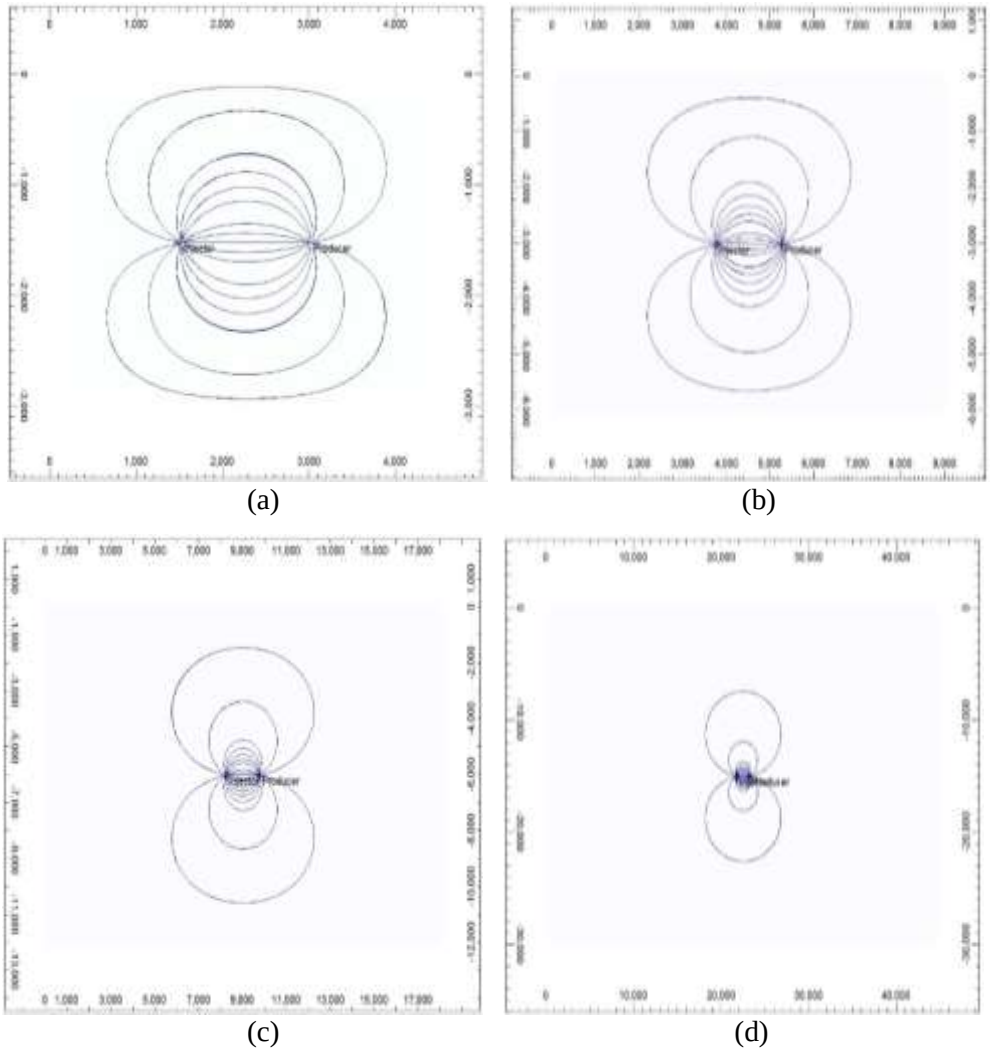

Figure 3-8 Streamline between production and injection well for the reservoir size of 4,500 m × 3,000 m (a), 9,000 m × 6,000 m (b), 18,000 m × 12,000 m (c) and 45,000 m × 30,000 m (d).

3.3.4 Time-step effect on thermal breakthrough time

In general, grid size and time-step effects are coupled. Thus, we perform an evaluation of the time step used during the numerical solution of the flow and thermal behavior of the geothermal reservoir, which also plays a role in the accuracy of the solution by affecting the numerical dispersion. Figure 3-9 shows the temperature change at the production well with time obtained using different time step values for a grid-block size of 10 x 10 m. The time step effect on thermal breakthrough time is more evident as the grid block size decreases (Figure 3-9 (a), (b) and (c)). For time steps less than 1 month, the change in the solution is not considerable, which indicates that a time step of 1 month is an appropriate value for the maximum time step to for the given reservoir parameters.

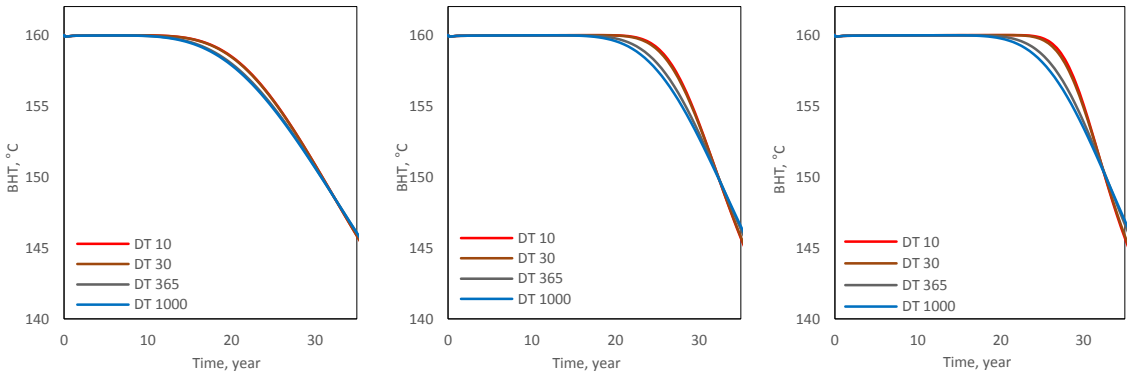

(a) (b) (c)

Figure 3-9 BHT at production well for different grid sizes - 100 × 100 m (a) , 20 × 20 m (b) and 10 × 10 m (c) - with respect to different maximum time-step intervals (10 days, 30 days, 365 days and 1,000 days).

3.4 Optimum grid configuration

The next step was the study of different numerical grid configurations, in order to obtain an optimal grid system with a minimum number of grid blocks and practical computational time. The numerical grid configuration is defined by specifying the grid block size of the interest area in the center of the reservoir model containing the pair of wells, the total reservoir areal dimensions, and the grid block size distribution in the reservoir boundary surrounding the interest area. Table 3-8 presents the parameters of different numerical grid configurations considered in this study, and Figure 3-10 shows a plane view of the grid configurations.

Table 3-8 Parameters of numerical grid configurations studied

Grid ID	Grid block size of interest area (m)	Reservoir size (m)	Grid block size distribution of reservoir boundary	Number of grid blocks	Computational time
(a)	20 x 20	4,500 x 3,000	N/A	33,751	6m 44s
(b)	20 x 20	34,500 x 33,000	Coarser	33,759	6m 45s
(c)	20 x 20	34,500 x 33,000	Linear, 20 x 20, for coordinates of interest area	34,504	6m 57s
(d)	20 x 20	34,500 x 33,000	Logarithmic coarser	34,191	7m 3s
(e)	20 x 20	66376 x 64876	Logarithmic finer	42,650	8m 16s
(f)	20 x 20	34,500 x 33,000	Logarithmic medium	34,591	7m 00s
(g)	20 x 20	34,500 x 33,000	20 x 20 entire reservoir model	2,881,725	11h 22m 02s

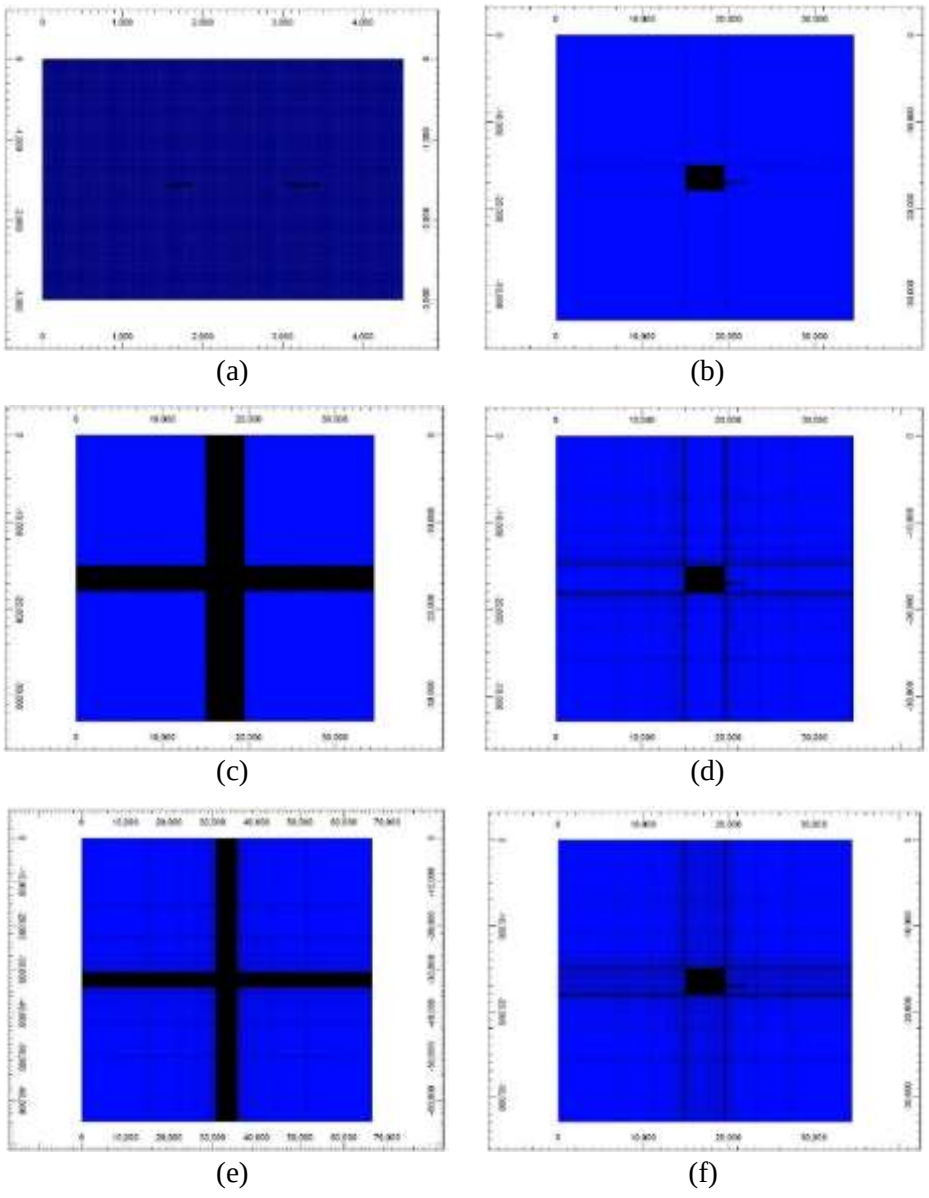

Figure 3-10 Grid configurations considered in this study.

The optimal numerical grid configuration is selected from the numerical solution close to the analytical solution. Figure 3-11 shows the temperature at the production well as function of time obtained using the different grid configurations. Grid (e) and Grid (f) shows the best solution and it is associated with a practical computational time (from Table 3-8). Figure 3-12 shows that Grid (e) and Grid (f) shows the same result as Grid (g) of which entire area is discretized with 20 x 20 m grid blocks.

Applying the optimal numerical grid configuration, grid (f), to several cases with different grid block sizes in the interest area, we verify that the calculated thermal behavior of the geothermal reservoir is more accurate when using a finer grid.

Table 3-9 shows the temperature change at the production well with time for different grid block sizes using grid (f). Like Figure 3-6, the solution with the optimal grid configuration also shows longer thermal breakthrough times with smaller grid block sizes, and a sharper thermal front arriving to the production well, which indicates a decrease in the numerical dispersion. Table 3-9 presents a summary of the results obtained with different grid block sizes and the optimal grid configuration. With the two smallest grid block sizes (5 x 5 m, and 2.5 x 2.5 m) the relative error with respect to the analytical solution is reduced to 6.6%.

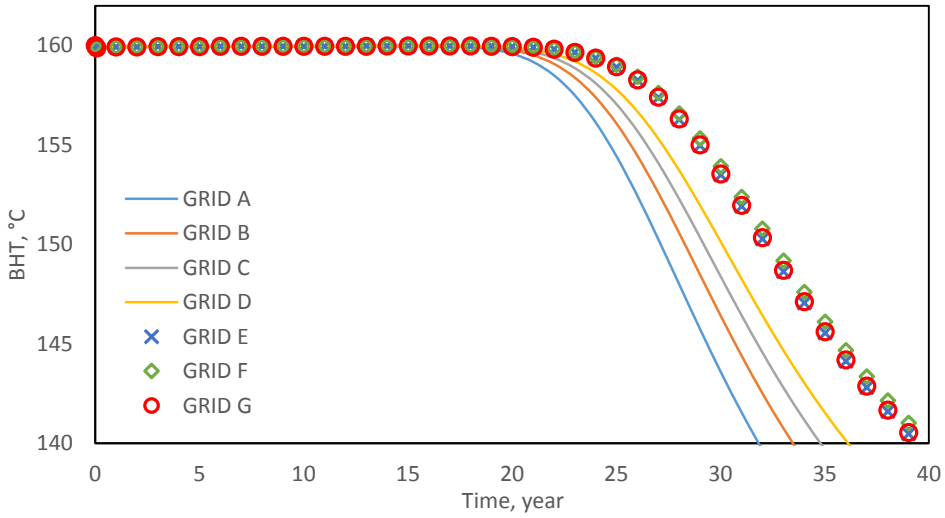

Figure 3-11 Plot of BHT at the production well location as function of time, for different numerical grid configurations.

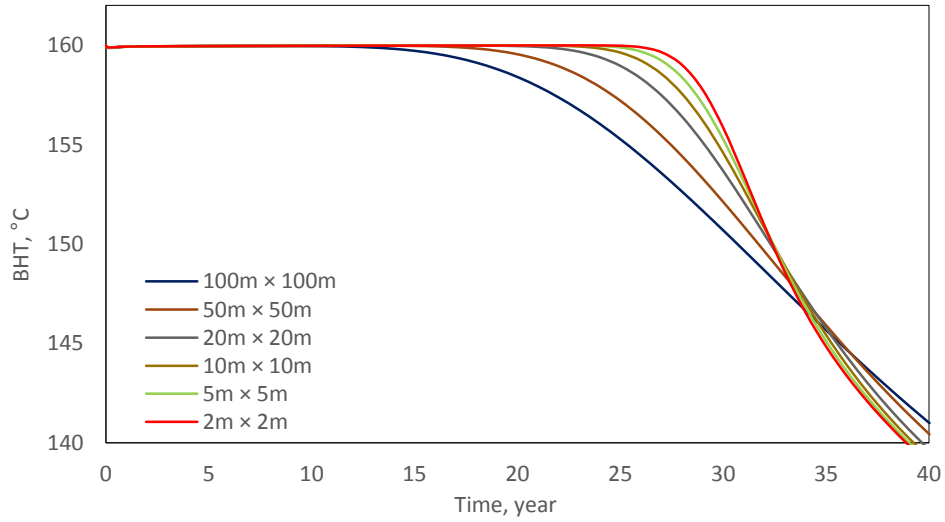

Figure 3-12 Plot of BHT at the production well location as function of time, for different grid block sizes using grid configuration (f).

Table 3-9 Summary of numerical results of thermal breakthrough time obtained with different grid block sizes using grid (f), and comparison with analytical solution

Grid block size (m)	Reservoir size (m)	Well spacing (m)	Thermal breakthrough time (year)		Relative error (%)
			Analytical solution	Numerical solution	
100 x 100	34500 x 33000	1500	30	19.0	36.6%
50 x 50	34500 x 33000	1500	30	22.0	26.6%
20 x 20	34500 x 33000	1500	30	25.0	16.6%
10 x 10	34500 x 33000	1500	30	27.0	10.0%
5 x 5	34500 x 33000	1500	30	28.0	6.6%
2 x 2	34500 x 33000	1500	30	28.0	6.6%

This result presents the validation of the numerical reservoir model with an analytical model. The grid configuration proposed shows an acceptable match between the numerical and analytical solutions. In order to improve the accuracy of the numerical solution with reference to the analytical solution, the numerical grid block size and the effect of the reservoir no-flow boundaries should be considered. We found that the numerical solution improves by reducing the grid block size and by increasing the reservoir areal size (i.e., placing no-flow boundaries further apart from the wells). With the two smallest grid block sizes (5 x 5 m and 2 x 2 m) the relative error with respect to the analytical solution is reduced to 6.6%.

As the effect of the time step is not as significant as the effect of the numerical grid size, a maximum time step of 1 month is appropriate for the simulation of geothermal reservoirs, considering that the magnitude of the reservoir lifetime is around 30 years. In sum, the agreement obtained between the numerical and analytical models allows us to proceed with confidence to study reservoir enhancement techniques using numerical reservoir simulation.

CHAPTER 4
TRACER TEST MODELING

G. M. Shook (2000) proposed a tracer test method to predict thermal breakthrough time for a single-phase flow in heterogeneous porous media. His formulation correlates the velocity of a thermal front to the interstitial velocity of tracer. A retardation factor which shows how the temperature front movement is retarded due to the heat transfer from the surrounding rocks is introduced and it allows calculating the thermal breakthrough time based on the tracer breakthrough time.

4.1 Analytical formulation of a tracer test

The conservation of mass and energy for single-phase fluid in porous media is follows,

$$\phi \frac{\partial \rho_w}{\partial t} + \vec{\nabla} \cdot (\rho_w \vec{u}_w) = 0 \tag{4.1}$$

$$\phi \frac{\partial (\overline{\rho C}_p T)}{\partial t} + \vec{\nabla} \cdot (\rho_w \vec{u}_w C_{pw} T) = \vec{\nabla} \cdot (\overline{\kappa} \vec{\nabla} T) \tag{4.2}$$
$$\text{where, } \rho C_p = \phi \rho_w C_{pw} + (1-\phi)\overline{\rho C_{pr}}$$

In Eq. 4.1 and Eq. 4.2, it is assumed that there is thermodynamic equilibrium between the rock and fluid domain. By neglecting rock compressibility and assuming constant thermal properties of rock and water, Eq. 4.1 and Eq. 4.2 are combined to get Eq. 4.3.

$$\frac{\partial T}{\partial t} + \frac{u_w}{\phi}\left(\frac{\phi \rho_w C_{pw}}{\phi \rho_w C_{pw} + (1-\phi)\rho_r C_{pr}}\right)\vec{\nabla} T - \kappa \vec{\nabla}^2 T_D = 0 \tag{4.3}$$
$$\text{where, } \kappa = \frac{\overline{K}}{p_r C_p}$$

If it is assumed that heat conduction is negligible compared to convection term (to be discussed in Section 4.4) and Eq. 4.3 could be arranged to get Eq. 4.4.

$$\frac{v_T}{v_w} = \frac{v_T}{u_w / \phi} = \frac{\phi \rho_w C_{pw}}{\phi \rho_w C_{pw} + (1-\phi)\rho_r C_{pr}} = \frac{1}{1 + D_T} \tag{4.4}$$
$$\text{where, } D_T = \frac{(1-\phi)\rho_r C_{pr}}{\phi \rho_w C_{pw}}$$

D_T is thermal retardation factor. It is the measure of how the velocity of thermal front movement is delayed with respect to fluid velocity by heat transfer. Higher values of retardation factor mean that the

degree of reduction in thermal front velocity is higher. The lifetime of doublet systems or the arrival time of a thermal front can be estimated using the following correlation,

$$t_T^{BT} = t_w^{BT}\left(1 + D_T\right) \tag{4.5}$$

Eq. 4.5 indicates that the ratio of thermal front breakthrough time and fluid-flow breakthrough time is a constant, which is determined by the retardation factor. The retardation factor is solely a function of volumetric heat capacity of the rock and fluid. Therefore, thermal front breakthrough time can be obtained from tracer (water) breakthrough time using Eq. 4.5.

Eq. 4.5 has the following two assumptions:

- The viscosity and density of reservoir fluid are constant,
- The heat conduction is negligible.

Despite limitations from the above assumptions, Eq. 4.5 does involve no assumption of homogeneity and isotropy of reservoir rock properties. Therefore, it can be used to approximate the thermal front breakthrough time for a reservoir which heterogeneity and anisotropy in porosity and permeability. Hence, Shook's tracer testing can be used as a powerful tool to evaluate the possibility of short-circuiting in heterogeneous and anisotropic reservoirs.

4.2 Numerical tracer test model in homogeneous reservoir

The tracer is modeled as an aqueous phase component so it travels along with the water phase. Hence, the properties of tracer modeled are considered the same as water. The tracer component is carried into the reservoir with the water injection stream. The duration of tracer injection is set to 1 day. The mole fraction of the tracer component is captured at the producer well. Figure 4-1 shows the behavior of temperature and mole fraction of the tracer component at the producer well. The tracer component reaches the producer well after 4 years of production. This is the time when the injected water and tracer reach the producer well – injected water breakthrough time or tracer breakthrough time. The temperature at the producer remains constant until the thermal front arrives at the producer well. The injected cold water moves in the porous media while absorbing heat from the surrounding rocks, and thus, the advancement of the thermal front is retarded by a factor of 1 plus the retardation factor ($1+D_T$). It is noteworthy that this correlation holds good regardless of the presence of no flow boundary and the effects of grid-size and time-step. This is because energy balance and flow calculation are affected by the same magnitude at the same time.

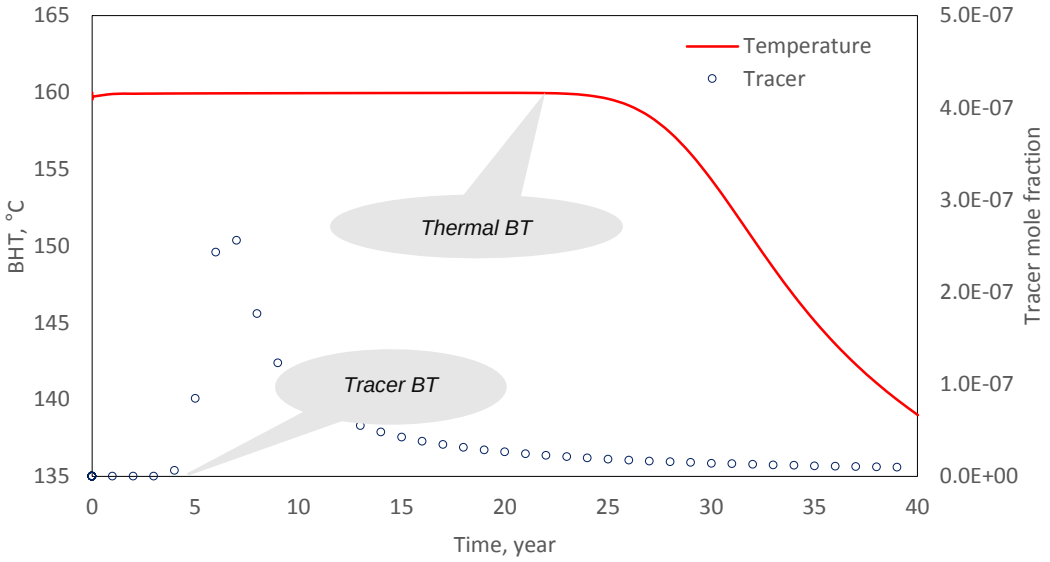

Figure 4-1 Shook's tracer test model in a homogeneous reservoir - tracer breakthrough time and temperature breakthrough time are marked.

The reservoir dimension of 100m × 100m × 50m with the grid block size of 1m × 1m × 50 m with no flow boundary at each side is used to test the Shook's correlation. The well spacing – distance between the producer and injector well, is 140 m. Figure 4-2 shows that the tracer propagation (b) which corresponds to the interstitial velocity of water already reached the producer while the thermal front (a) does not pass even the half of the well spacing distance.

Table 4-1 shows the correlation between the thermal breakthrough time and the tracer breakthrough time for different flow rates. The ratio of the thermal breakthrough time and the water breakthrough time is 1 + Retardation factor$(1 + D_T)$. Hence, the retardation factor governs the relationship between water flow and heat evolution. The retardation factor is a function of the reservoir rock and fluid thermal properties such as heat capacity. For constant density and viscosity, the heat capacity of water and rock establishes how much the heat front is retarded with respect to the water flow. As water heat capacity is a given value with little variation, the heat capacity of reservoir rocks is key element for determining the thermal breakthrough time. Table 4-1 shows the comparison of the thermal breakthrough time between the Gringarten and Sauty's solution. The thermal breakthrough time obtained from the Gringarten and Sauty is longer than that from the Shook's correlation. The correlation between the thermal breakthrough and tracer breakthrough time holds good while the thermal breakthrough time obtained from the numerical simulation is shorter than that of the Gringarten and Sauty's solution. As discussed in Section 3.3, the thermal breakthrough time obtained with the numerical model is affected by the grid-block size, time-step and no flow boundary which all add up to shorten the time when the temperate at the producer drops.

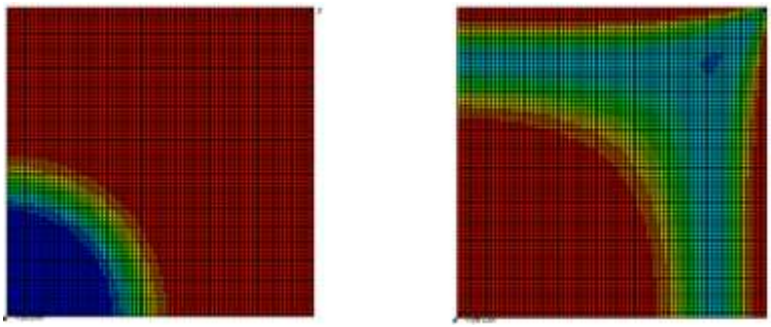

(a) (b)

Figure 4-2 Thermal front (a) and tracer propagation (b) after 5 years of production in homogeneous reservoir model.

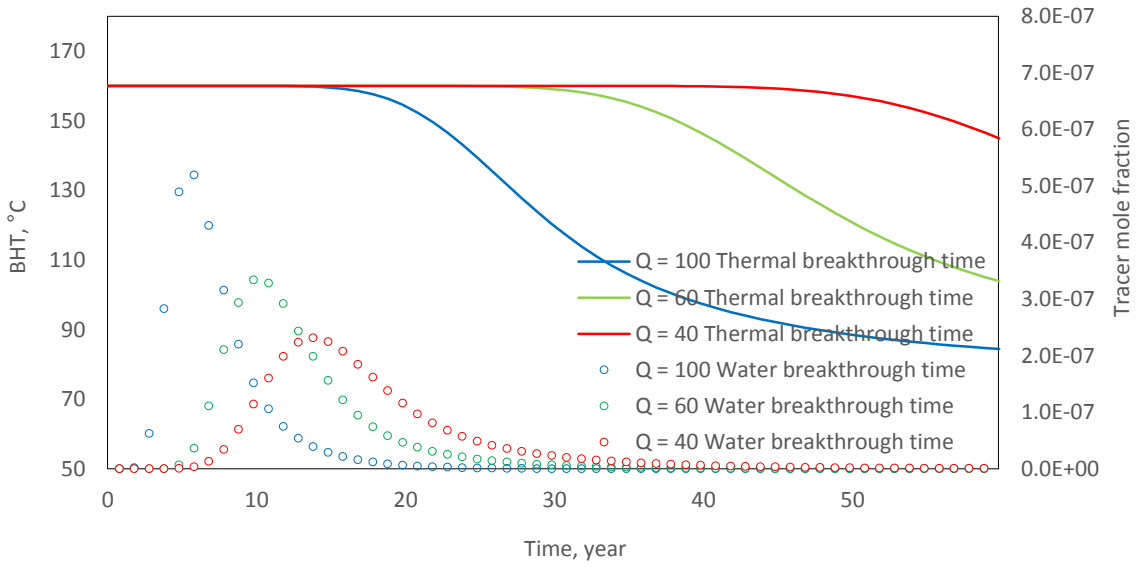

Figure 4-3 Thermal Front and tracer propagation in homogeneous reservoir model for different flow rate – 40 m^3/day, 60 m^3/day and 100 m^3 /day.

Table 4-1 Tracer test results in homogeneous reservoir model for varying flow rates compared to the Gringarten and Sauty solution

Q (m^3/day)	Retardation Factor	Breakthrough time obtained from the Gringarten and Sauty's solution (year)	Breakthrough time obtained from the numerical model (year)	Tracer breakthrough time (year)	Breakthrough time using Eq. 4.5 (year)
100	4	17	14	3	15
60	4	28	27	5	25
40	4	42	40	8	40

4.3 Application of tracer test model to reservoirs with heterogeneity and anisotropy

The relation between the tracer breakthrough time and thermal front breakthrough time is given by Eq. 4.5. Eq. 4.5 is valid for reservoirs with spatial variation. In a geothermal field, a tracer test can be used to capture hydraulic connectivity. Using a field scale tracer test, we can identify the presence of high permeability channel which could cause a premature thermal breakthrough or short-circuiting. The Shook's correlation was tested with various models: homogeneous, heterogeneous (porosity and permeability), high permeability channel model and a model with a tensile fracture at each well. Various hypothetical reservoir models with spatial variation in porosity and permeability are tested. Parameters of each model are descried in Table 4-2 and the simulation results are presented from Figure 4-4 to Figure 4-9.

Table 4-2 Reservoir models for Shook's correlation

Model	Porosity	Permeability(mD)	Retardation factor	Remarks
Reference	0.15	125	4	Reference model
Model A	0.3 ~ 0.4	125	-	High avg. porosity
Model B	0.05 ~ 0.15	125	-	Low avg. porosity
Model C	0.15	150 ~ 240	4	High avg. permeability
Model D	0.15	10 ~ 100	4	Low avg. permeability
Model E	0.15	125 / 125 ~ 300	4	High perm channel model
Model F	0.15	125	4	Tensile fractured model

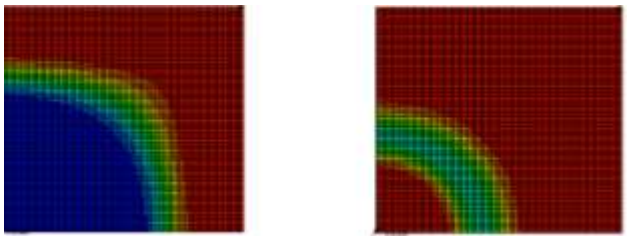

(a) (b)

Figure 4-4 Model A (high average porosity model) - thermal front propagation after 30 years (a) and tracer propagation after 5 years (b).

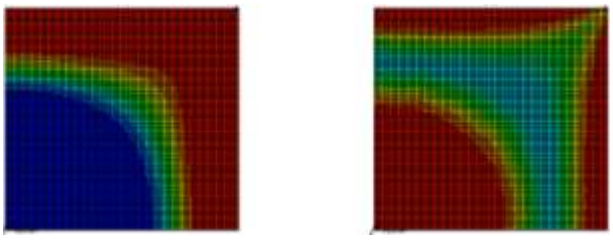

(a) (b)

Figure 4-5 Model B (low average porosity model) - thermal front propagation after 30 years (a) and tracer propagation after 5 years (b).

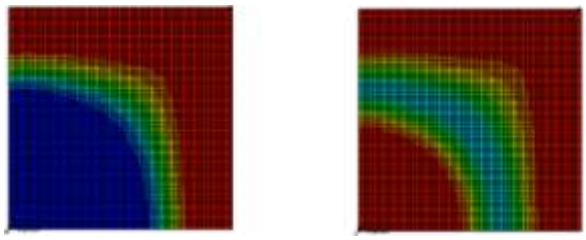

(a) (b)

Figure 4-6 Model C (high average permeability model) - thermal front propagation after 30 years (a) and tracer propagation after 5 years (b).

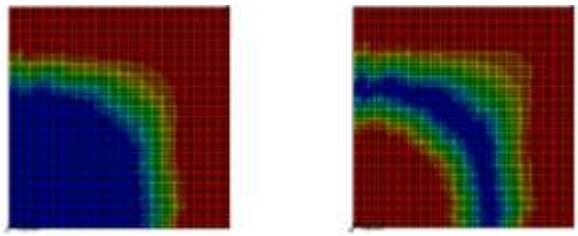

(a) (b)

Figure 4-7 Model D (low average permeability model) - thermal front propagation after 30 years (a) and tracer propagation after 5 years (b).

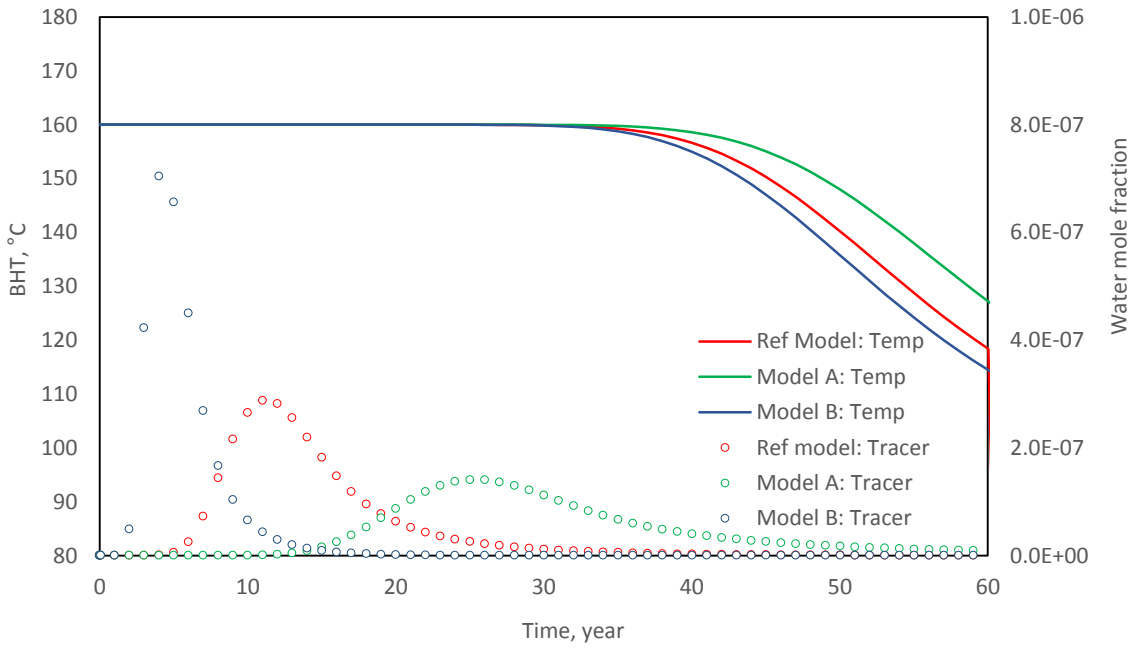

Figure 4-8 Thermal front propagation and tracer propagation in the heterogeneous (porosity) reservoir model compared to the homogeneous model – Model A and Model B.

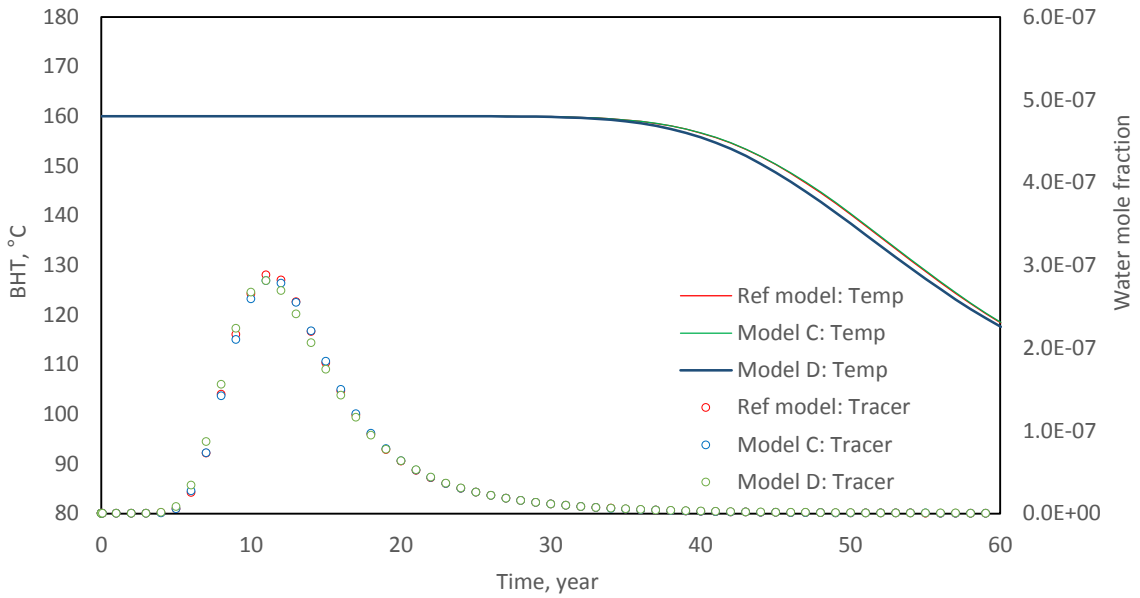

Figure 4-9 Thermal front propagation and tracer propagation in the heterogeneous (permeability) reservoir model compared to the homogeneous model – Model C and Model D.

Permeability variation, particularly in low permeability reservoir, causes unstable thermal front movement. High permeability channels in a reservoir are highly likely to cause premature thermal front breakthrough. To see the effect of permeability distribution forming a high permeability channel, a simulation model with a strip of higher permeability along the wells (Figure 4-10) is tested and its thermal front propagation is compared to that of the homogeneous model in Figure 4-11. The thermal front along the high permeability channel travels much faster than in the rest of the reservoir. This phenomenon is called "short circuiting", making the thermal breakthrough time (17 year) to be significantly shorter than that (27 year) of the homogeneous model.

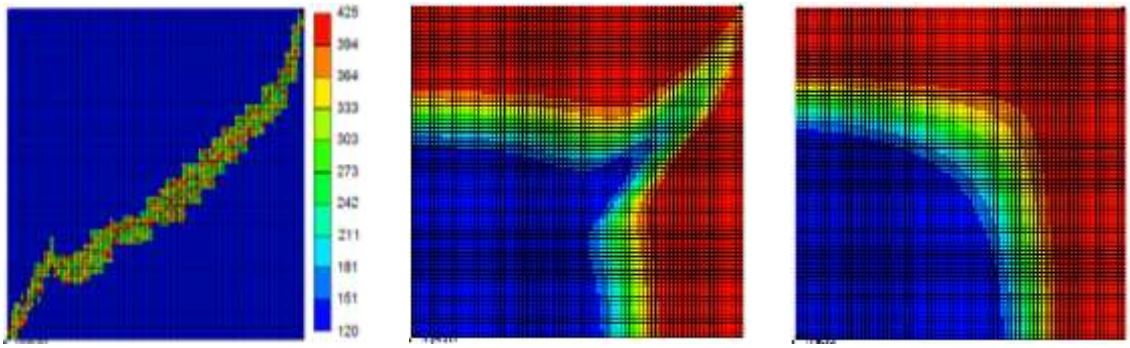

(a) (b) (c)

Figure 4-10 High permeability channel model – Model (a): permeability in the high perm zone ranges from 125 to 300 and the rest of the reservoir permeability is 125 mD, thermal front propagation after 30 years in high permeability channel model (b) and that of homogeneous model after 30 years (c) for comparison.

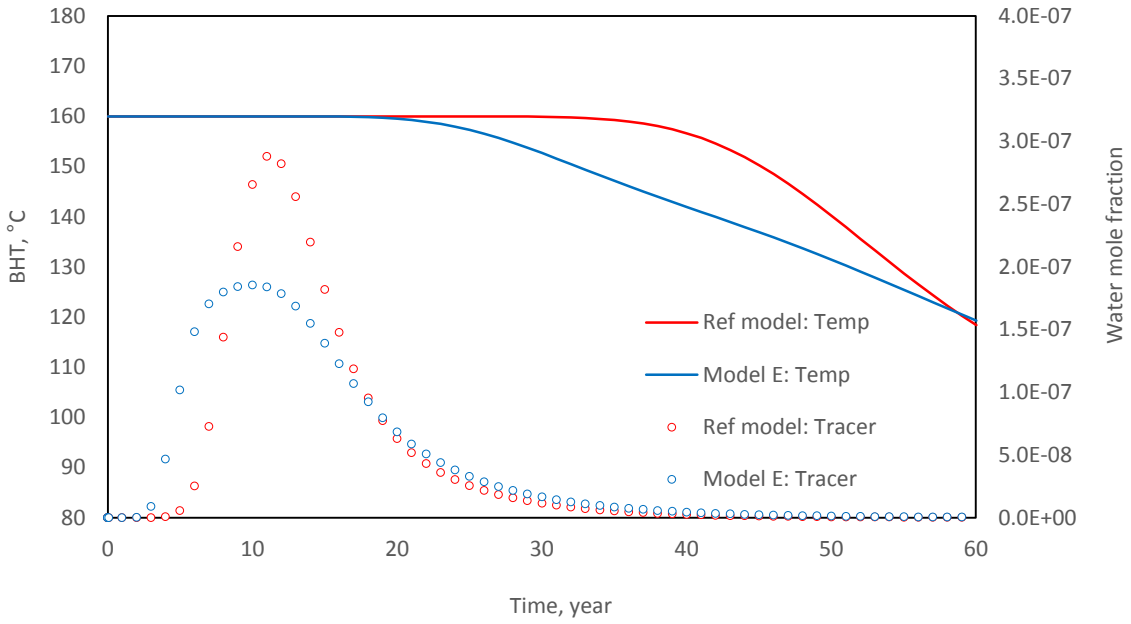

Figure 4-11 Thermal front propagation and tracer propagation in the reservoir model with high permeability channel - compared to the homogeneous model.

It is of no doubt that hydraulic fracturing can help overcome low permeability of the sedimentary formation for geothermal energy extraction by enhancing the injectivity and productivity of the wells. Therefore, multi-stage hydraulic fracturing with horizontal well may be able to make feasible a large capacity power generation from deep sedimentary basin. However, it could possibly lead to premature thermal front breakthrough. Hence, simulation study in this project focuses on the thermal evolution in hydraulically fractured reservoirs. As shown in Figure 4-12 , the reference simulation model is used and the vertical hydraulic fractures (red circled) at producer and injector are added using local grid refinement (LGR) to see its effect on thermal front propagation.

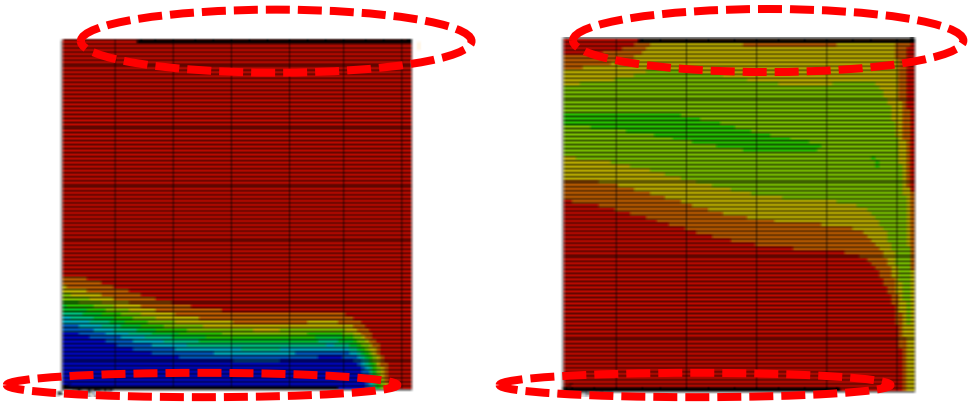

Figure 4-12 Thermal front (a) and tracer propagation (b) in the reservoir model with tensile hydraulic fracture modeled at the producer and injector.

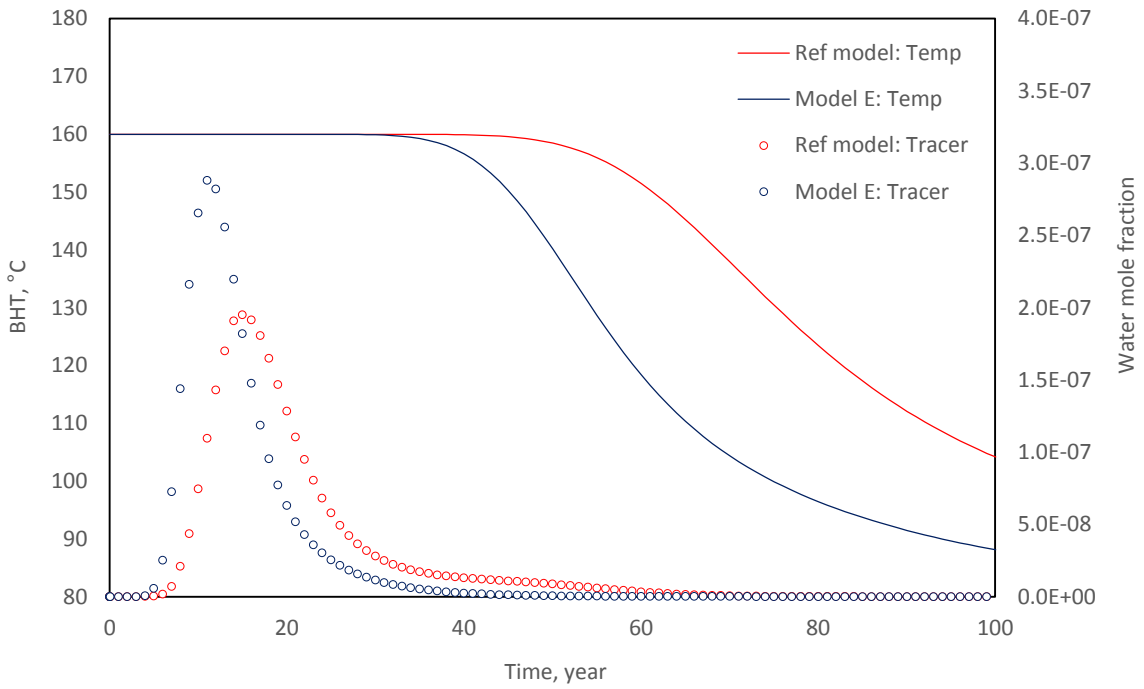

Figure 4-13 Comparison between the hydraulically fractured reservoir model and the homogeneous reservoir model with no hydraulic fracturing.

4.4 Thermal Peclet Number

Eq. 4.1 can be rearranged in dimensionless form in Eq. 4.6,

$$\frac{\partial T_D}{\partial t_D} + \frac{v_D}{1+D_T}\nabla_D T_D - \frac{1}{N_{PeT}}\nabla^2 T_D = 0$$

$$\text{where, } N_{PeT} = \frac{v_w L}{\kappa},\ T_D = \frac{T(t)-T_I}{T_J - T_I} \tag{4.6}$$

Eq. 4.8 has the dimensionless thermal Peclet number, which is the ratio of thermal convection to thermal conduction. Higher Peclet number means that heat transfer is dominated by heat convection rather than heat conduction. In the formulation of Eq. 4.6., it is assumed that heat conduction is negligible. To ignore heat conduction, Peclet number in Eq. 4.6 should be much greater than unity ($N_{PeT} >> 1$), and then the thermal conduction term can be neglected. By assuming a radial flow (Q = 8068 m^3/day), Peclet number for the base reference model with constant thermal conductivity of rock and water can be obtained as follows,

$$K_{mix} = \phi K_{water} + (1-\phi)K_{rock}, \quad \kappa = \frac{\rho C_p}{K_{mix}} \tag{4.7}$$

$$v_w = q / A\phi$$

$$N_{PeT} = \frac{v_w L}{\kappa} = \frac{Q}{A\phi}\frac{L}{\kappa} = \frac{Q}{2\pi h\phi\kappa} \tag{4.8}$$

Therefore, Peclet number is greater than unity and the condition can be expressed in a more general way as follows (Shook, 2001),

$$q / h \gg 2\pi\phi\kappa \tag{4.9}$$

The effect of thermal conduction in reservoirs can be significant when the flow rate is extremely low or the thermal conductivity of rock and fluid is very high. Figure 4-14 shows that the Shook's correlation is not valid any longer when the Peclet number does not satisfy Eq. 4.9 shows five cases with different Peclet number. Case 2 has the values of thermal conductivity of typical reservoir rock and water. The results of Case 2 is identical with Case 1 (no thermal conduction). On the contrary, Case 4 has extremely high values of thermal conductivity of rock and water, and it has its thermal breakthrough time at 5 years, one fourth shorter than Case 2. The Shook's correlation is not valid any longer for Case 1 and 2 since heat conduction plays a role in thermal regime of the system. Table 4-3 summarizes the thermal properties and parameters of the Shook's correlation with the calculation of Peclet number for each case.

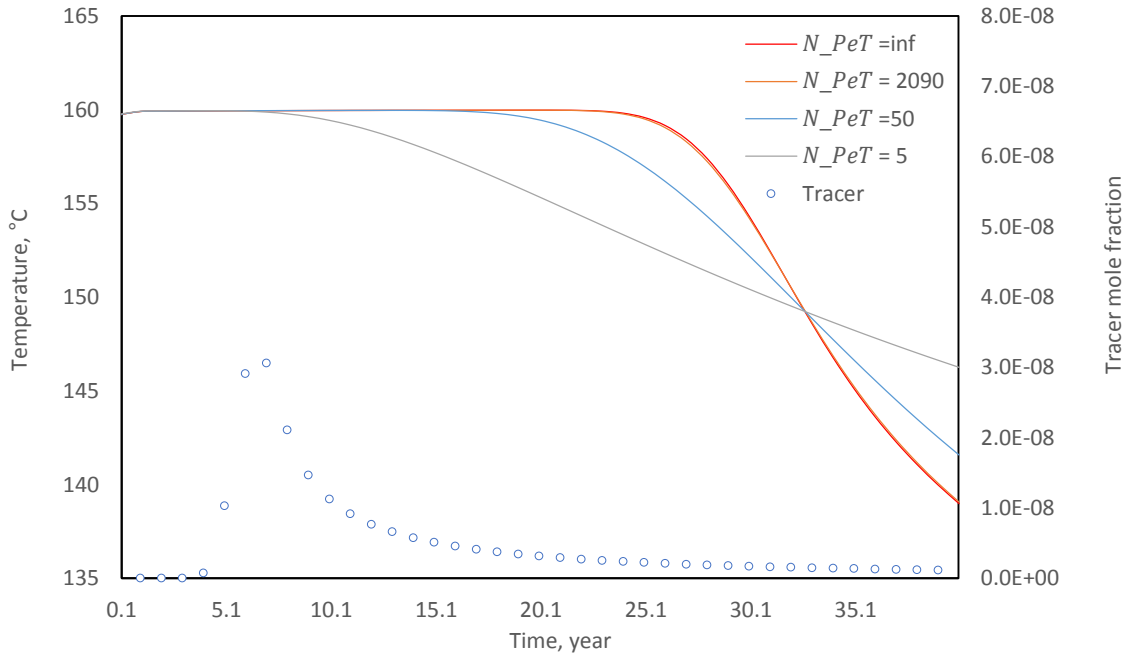

Figure 4-14 Effect of thermal conductivity of rock and water (Peclet number) on thermal breakthrough time.

Table 4-3 Calculation of thermal Peclet number for various cases with thermal conductivity of rock and water, and its effect on thermal breakthrough time and retardation factor

Case	1	2	3	4
K_{water} (J/m-day-^oC)	0	5.35E+04	1.00E+07	1.00E+08
K_{rock} (J/m-day-^oC)	0	2.74E+05	1.00E+07	1.00E+08
κ (m^2/day)	0	8.19E-02	3.40E+00	3.40E+01
Theoretical D_T	4	4	4	4
t_w^{BT} (year)	4	4	4	4
t_T^{BT} (year)	20	20	14	5
True D_T	4	4	2.5	0.25
N_{PeT}	Infinite	2090	50	5

CHAPTER 5
EFFECT OF ROCK and FLUID PROPERTY

The propagation of thermal front is affected by rock and water properties of the reservoir. Particularly, thermal properties of rock and water have a significant impact on the reservoir performance. Hence, the importance of thermal properties of reservoir element becomes more evident in geothermal reservoir engineering. Using representative values of rock and water at reservoir condition (Table 5-1), the effect of rock and water properties on thermal behavior is evaluated by comparing each to the reference model whose rock and fluid properties are held constant.

5.1 Effect of water properties – compressibility, density and viscosity

The effect of water compressibility on fluid temperature at production well is shown in Figure 5-1. The compressibility of water does not have a considerable impact on the thermal breakthrough time since it is not a strong function of temperature. Hence, the assumption of incompressibility that the Gringarten and Sauty bases on is acceptable. On the contrary, the density and viscosity of water has a significant impact on the temperature behavior at the production well. Figure 5-2 and Figure 5-3show that change in viscosity and density of water (viscosity and density increases with decrease in temperature) have a considerable impact on the thermal breakthrough time. Viscosity as a function of temperature delays the thermal breakthrough time while density as a function of temperature shortens the thermal breakthrough time. Both the Gringarten and Sauty's solution and the Shook's correlation assume that the density and viscosity of water is constant. As such, neither are valid once density and viscosity changes with temperature. Nevertheless, the analytical solution, as shown in Figure 5-4, gives us a conservative estimate of thermal breakthrough time. Therefore, the analytical solutions can be used as a starting design criterion for predicting well spacing and reservoir lifetime of geothermal doublets.

Table 5-1 Representative properties of rock and fluid at reservoir condition

Properties	Water	Rock
Compressibility (1/kPa)	4.5E-7	4.4E-7
Density (g/cc)	Internal table	Quartz: 2.65 Calcite 2.7 Kaolinite: 2.63
Viscosity (cp)	Internal table	-
Heat capacity (J/m^3-^oC)	-	Quartz: 2.38E6 Calcite 2.48E6 Kaolinite: 2.871E6
Thermal conductivity (J/m-day-^oC)	-	Sandstone: 2.74E5 Andesite: 1.54E5

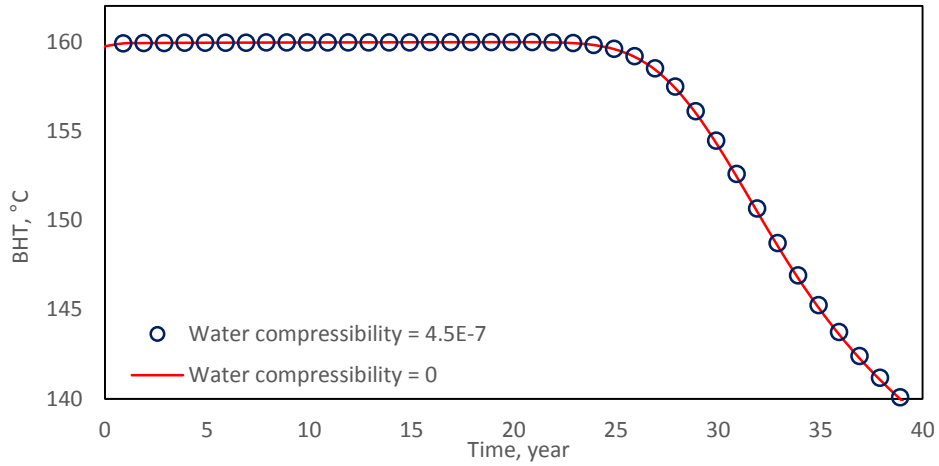

Figure 5-1 Effect of compressibility of water on temperature behavior at production well.

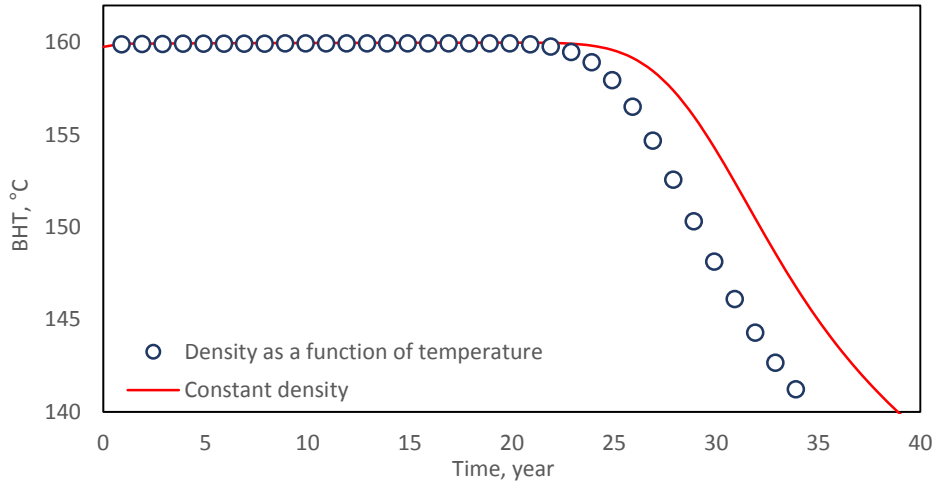

Figure 5-2 Effect of water density on temperature behavior at production well.

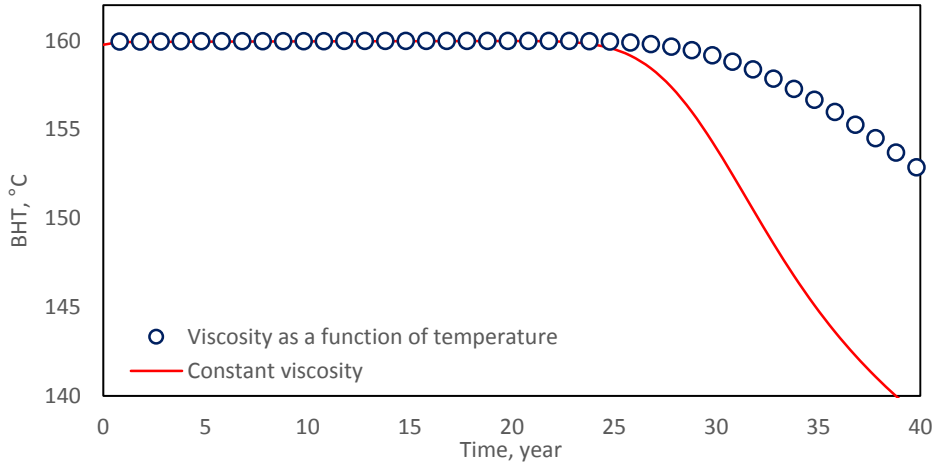

Figure 5-3 Effect of water viscosity on temperature behavior at production well.

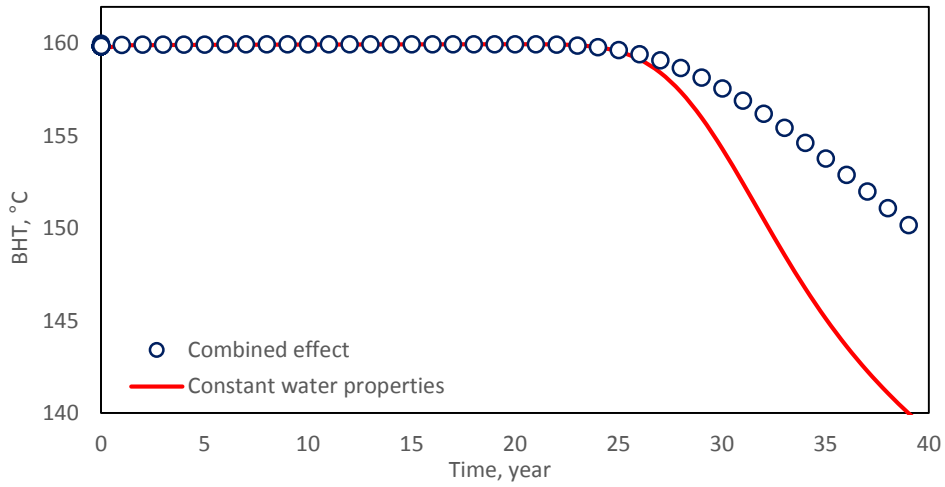

Figure 5-4 Combined effect of compressibility, density and viscosity of water on temperature behavior at production well.

5.2 Effect of thermal properties of rock – compressibility, thermal conductivity and heat capacity

Rock compressibility as well as water compressibility has little impact on the thermal breakthrough time (Figure 5-5) if they are in the typical range of values at reservoir conditions. Figure 5-6 shows the effect of thermal conductivity of rock. Representative values for typical sandstone (sedimentary rock) and andesite (igneous rock) are fed into the simulation model and there is no considerable change on the thermal breakthrough time (Figure 5-6) as it is already discussed in Section 4.4. Effects of heat capacity of different rocks – sandstone, limestone and kaolinite on thermal breakthrough time are also compared.

Figure 5-7 shows that the higher heat capacity, the longer thermal breakthrough time. This is what we can expect from the Gringarten and Sauty solution in which thermal breakthrough time is a function of the ratio of reservoir heat capacity to water heat capacity. With given heat capacity of water, the heat capacity of rock defines thermal performance of a geothermal reservoir. Therefore, heat capacity of reservoir rock plays a significant role in retarding the advancement of the thermal front.

All other things being equal, it is expected that carbonate reservoirs would have a longer lifetime than sandstone reservoir. Interestingly, high heat capacity of shale content (kaolinite) could help retard the thermal breakthrough time. This could imply that stratigraphic reservoir with shale bedding could show an improved heat sweep performance. Figure 5-8 shows the temperature behavior of a reservoir model with different initial temperature (160, 200 and 220 ℃) with rock and water properties varying with temperature. The reservoir model with higher initial temperature shows a slightly improved decline, but not evident, in the temperature after breakthrough time. High temperature (above 250 ℃) with under-pressured geothermal reservoir reservoirs could possibly be a two-phase system.

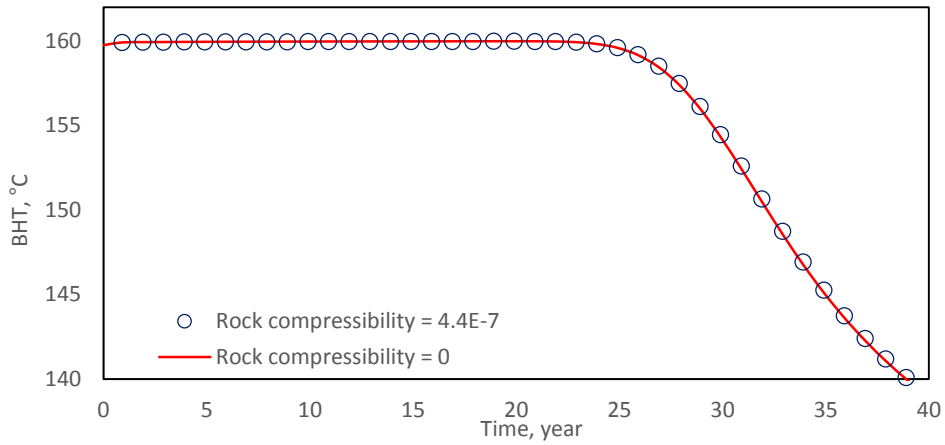

Figure 5-5 Effect of compressibility of rock on temperature behavior at production well.

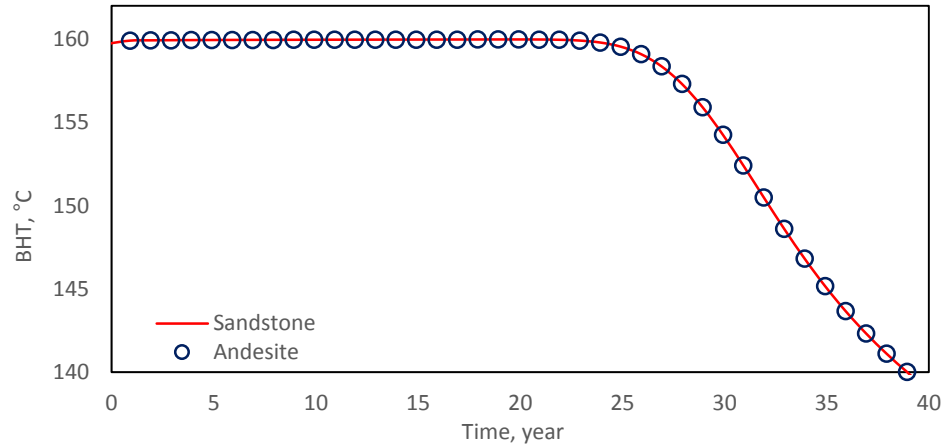

Figure 5-6 Effect of thermal conductivity on temperature behavior at producer – representative value of thermal conductivity for sandstone and andesite is used.

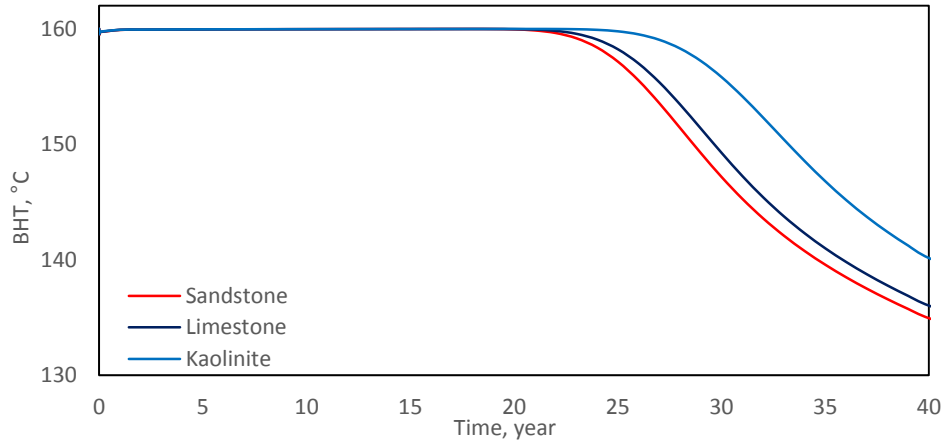

Figure 5-7 Effect of heat capacity on temperature behavior at producer – representative value of heat capacity for sandstone and limestone is used.

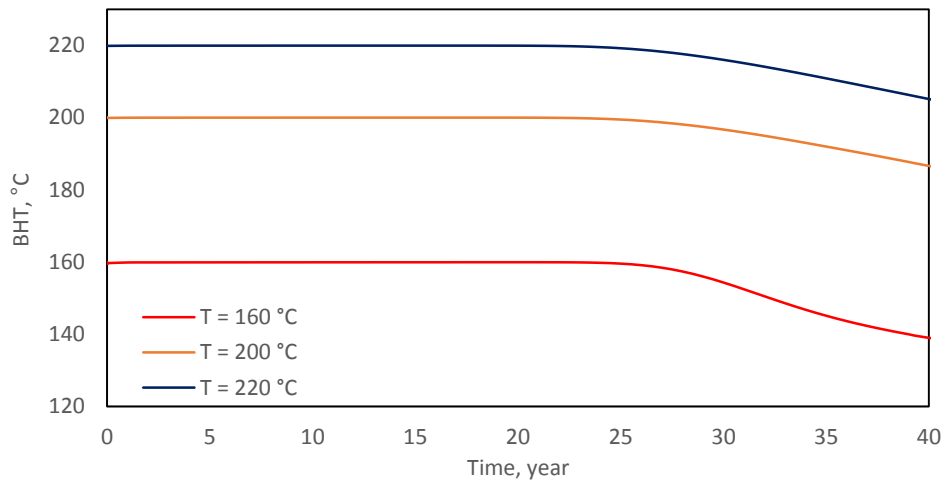

Figure 5-8 Effect of initial reservoir temperature on thermal breakthrough time – rock and water properties varying with temperature.

CHAPTER 6
RESERVOIR SIMULATION STUDY FOR A TARGET FORMATION

Porro and Augustine (2012) suggested the possibility of commercially viable geothermal energy production from sedimentary basins in Colorado. Their work included 15 sedimentary basins in the United States and it concluded that the expected thermal potential in the sedimentary basins is high enough for large scale geothermal energy production. Among the basins discussed in their work, Denver basin is selected for this research.

6.1 Target formation for preliminary simulation study

The Permian Lyons Sandstone in the areas of the Wattenberg field (Figure 6-1) is the target formation for preliminary reservoir simulation; not only because of its relatively high geothermal gradient, but also of abundant well log data in connection with oil and gas activities. Several reservoir parameters of the Lyons Sandstone are summarized in Table 6-1 and lithofacies and the stratigraphy of the formation is shown in Figure 6-2 (Debra and Dave, 2007).

Figure 6-1 Location of the Wattenberg field (http://shaleoilandgas.blogspot.com/2011/04/denver-basinvideo-blog.html).

Table 6-1 The Lyons formation data (http://www.beg.utexas.edu/environqlty/co2seq/co2data/0lyons.htm)

Depth (m)	3,200 to 6,000
Thickness (m)	92
Temperature gradient (℃/km)	30 to 40
Porosity	0.04 to 0.261
Permeability (mD)	0.1 to 3,000
Mineralogy	Well sorted sandstone
Seal rock	Lykins formation

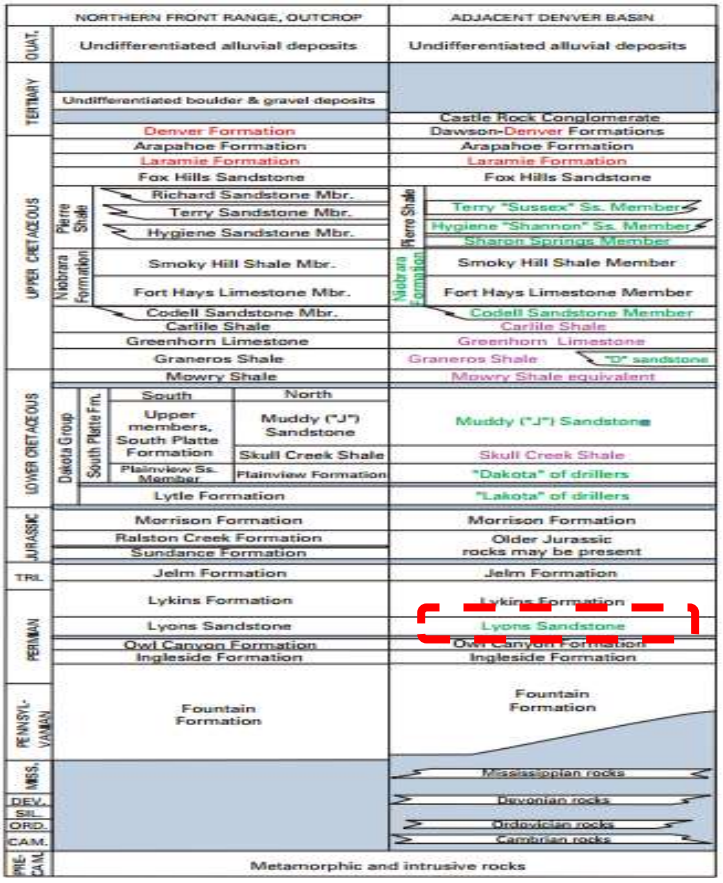

Figure 6-2 Stratigraphic section of rock units in outcrop and the adjacent Denver Basin - The Permian Lyons Sandstone formation is between Lykins and Owl Canyon formation. (http://pubs.usgs.gov/dds/dds-069/dds-069-p/REPORTS/69_P_CH_2.pdf)

6.2 Estimation of geothermal potential

Reservoir simulation models with spatial variation of porosity and permeability are built based on the well log data from the Wattenberg field. The Wattenberg field is well known for oil and gas development and well log data are available from the Colorado Oil and Gas Information System (COGIS: http://cogcc.state.co.us/cogis/). Well log data near the Weld County in the Wattenberg field are collected (Figure 6-3) and the temperature distribution map is generated (Figure 6-4 and Figure 6-5).

In an effort to evaluate the geothermal potential in the area of interest, bottomhole temperature (BHT) data recorded in well log headers are compiled. The BHT data were converted into corrected geothermal gradient using the same approach that Morgan (2009) used in his analysis of the geothermal potential of the Raton basin (APPENDIX A). The area (red circled in Figure 6-5) expected to have a higher geothermal gradient includes Well #12, #13, #14 #15 in Appendix A (Estimation of geothermal gradient). The average gradient is expected at 72 ^{o}C /km, greater than the average geothermal gradient in the Wattenberg field (46 ^{o}C /km: Meyer and McGee 1985). With the geothermal gradient obtained from the

well log data and heat capacity of reservoir water and rock, the electric geothermal potential - a measure of how many megawatts of electric power can be produced from a geothermal field, at a depth of 2.5 km can be approximated.

The electric geothermal potential (G_p) is,

$$Gp = \eta_G \frac{H_G}{t_E} = \eta_G \frac{\rho_s c_p V_b \Delta T}{t_E} \quad [MW_e] \tag{6.1}$$

Using the geothermal gradient (72 °C / km) and the average value of heat capacity (2540 kJ/m^3), the in-place reservoir thermal energy per unit volume is the product of average volumetric heat capacity of the reservoir and the temperature difference between the reservoir and the surface.

$$\frac{H_G}{t_E} = 2540 \text{ kJ/m}^3\text{-°C} \times (180 \text{ °C} - 20 \text{ °C}) = 406 \text{ MJ/m}^3 \tag{6.2}$$

The conversion factor of correlating heat energy in-place with electricity power at the surface power plant is η_G. The proposed value based on the Los Azufres geothermal reservoir in Mexico is around 2.5% (Suarez and Viggiano 1992). Hence, the maximum electric geothermal power density for 30 year's production is,

$$Gp/V_B = 0.025 \times \frac{406 \text{ MJ/m}^3}{30 \text{ year}} \approx 0.01 \text{ W}_e/\text{m}^3 = 10 \text{ MW}_e/\text{km}^3 \tag{6.3}$$

Figure 6-3 Location of wells in the Wattenberg field.

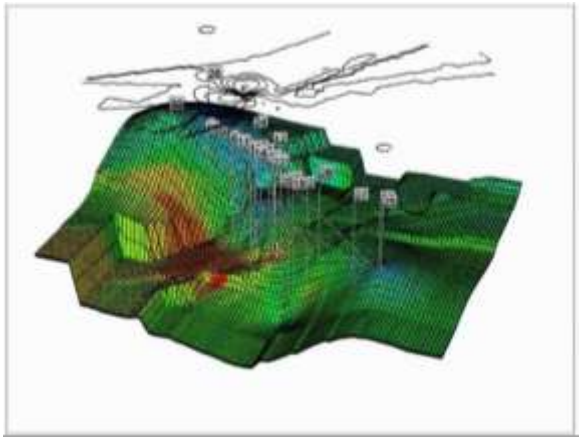

Figure 6-4 Temperature distribution map on the top of the Lyons formation in the Wattenberg field – generated by Kriging using BHT data in well log headers.

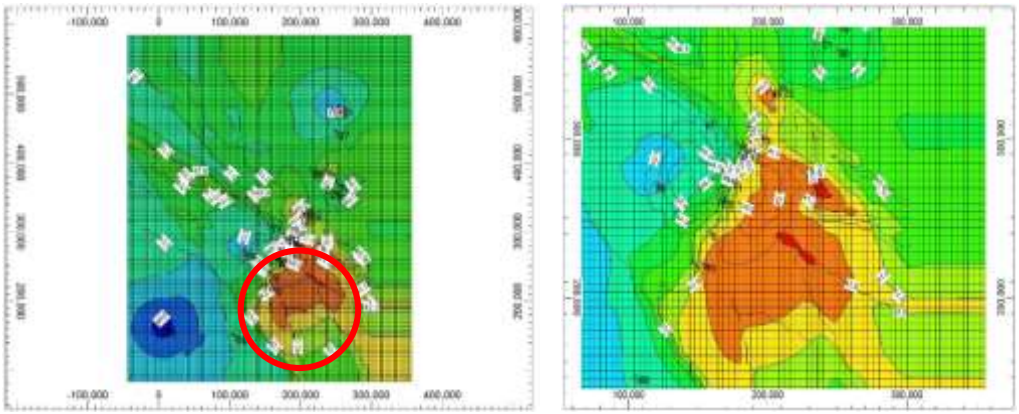

(a) (b)

Figure 6-5 Temperature map on the top of Lyons formation in the Wattenberg field (a) and high thermal potential area zoomed (b).

6.3 Reservoir modeling

The base simulation model is built based on the log of Well # 15. For the porosity and permeability realization, Well # 12, #13 and #14 are used additionally. The reservoir size is established such that pressure at the boundary is not significantly affected by no-flow boundaries. Figure 6-6 shows the log of Well #15 at depths from 2591m (8500 ft) to 2699 m (8850 ft). The initial formation temperature is 171 ºC (330 ºF) based on the Generalized Bottomhole Temperature (GTEM) in the log. A water bearing sand zone with its thickness of 110 m can be identified based on resistivity, GR (gamma ray) and PEF (Photo Electric Factor). Average porosity is estimated at 0.08. Porosity distribution is generated using geo-statistical method (sequential Gaussian simulation) based on the neutron porosity in the well log. The porosity distribution honors the neutron porosity log at Well #15 but does not fully represent spacial variation as it moves away from the well. Permeability is updated based on the simulated porosity distribution using Kozeny-Carman

type correlation as given in Eq. 6.4 (CMG geostatistical modeling tutorial, 2013). The porosity and permeability distribution of the base model is shown in Figure 6-7.

$$k = 3000 \times (\phi + 0.1)^3 / (1-\phi)^2 \quad (6.4)$$

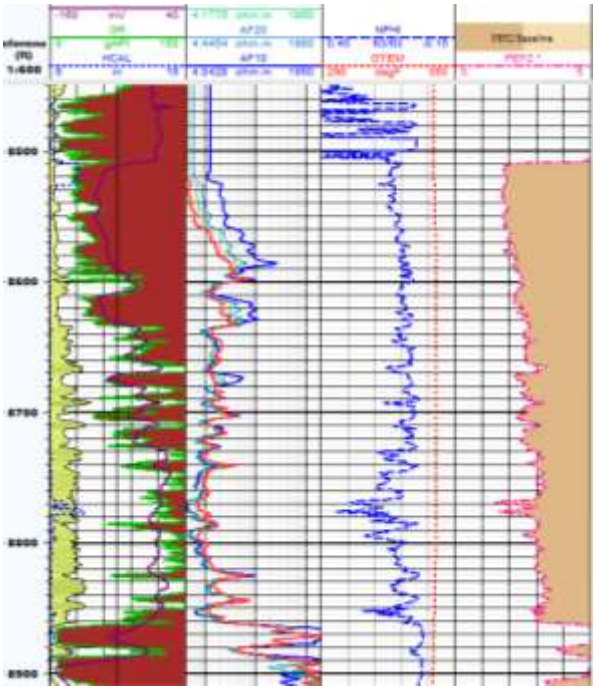

Figure 6-6 Well log (# 15) of the target formation - gamma ray, resistivity, neutron porosity and generalized borehole temperature.

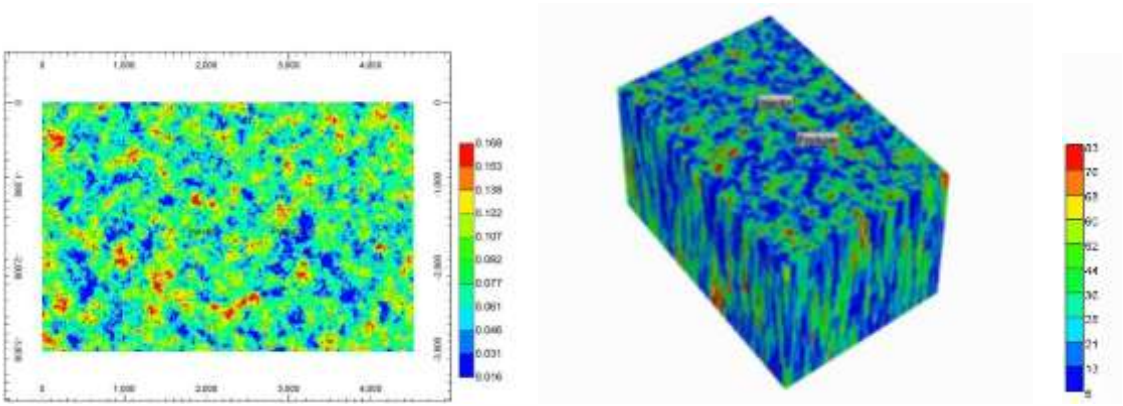

(a) (b)

Figure 6-7 Porosity (a) and permeability (b) realization using sequential Gaussian simulation from the neutron porosity of well log.

The base simulation model parameters are listed in Table 6-2. The internal default values of water properties are used so that they change as a function of temperature and pressure. Rock properties are

representative of typical sandstone reservoirs. The temperature gradient is constant for the given depth and normal hydrostatic pressure is assumed. The model assumptions are the followings,

- All the produced water is re-injected to the injection well,
- Injection and production well are pump-operated at a constant rate of 8068 m^3/day at the surface,
- No pressure and heat loss in wellbore,
- No other operational constraints on the injection and production, unless otherwise specified,
- Fully perforated along the entire reservoir height.

In addition to the base model, 3 different well patterns; openhole horizontal well, doublet with vertical hydraulic fracture at each well, and horizontal well with longitudinal hydraulic fracture at each well are studied in terms of thermal and hydraulic performance. The hydraulic fractures are modeled in an explicit way using local grid refinement.

Table 6-2 Base case model (doublet) parameters

Grid type and resolution (m)	Cartesian 20 - 20 - 10
Time-step (day)	30
Reservoir dimensions (m)	4500 – 3000 - 110
Well spacing (m)	1000
Top depth of reservoir (m)	2591
Porosity (fraction)	Min value: 0.015795 Max value: 0.168008 Average: 0.08245659
Permeability I and J (mD)	Min value: 4.80861 Max value: 83.43076 Average: 25.10615
Permeability K (mD)	0.1×Perm I
Rock compressibility (1/kPa)	4.50E-07
Volumetric rock heat capacity (J/m^3-k)	2.38E+06
Rock thermal conductivity (J/m-day-C)	1.50E+05
Injection/production rate (kg/day)	8068
Initial reservoir temperature (ºC)	171
Initial reservoir pressure (kPa)	25778.5
Injection temperature (ºC)	80
Horizontal well length	1000
Fracture half length	500
Dimensionless fracture conductivity	20

6.4 Reservoir performance

As previously discussed in Section 3.3.1, hydraulic performance of a geothermal doublet can be evaluated by a productivity index. The average productivity index of the simple doublet model at the production side is 0.72 L/bar-s (Figure 6-8). With no operational constrains on the injection or production pumps, it is likely that the simple doublet configuration is marginally sub-commercial because such low productivity index – less than 1L/bar-s, forces the pumps to operate out of their optimal range of operation, resulting in significant decrease in their efficiency. If more realistic operational conditions are imposed considering the optimal operational range of the pumps, the injection well pressure build-up and the production well pressure drawdown are limited to 6,892 kPa (1,000 psi) and 3446 kPa (500 psi), respectively (Butler et al., 2004). Based on these constraints, the system would not be able to achieve the target flow rate (8068 m^3/day) as in Figure 6-9.

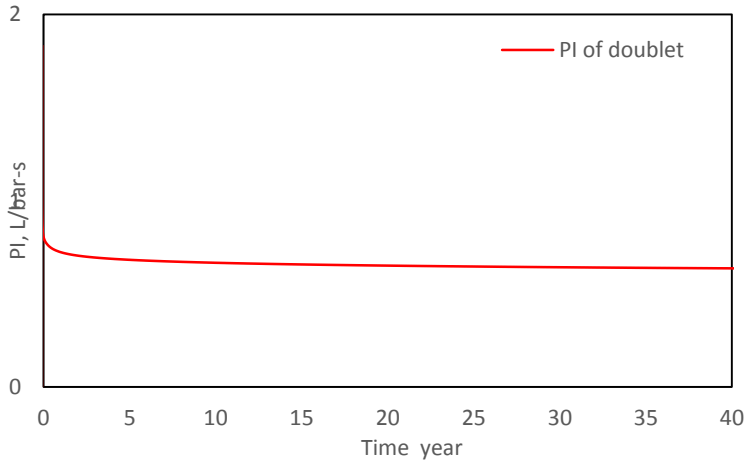

Figure 6-8 Productivity index (PI) for the base case (doublet) with no operational constraints.

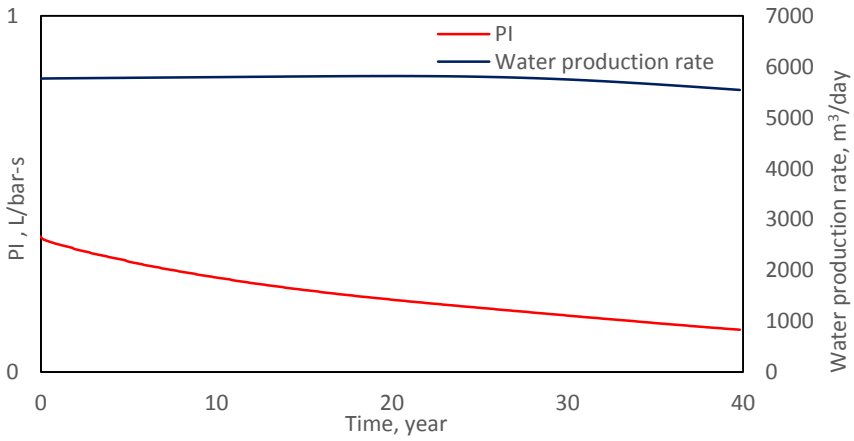

Figure 6-9 Production rate and pressure for the base case (doublet) with operational constraints imposed on the injection and production well pump.

The evolution of heat front over reservoir lifetime for the base model (doublet) is shown in Figure 6-10. The variation in porosity and permeability makes the heat front unstable and the permeability contrast induces a localized channeling effect which lowers the heat sweep efficiency, making the thermal breakthrough time slightly earlier. The thermal breakthrough time of the base model 18 is years (at 170 °C), which is shorter than the desired geothermal lifetime (30 years). However, considering the operational range of a binary power plant at the surface, we assume that the minimum inlet temperature is 161 °C (maximum temperature drop is 10 °C), and then the geothermal reservoir can operate up to 30 years of lifetime.

In sum, the base model is able to operate for 30 years and its average productivity index at the production well is 0.72 L/bar-s. This indicates that the base model, for the given conditions, satisfies the thermal criterion (30 year) but its hydraulic performance is not able to meet the target flow rate. Hence, there is a need of technology for enhancing the productivity index. Horizontal well, higher pump efficiency, lower pump setting depth and well bore insulation against heat loss could be considered. In addition, various stimulation technologies such as hydraulic, thermal and chemical stimulation can enhance the productivity index.

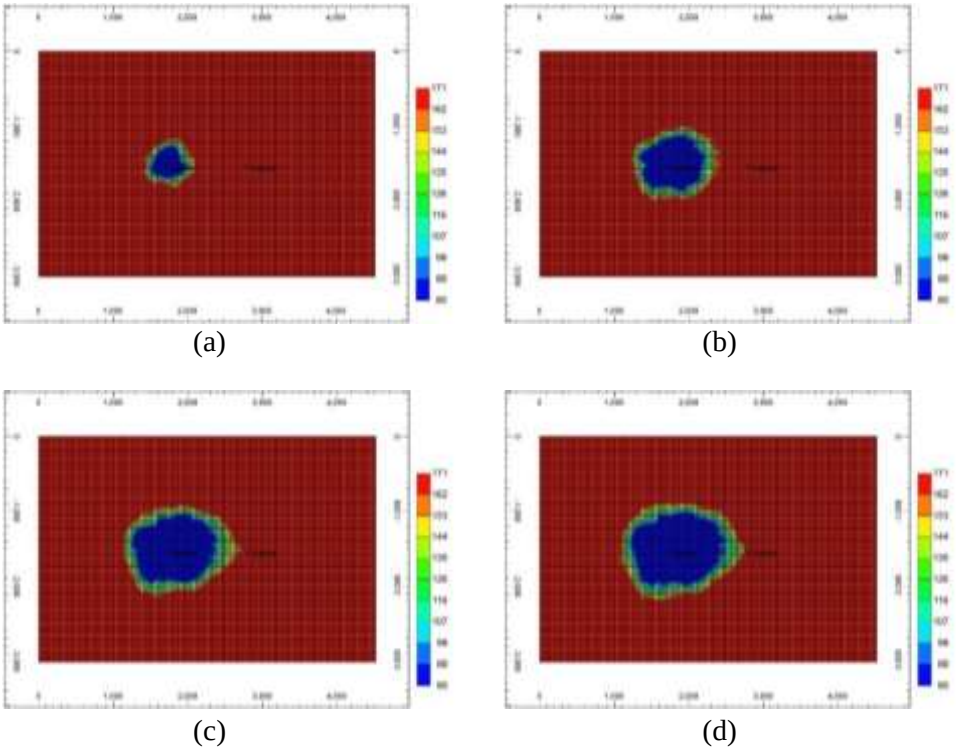

(a) (b)

(c) (d)

Figure 6-10 Heat front evolution for a doublet model over reservoir lifetime – 5 year (a), 15 year (b), 25 year (c) and 30 year (d).

Improving PI and heat sweep efficiency result in more heat energy produced from a reservoir performance perspective. In this study, horizontal well, doublet with vertical hydraulic fractures and horizontal well with longitudinal hydraulic fractures are studied to see how they improve the reservoir performance (Figure 6-11).

- Vertical wells doublet with hydraulic fractures (Figure 6-11 (a)).
  Fracture half-length is 500 m and height is 110 m
- Horizontal wells with open-hole completion (Figure 6-11 (b)).
  Length of horizontal wells is 1000 m.
- Horizontal wells with longitudinal hydraulic fracture (6-11(c)).
  Length of horizontal wells is 1000 m, and height of longitudinal fracture is 110 m along the length of the horizontal well.

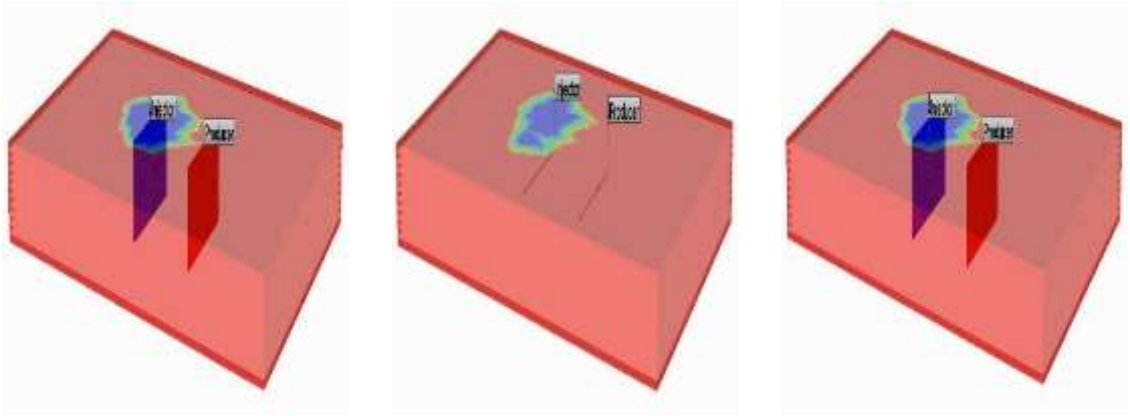

(a) (b) (c)

Figure 6-11 Well configurations of the reservoir enhancement techniques – (a) vertical wells doublet with hydraulic fractures, (b) horizontal wells with open-hole completion and (c) horizontal well with longitudinal fracture.

When it comes to the modeling of hydraulic fractures at each well, only a simple tensile hydraulic fracture using local grid refinement is considered. The reservoir productivity index, improvement factor (the ratio of original productivity index to improved productivity index) with respect to the simple doublet model and thermal breakthrough time of each model are summarized in Table 6-3. Cumulative heat produced per unit rock volume and heat recovery are listed in

Table 6-4. Figure 6-12 shows the productivity index (PI) at the production well, and Figure 6-13 shows the thermal evolution over time for each model. Reservoir stimulation and horizontal well help improve reservoir hydraulics. The average productivity index of the simple doublet model is 0.72 L/bar-s. The vertical hydraulic fracture, horizontal well, horizontal well with longitudinal fracture increase the PI by 2.58, 2.97 and 7.5 L/bar-s times, respectively.

As seen in from Figure 6-14 to Figure 6-16, it is evident that horizontal well and tensile fractures make the heat flow between the wells linear. The linear heat front propagation not only delays thermal breakthrough time but also improves heat sweep between the wells, resulting in the increase in cumulative heat energy produced for 30 years of reservoir lifetime. The horizontal well with longitudinal hydraulic fractures shows the best performance in terms of heat production for the given lifetime (Table 6-4).

Table 6-3 Average productivity index, improvement factor and thermal breakthrough time

MODEL	Average PI (L/bar-s)	PI Improvement factor	Thermal breakthrough time (at 170 °C) (year)
Doublet	0.72	-	18
Doublet fractured	1.86	2.58	20
Horizontal	2.14	2.97	25
Horizontal fractured	5.4	7.5	28

Table 6-4 Cumulative heat per unit volume for 30 years and heat recovery factor for each model

MODEL	Heat in-pace (MJ/ m^3)	Cumulative Heat produced per unit volume for 30 years (MJ/ m^3)	Heat recovery (%)
Doublet	367.0	35.181	9.586
Doublet fractured		35.379	9.640
Horizontal		35.635	9.710
Horizontal fractured		35.688	9.724

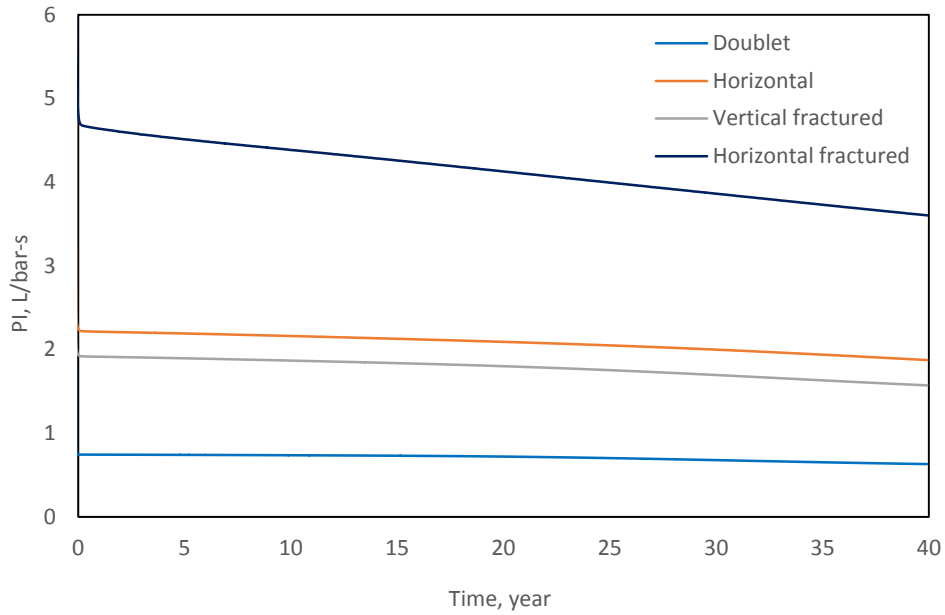

Figure 6-12 Productivity index for the models in Table 6-3.

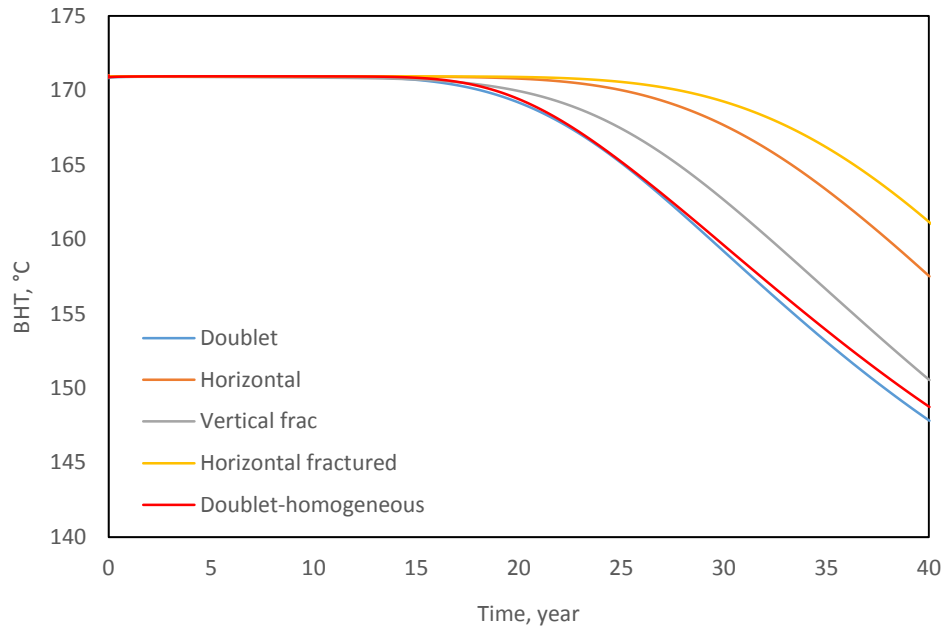

Figure 6-13 BHT at production well for the model in Table 6-3 and the BHT of the homogeneous doublet model is included for comparison (red).

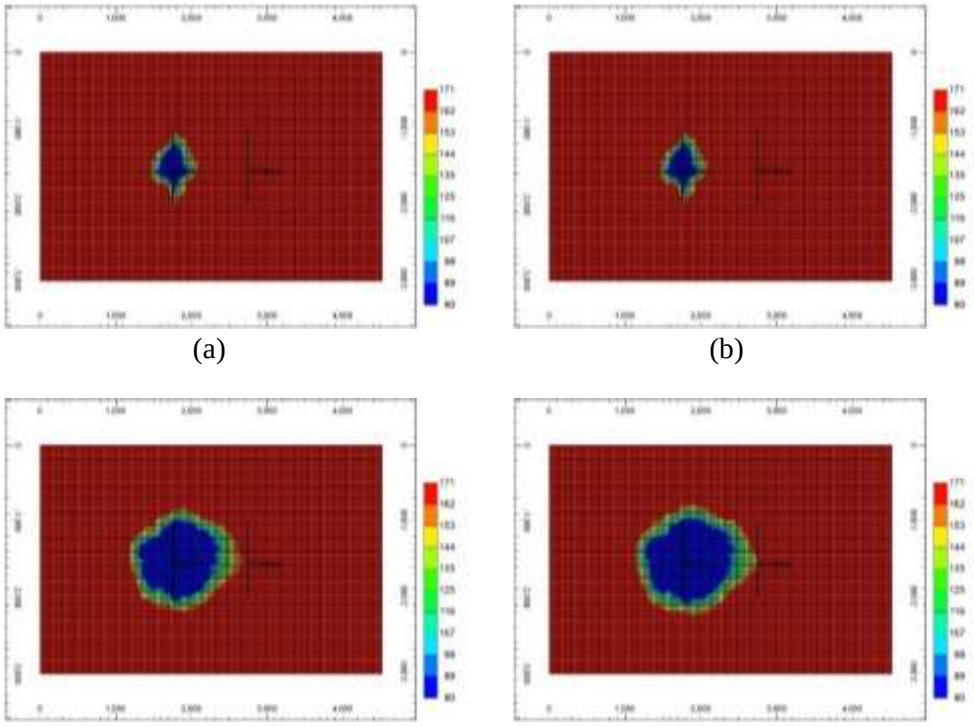

Figure 6-14 Heat front evolution for doublet with hydraulic fracture – 5 year (a), 15 year (b), 25 year (c) and 30 year (d).

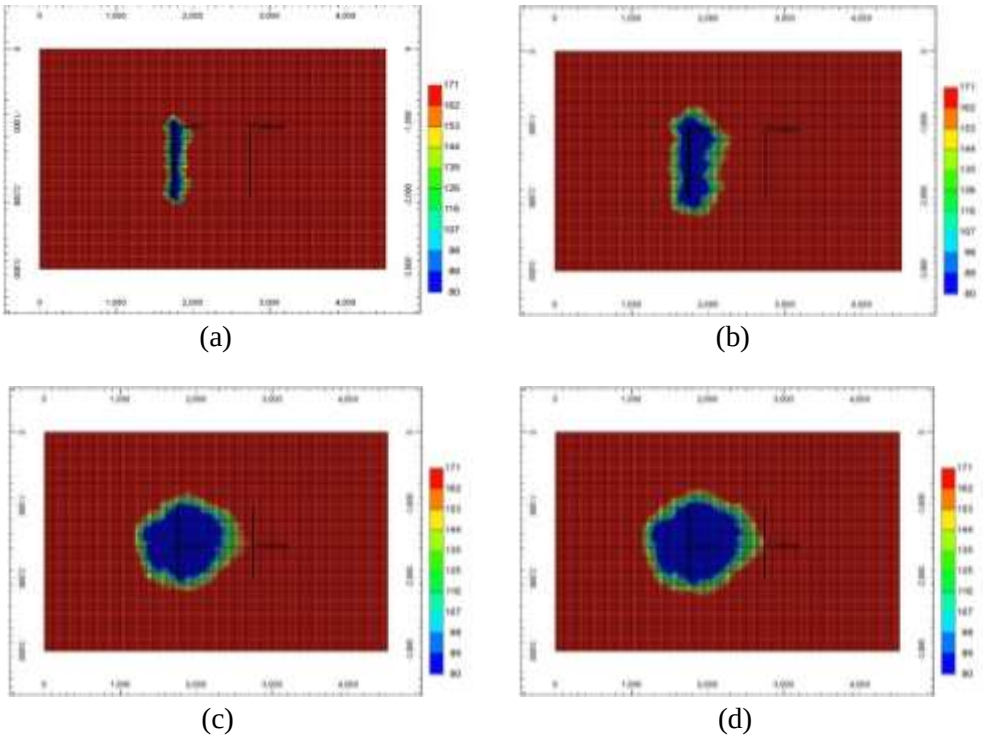

(a) (b) (c) (d)

Figure 6-15 Heat front evolution for horizontal well model over reservoir lifetime – 5 year (a), 15 year (b), 25 year (c) and 30 year (d).

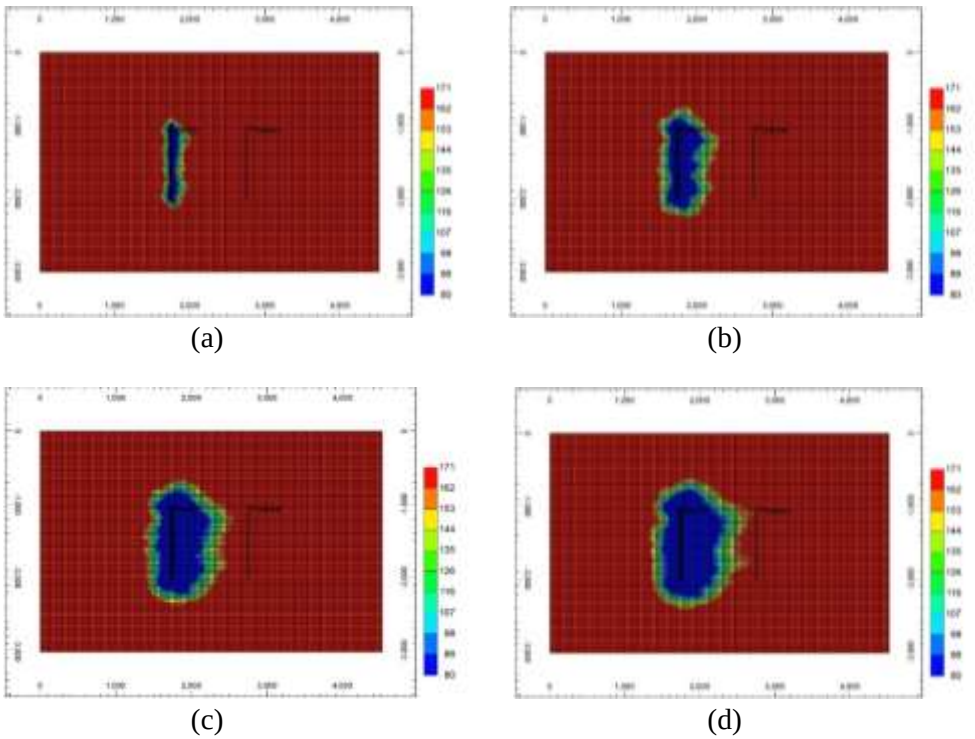

(a) (b) (c) (d)

Figure 6-16 Heat front evolution for horizontal well with longitudinal hydraulic fracture – 5 year (a), 15 year (b), 25 year (c) and 30 year (d).

6.5 Overburden/underburden effect

The advancement of a thermal front is retarded by the heat provided from cap and bed rocks as well as reservoir rocks (Figure 6-17). It is obvious that the heat from the cap rock and bed rock helps prevent premature thermal front breakthrough, delaying the advancement of a thermal front. The amount of heat transferred into the reservoir depends on thermal properties of rocks including heat capacity and thermal conductivity. The higher values of heat capacity and thermal conductivity of rocks are, the more amount of heat is transferred and the longer thermal lifetime of geothermal systems.

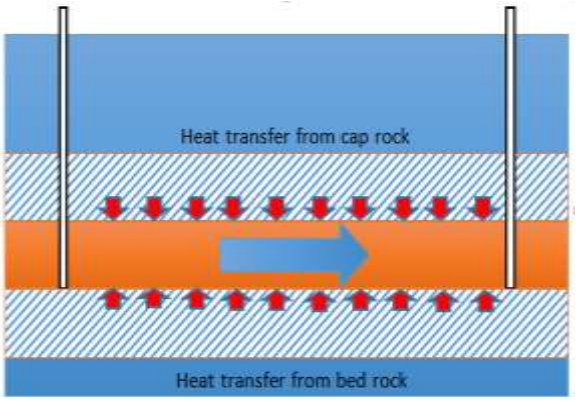

Figure 6-17 Heat transfer from the overburden and underburden.

A new simulation model with overburden and underburden between the reservoir layers is built to account for heat loss. The cap and bed rock are modeled as low permeability layers (0.1 mD). It is assumed that cap/bed rocks have the same thermal properties; heat capacity and thermal conductivity. Basic parameters are summarized in Table 6.5. Three doublet models with different layers are tested: Model A with no overburden and underburden, Model B with 5 layers of overburden and underburden, and Model C with high permeability short circuiting layers (200 mD) at the center (Table 6-6). Figure 6-18 shows the layer configuration of each model.

The thermal propagation and isosurface map of each model are shown from Figure 6-19 to Figure 6-21. Model B (Figure 6-20) and Model C (Figure 6-21) show that the heat in the overburden and underburden is being swept by the fluid flow in the high permeability reservoir zone while Model A (Figure 6-19) has no heat transfer between the overburden and underburden and the reservoir layers. Particularly for Model B, the additional heat from the overburden and underburden retards the propagation of the heat front and improve the BHT decline past its thermal breakthrough time (Figure 6-22). The amount of heat energy swept per unit volume for 30 years from the overburden and underburden is 0.187 MJ/m^3. The short-circuiting model (Model C) shows the worst thermal performance with its temperature at 151 after 30 years and the cumulative energy produced is 1.67 MJ/m^3 less than that of Model B. Especially, the thermal breakthrough time is reduced to 7 years, 10 years shorter than Model B (Table 6-7).

Table 6-5 Basic parameters for overburden and underburden heat loss model

Grid type	Cartesian
Grid resolution (m)	20 - 20 – 10 (aquifer) 20 – 20 – 20 (cap/bed)
Time-step (day)	Simulator default
Reservoir dimensions (m)	4500 – 3000 – 310 Overburden: 100 m (5 layers) Underburden: 100 m (5 layers)
Top depth of reservoir (m)	2491
Porosity (fraction)	0.1
Permeability I and J (mD)	reservoir: 25 mD cap/bed: 0.1 mD
Permeability K (mD)	0.1×Perm I
Well perforation	6 – 16 layers

Table 6-6 Permeability layers for Model A, B and C

MODEL	Description	Permeability
A	Without overburden and underburden	1-5 and 17-21 layers : NULL 6-16 layers: 25 mD
B	With overburden and underburden	1-5 and 17-21 layers : 0.1 mD 6-16 layers: 25 mD
C	Short circuit	1-5 layers: 0.1 mD, 17-19: 200 mD 6-9 and 13-16 layers: 25 mD

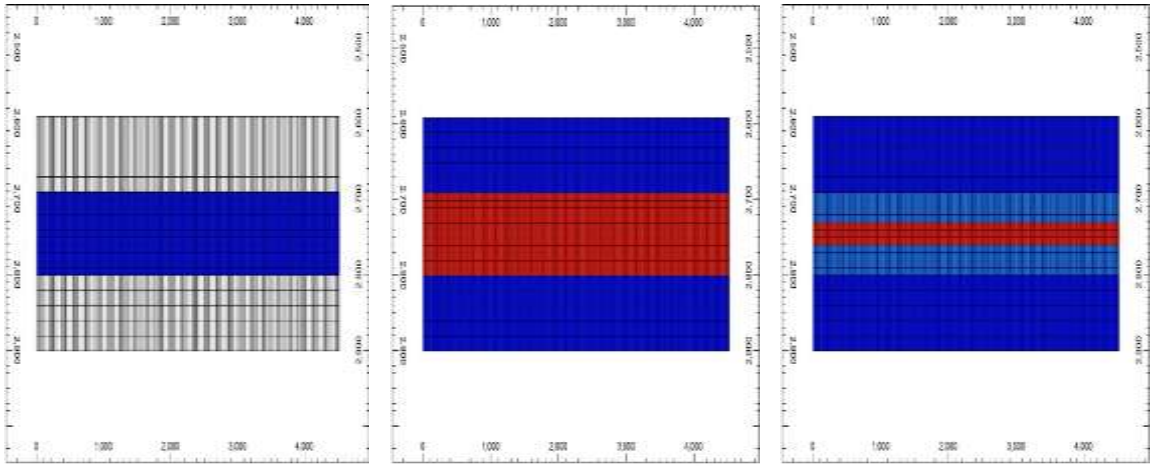

(a) (b) (c)

Figure 6-18 Doublet without overburden and underburden (a), doublet with overburden and underburden (b), and short circuit model with a 200 mD high permeability zone in 17 to 19 layers (c).

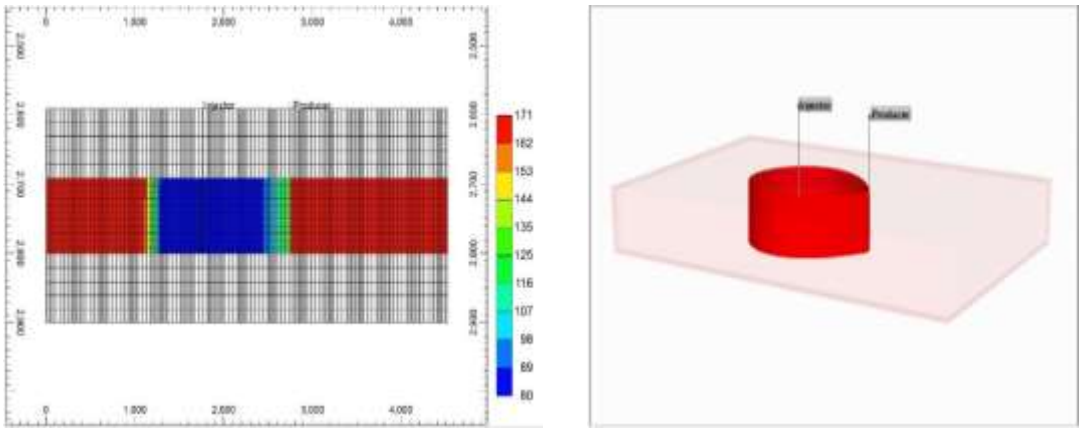

(a) (b)

Figure 6-19 Model A - thermal evolution (a) and isosurface map of 161 °C (b) after 30 year.

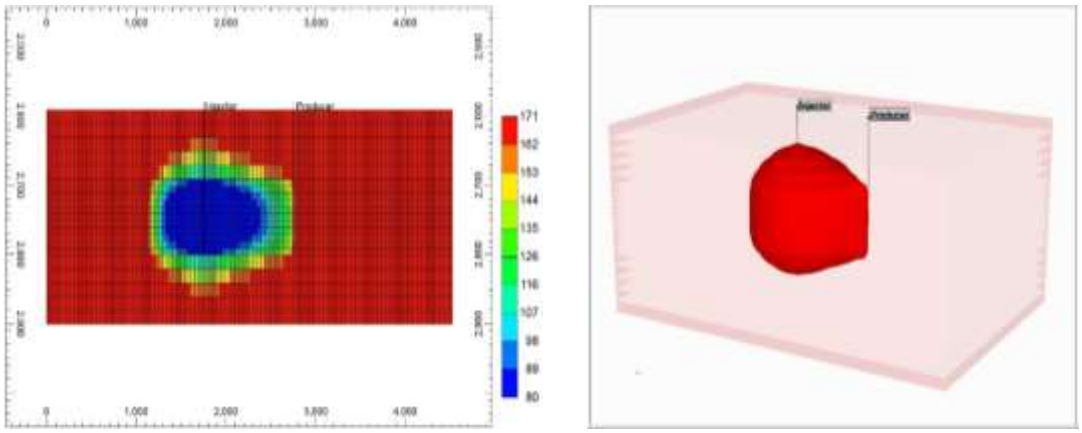

(a) (b)

Figure 6-20 Model B – thermal evolution (a) and isosurface map of 161 °C (b) after 30 year.

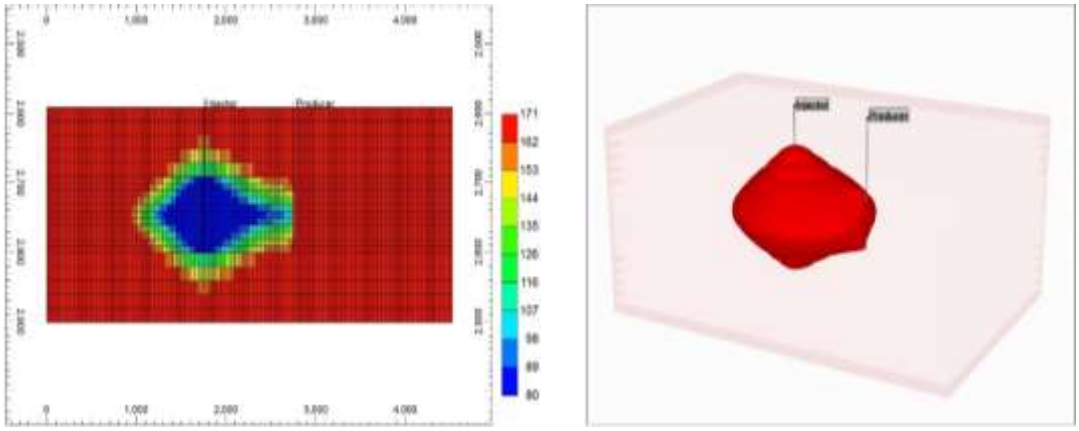

(a) (b)

Figure 6-21 Model C – thermal evolution (a) and isosurface map of 161 °C (b) after 30 year.

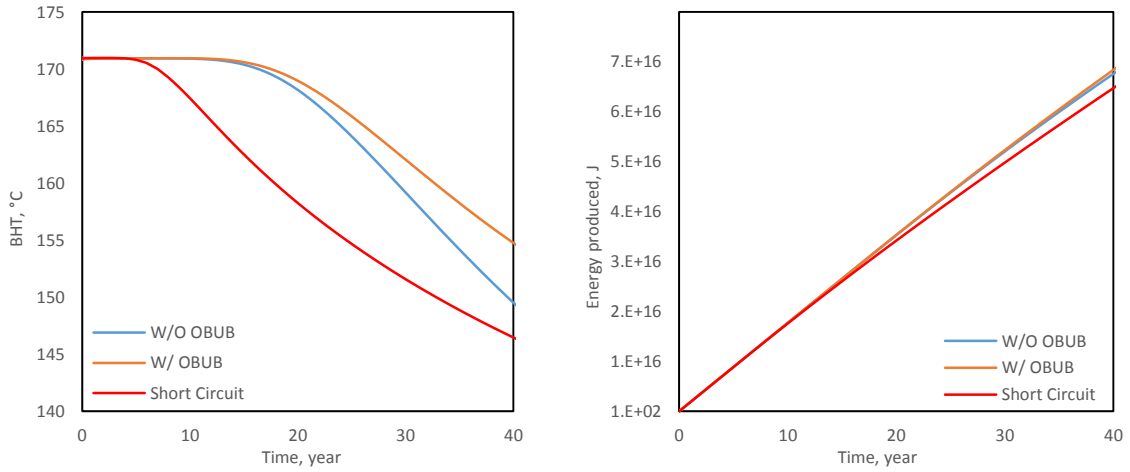

(a) (b)

Figure 6-22 Plot of BHT at the production well location as function of time (a) and cumulative energy produced (b) for model A, B and C.

Table 6-7 BHT after 30 years and cumulative energy per unit volume produced for Model A, B and C

MODEL	Description	Thermal breakthrough time (at 170 °C) (year)	Cumulative energy produced per unit volume for 30 years (MJ/m^3)
A	No overburden/underburden heat transfer	16	35.071
B	Overburden/underburden heat transfer	17	35.258
C	Short-circuiting	7	33.578

6.6 Effect of reservoir stimulation or natural fractures

The conductivity of the target formation is not enough to meet the target flow rate for commercial power generation as the average productivity index for a simple doublet configuration is less than 1 L/bar-s. Commercial geothermal reservoirs have a wide range of productivity index, from 1L/bar-s (marginally sub-commercial) to 40 L/bar-s (exceptionally prolific) and the order of 10 L/bar-s is considered good for commercial power generation (Sanyal et al., 2007). Any type of reservoir stimulation which enhances the formation conductivity can help improve productivity index. However, presence of high conductivity conduits – engineered or naturally occurred, has a risk of causing premature thermal breakthrough or short-circuiting, advancing the end of a geothermal system. Therefore, reservoir stimulation should be designed such that it is able to strike the balance between hydraulic and thermal performance of the reservoir.

Previously, simple tensile fractures are considered in the modeling using local grid refinement. However, the bi-wing type hydraulic fractures modeled in an explicit way are not able to capture the hydro-shearing effects – micro-fractures generated or pre-existing micro-fractures rejuvenated by stimulation. The

primary mode of failure, particularly in geothermal applications of hydraulic fracturing, is more of failure in shear than of failure in tension (Cheon, 2013). Figure 6-23 shows microseismic cloud data of Soultz EGS captured during hydraulic fracturing process, and the boundary of the clouds indicate that the cloud area is stimulated. Therefore, the effects of hydro-shearing or pre-existing micro-fractures on fluid flow and heat propagation should be considered in the modeling work. Evaluation of the effects of induced hydraulic fractures is a complex process because it depends on stress regime, mechanical properties of reservoir rocks, hydraulic fracturing design and heterogeneity of reservoirs. It seems, at least up to date, that there is no definite solution to model this complex coupled physical process. For the purpose of the preliminary feasibility study, we use the dual permeability concept to model the induced hydraulic fractures on the assumption that the entire reservoir layers are stimulated. The formulation of the dual permeability model that STARS uses is described in Appendix B (Formulation of dual permeability).

Different from the dual porosity model, the dual permeability model allows fluid and heat to travel not only in the fractures but also in the matrix (Figure 6-24). The simulation input parameters such as fracture effective permeability, fracture porosity and shape factors are calculated on the basis of a constant fracture conductivity (fracture permeability times fracture width). The basic model parameters are listed in Table 6-8 and the fracture input parameters are listed in Table 6-9. It is assumed that fracture spacing is 10 m, fracture permeability in the vertical direction is ignored and well blocks are not fractured. The reservoir layers (from #6 to #16) are model as fractured using dual permeability. Doublet and horizontal well models with a well spacing of 1,000 m are evaluated in terms of PI and thermal breakthrough time. The doublet simulation model is shown in Figure 6-25.

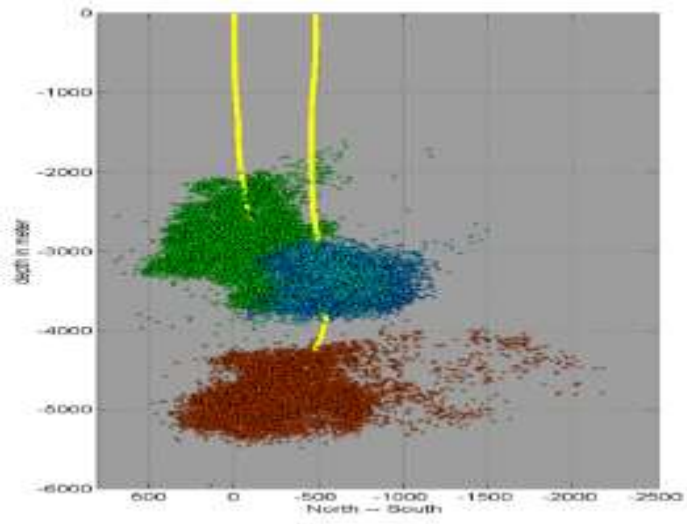

Figure 6-23 Microseismic clouds of stimulation tests of the EGS system of Soultz 1 (Reinhard Jung, 2013).

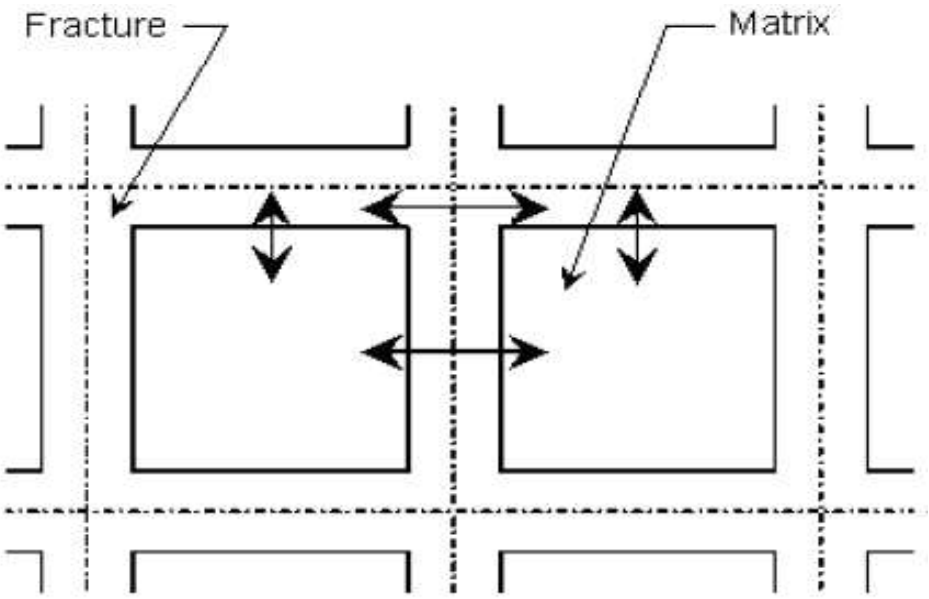

Figure 6-24 Dual permeability model (User's Guide of STARS, 2013).

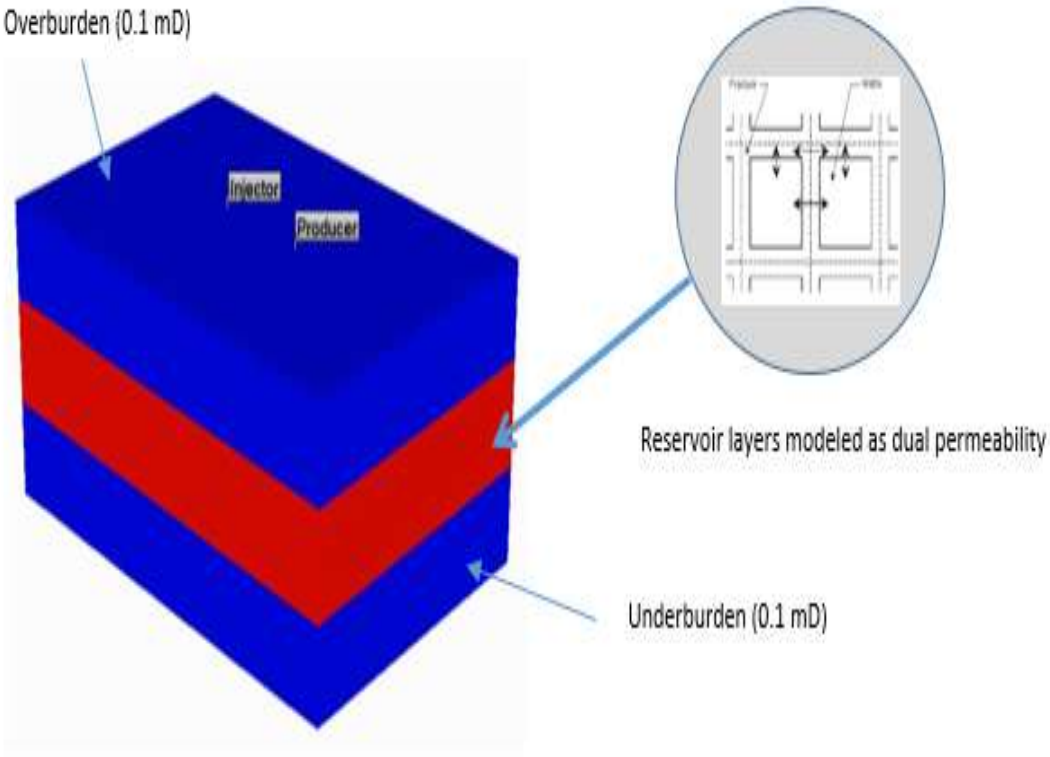

Figure 6-25 Reservoir simulation model – the reservoir layers (red) are modeled as fractured using dual permeability model.

Table 6-8 Modeling parameters of the reservoir simulation model (Figure 6-25)

Grid type	Cartesian
Grid resolution (m)	20 - 20 – 10 (aquifer) / 20 – 20 – 20 (cap/bed)
Time-step (day)	Simulator default
Reservoir dimensions (m)	4500 – 3000 – 310 Overburden: 100 m (5 layers) / Underburden: 100 m (5 layers)
Top depth of reservoir (m)	2491
Porosity (fraction)	0.1
Permeability I and J (mD)	reservoir: 25 mD / cap/bed: 0.1 mD
Permeability K (mD)	0.1×Perm I
Single porosity layers	1 – 5 and 16 – 21 layers
Double porosity/permeability layers	6 – 16 layers
Well perforation	6 – 16 layers

Table 6-9 Fracture input parameters for dual permeability simulation models

Fracture conductivity (D-m)	1	10	100
Fracture spacing (m)	10	10	10
Fracture porosity	6.868 E-5	1.479 E-4	3.187 E-4
Effective permeability (mD)	300	3,000	30,000

The simulation results for a doublet model are summarized in Table 6-10.The models with higher fracture conductivity show an improved productivity index and reduced thermal breakthrough time (Figure 6-26 and Figure 6-27). The productivity improvement factor for the fracture conductivity value of 1 D-m with respect to the model with no fractures in the reservoir layers (base case) is 1.75 with the productivity index of 1.98 L/bar-s and the thermal breakthrough occurs after 15 years of injection. As the fracture conductivity is further increased, the increase in PI and the decrease in thermal breakthrough time become less evident. The thermal evolution of a doublet model with different facture conductivity is shown from a different perspective in Figure 6-28, Figure 6-29 and Figure 6-30.

For the horizontal well models, fracture conductivity plays a significant role (Table 6-11). The productivity index for a model with the fracture conductivity of 100 D-m is increased from 3.19 L/bar-s up to 7.34 L/bar-s but its thermal breakthrough time is significantly reduced from 27 years to 3 years. Figure 6-31 and Figure 6-32 show that the increased fracture conductivity improves the productivity index while it significantly advances the thermal breakthrough time. This is because the horizontal fracture at the center layer (#11) where the horizontal well is located acts as a higher permeability channel and most of fluid flow travels through the fracture, resulting in premature thermal breakthrough time or short-circuiting. The amount of heat extracted from the overburden and underburden is reduced significantly, which exacerbates

the thermal performance. (Figure 6-34 (d)). The thermal evolution of the horizontal models with different facture conductivities are shown in Figure 6-33, Figure 6-34 and Figure 6-35.

Table 6-10 Doublet with 1,000 m well spacing - productivity index, improvement factor, thermal breakthrough time, geothermal lifetime and cumulative energy produced

Fracture conductivity (D-m)	Average PI (L/bar-s)	PI Improvement factor	Thermal breakthrough time at 170 °C (year)	Geothermal lifetime at 161 °C (year)	Energy produced per reservoir volume for geothermal lifetime (MJ/m^3)
-	1.13	-	17	31	36.36
1	1.98	1.75	15	29	33.99
10	2.09	1.85	14	29	33.97
100	2.11	1.87	14	28	32.85

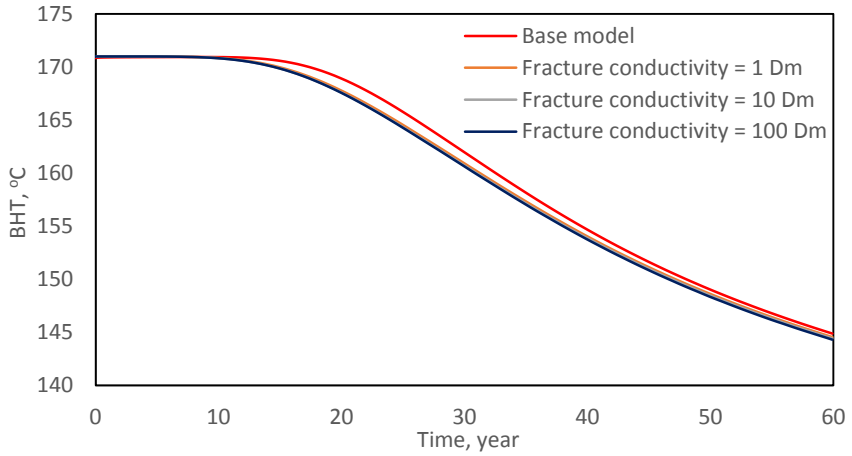

Figure 6-26 BHT at production well for the doublet models with various fracture conductivity of 0 D-m, 1 D-m, 10 D-m and 100 D-m.

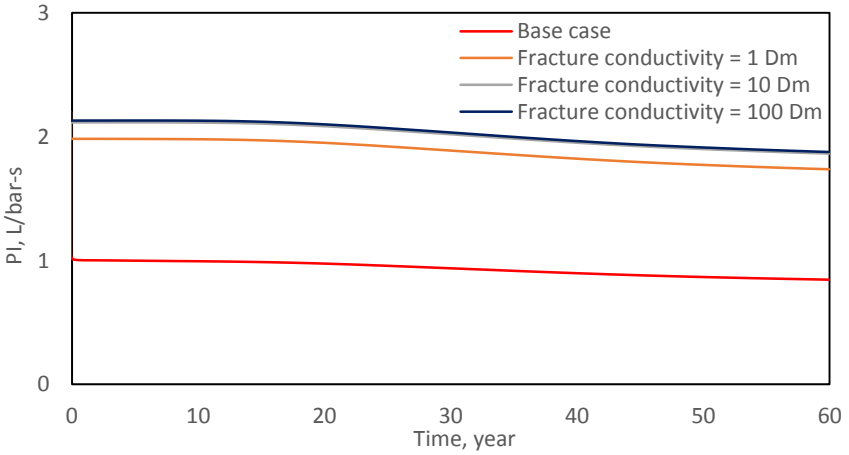

Figure 6-27 PI at production well for the doublet models with various fracture conductivity of 0 D-m, 1 D-m, 10 D-m and 100 D-m.

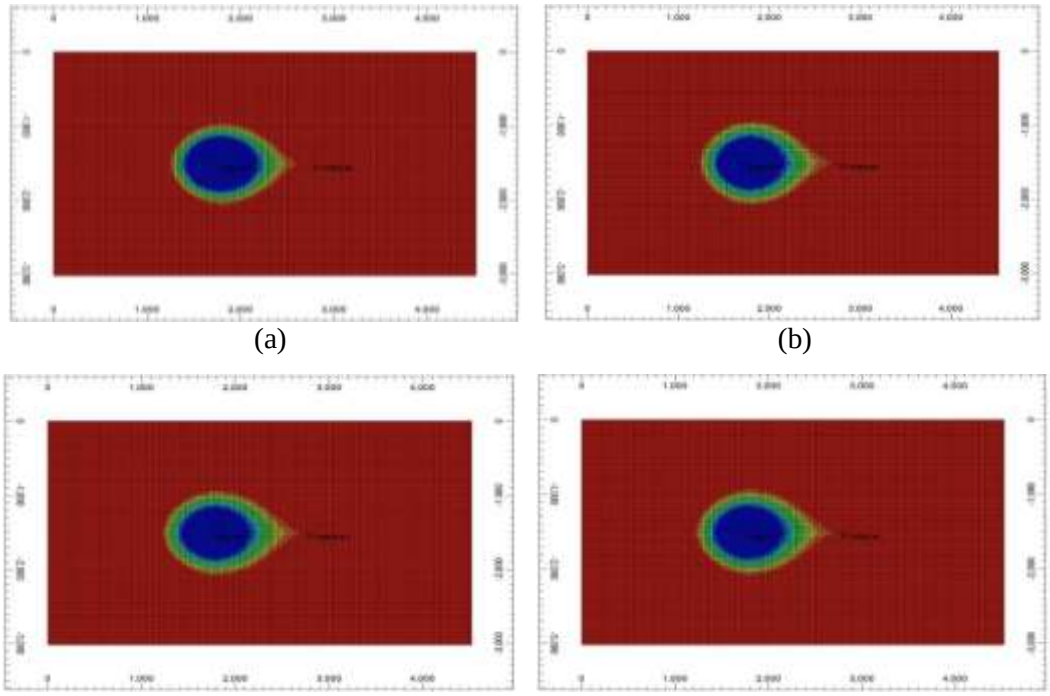

Figure 6-28 Plane view of temperature propagation at the center layer (#11) after 17 years of the doublet model with various fracture conductivity of (a) 0, (b)1, (c) 10 and (d)100 D-m, respectively.

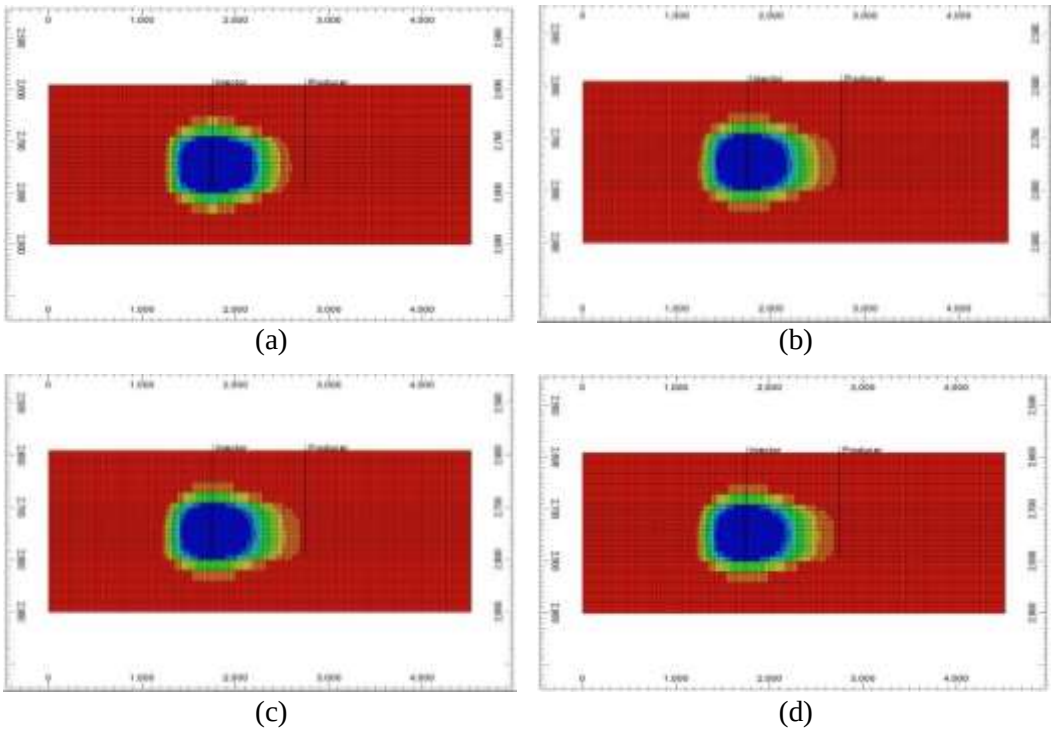

Figure 6-29 Side of temperature propagation at the center layer (#11) after 17 years of the doublet model with various fracture conductivity of (a) 0, (b)1, (c) 10 and (d)100 D-m, respectively.

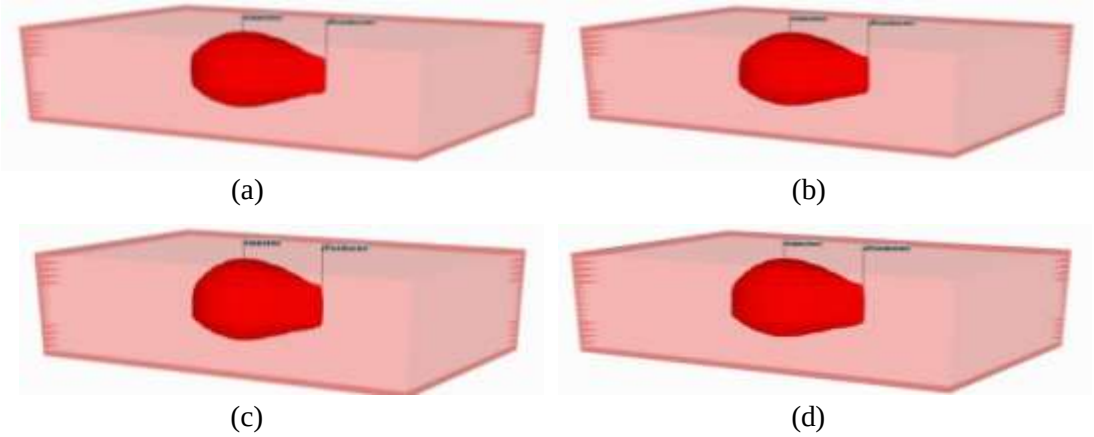

Figure 6-30 Isosurface map of 170 °C after 17 years of the doublet model with various fracture conductivity of (a) 0, (b)1, (c) 10 and (d)100 D-m, respectively.

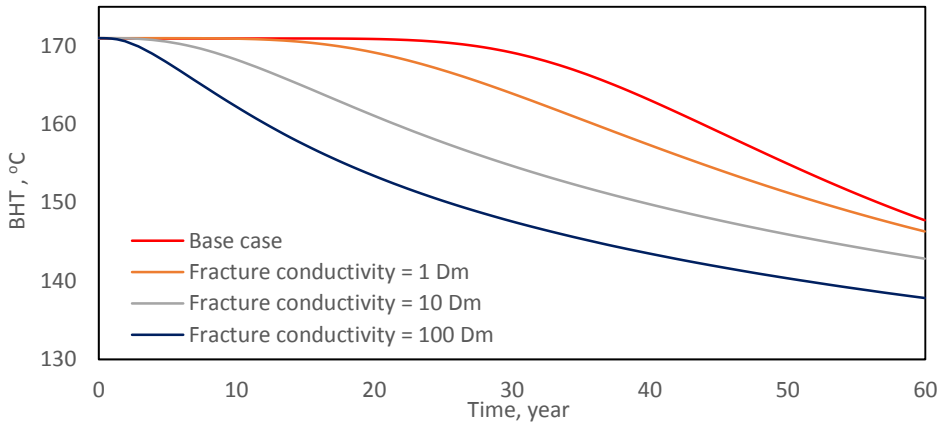

Figure 6-31 BHT at the production well for the horizontal well model with a various fracture conductivity of 0 D-m, 1 D-m, 10 D-m, 100 D-m.

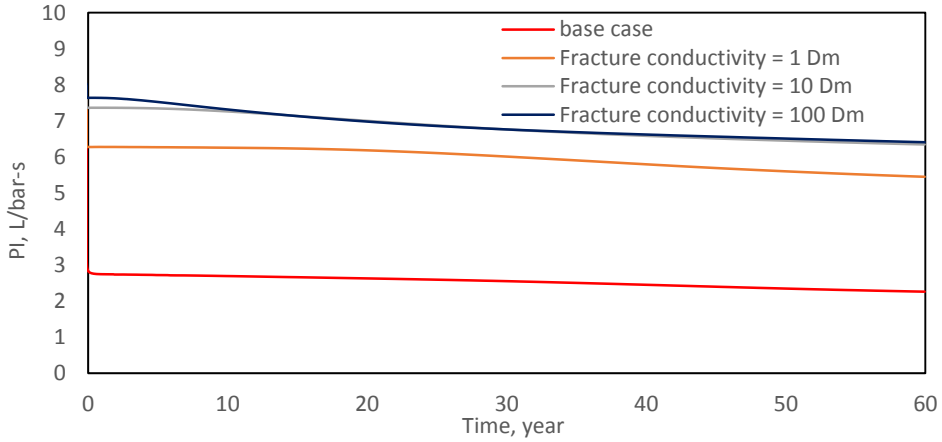

Figure 6-32 PI at production well for the horizontal well model with a various fracture conductivity of 0 D-m, 1 D-m, 10 D-m and 100 D-m.

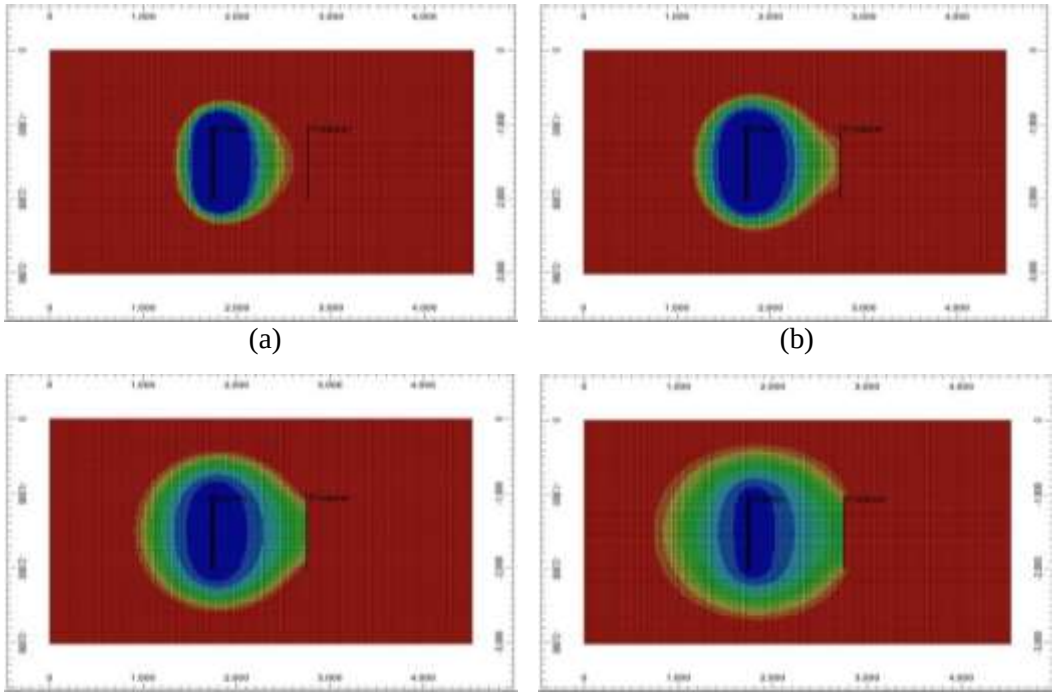

(a) (b)

(c) (d)

Figure 6-33 Plane view of temperature propagation at the center layer (#11) after 27 years for the horizontal well model with a various fracture conductivity of (a) 0 (b) 1 (c) 10 and (d) 100 D-m.

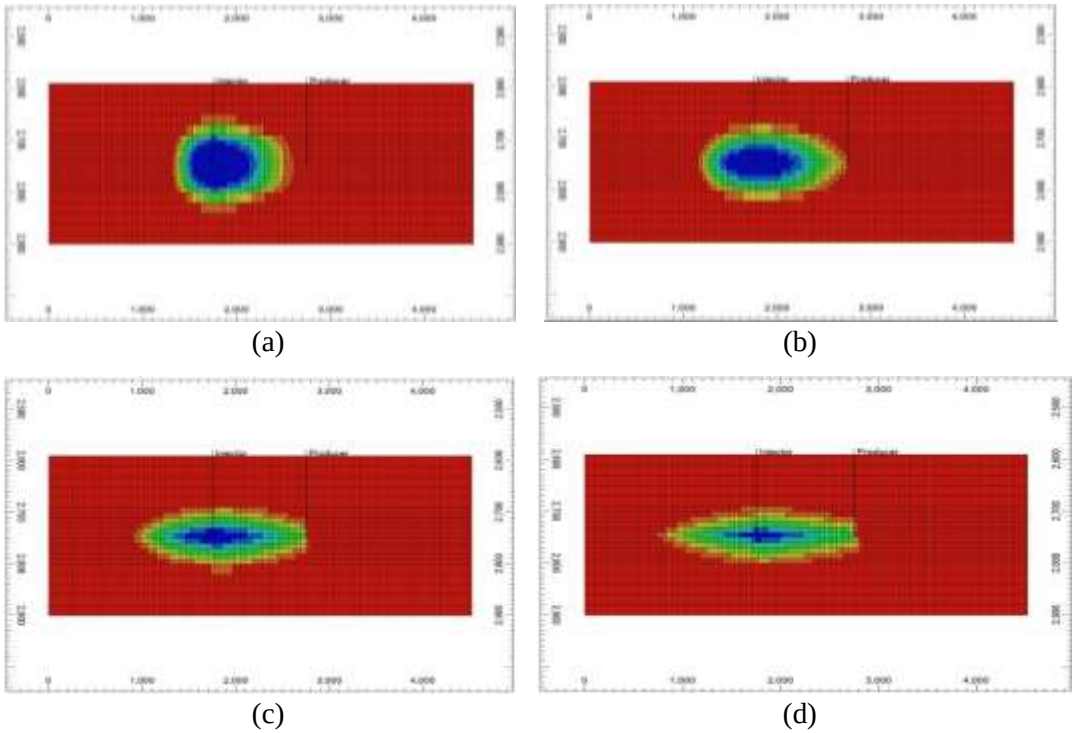

(a) (b)

(c) (d)

Figure 6-34 Side view of temperature propagation at the center layer (#11) after 27 years for the horizontal well model with a various fracture conductivity of (a) 0, (b) 1, (c) 10 and (d) 100 D-m.

Table 6-11 Horizontal well with 1,000 m well spacing - productivity index, improvement factor, thermal breakthrough time, geothermal lifetime and cumulative energy produced

Fracture conductivity (D-m)	Average PI (L/bar-s)	PI Improvement factor	Thermal breakthrough time - at 170 °C (year)	Geothermal lifetime - at 161 °C (year)	Energy produced per reservoir volume for geothermal lifetime (MJ/m^3)
-	3.19	-	27	41	48.37
1	6.25	1.96	17	34	39.84
10	7.17	2.25	6	18	21.01
100	7.34	2.30	3	10	11.60

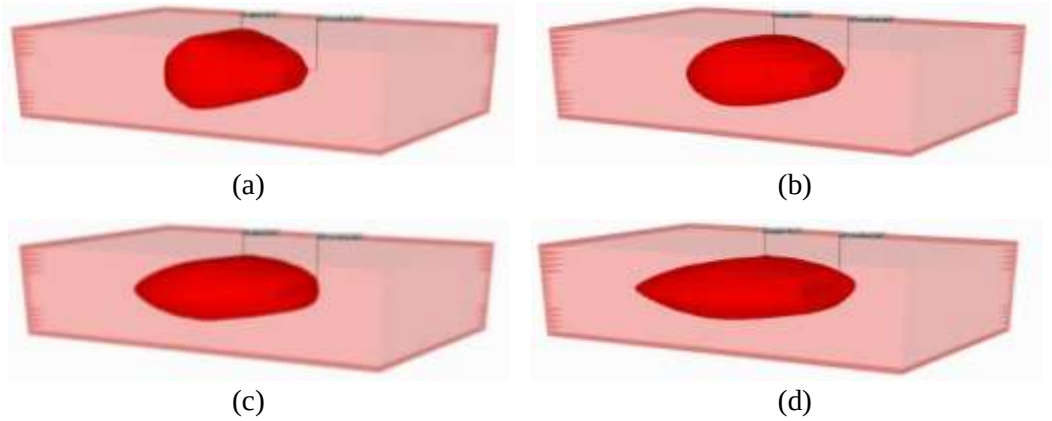

Figure 6-35 Isosurface map of 170 °C after 27 years for the horizontal well model with a various fracture conductivity of (a) 0, (b) 1, (c) 10 and (d) 100 D-m.

The effects of reservoir stimulation are investigated by changing fracture spacing of dual permeability model. Fracture spacing (or element size) determines the shape factor (Eq. B1): larger fracture spacing means a smaller value of shape factor and more flow resistance between the matrix and the fracture. Higher values of shape factor imply that the rocks are effectively stimulated so that the flow path between the fracture and the matrix is secured. Ineffective hydraulic fracturing with low values of shape factor implies that there is less flow from the matrix to the fracture and the entire heat and fluid flow system is dominated more by the fracture flow than the matrix flow. 1 D-m of fracture conductivity is maintained as it balances thermal and hydraulic performance. The simulation results for each model are summarized in Table 6-12 and Table 6-13 and are visualized in Figure 6-36, Figure 6-38 and 39 for the doublet and Figure 6-39, 40 and 41 for the horizontal well model. The thermal and hydraulic performance deteriorate with higher values of fracture spacing. The models with larger fracture spacing shows an extremely sharp decline in bottomhole temperature at production well (Figure 6-36 and Figure 6-39). As for the doublet model with its fracture spacing of 100 m, the initial reservoir temperature (171 °C) immediately declines down to 120 °C and levels off to maintain it for the rest of time. This undesirable early temperature drop is caused by a

low value of shape factor which restricts the heat and mass flow between the matrix and the fracture. Hence, there is less flow from the matrix to the fracture, and the injected cold water travels fast through the fracture at the center layer. This results in premature thermal breakthrough or short circuiting.

Table 6-12 Doublet with varying fracture spacing- productivity index, improvement factor, thermal breakthrough time, geothermal lifetime and cumulative energy produced

Fracture spacing (m)	Average PI (L/bar-s)	Thermal breakthrough time - at 170 °C (year)	Geothermal lifetime - at 161 °C (year)	Cumulative energy per reservoir volume produced for 30 years (MJ/m^3)
10	1.95	15	29	34.47
100	1.84	0	0	30.23
1000	1.60	0	0	20.87

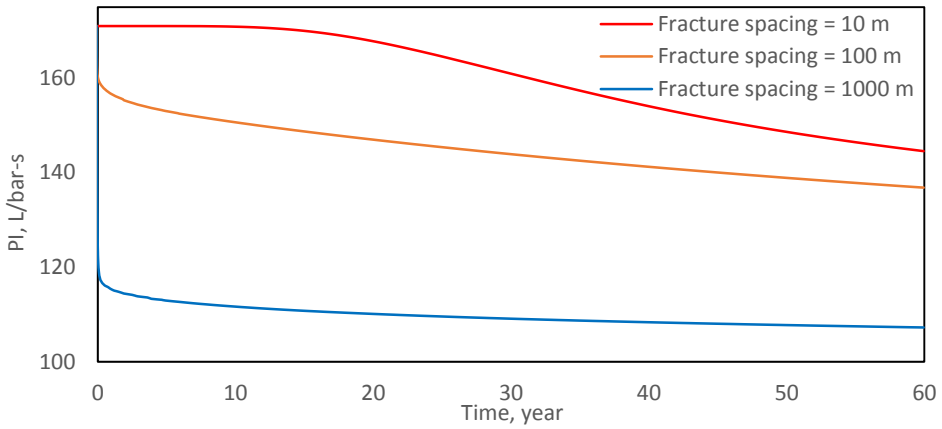

Figure 6-36 BHT at production well for the models with varying fracture spacing in Table 6-35 – doublet with the reservoir zone stimulated.

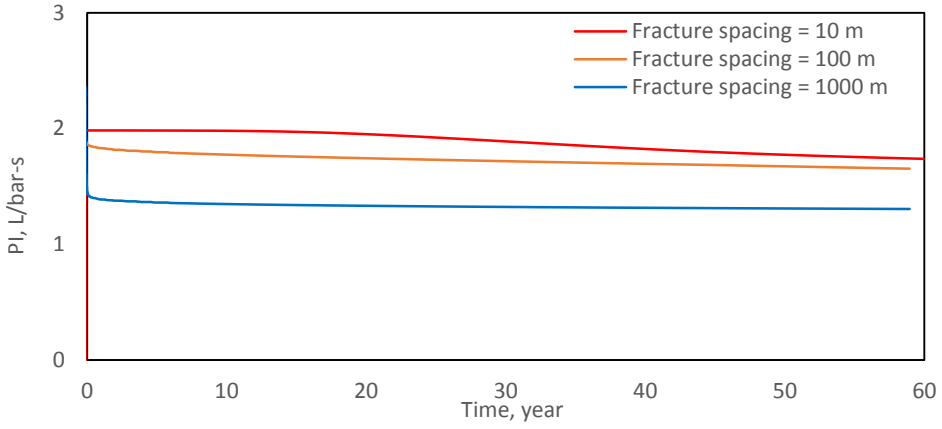

Figure 6-37 PI at production well for the models with varying fracture spacing in Table 6-35 – doublet with the reservoir zone stimulated.

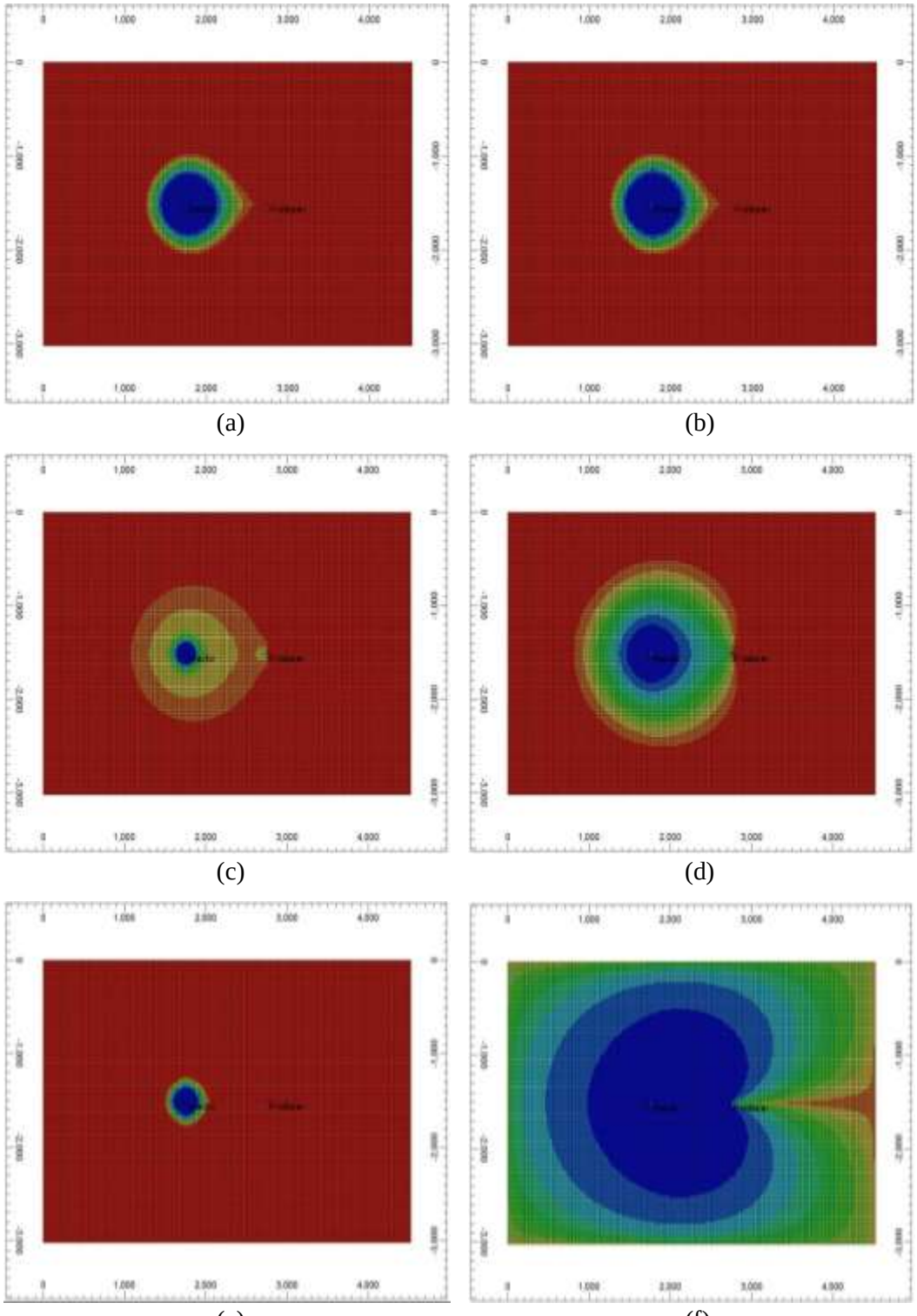

Figure 6-38 Doublet - comparison of the matrix temperature (left: (a), (c) and (e)) and the fracture temperature (right: (b), (d) and (f)) with a fracture spacing of 10, 100 and 1,000 after 15 years of production.

Table 6-13 Horizontal well with varying fracture spacing - productivity index, improvement factor, thermal breakthrough time, geothermal lifetime and cumulative energy produced

Fracture spacing (m)	Average PI (L/bar-s)	Thermal breakthrough time (at 170 °C) (year)	Geothermal lifetime (at 161 °C) (year)	Cumulative energy per reservoir volume produced for 30 years (MJ/m^3)
10	6.22	17	34	35.35
100	5.87	0	8	32.45
1000	4.93	0	0	28.55

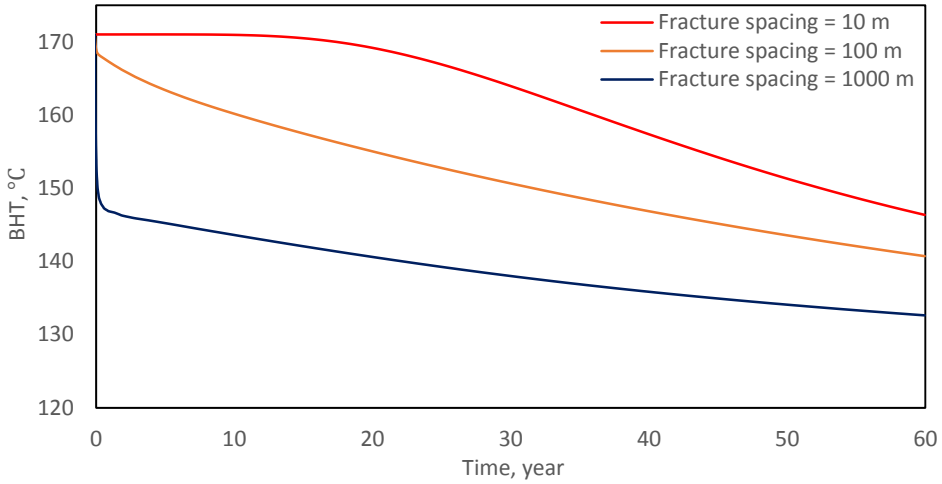

Figure 6-39 BHT at production well for the models with varying shape spacing in Table 6-35 – horizontal well with the reservoir zone stimulated.

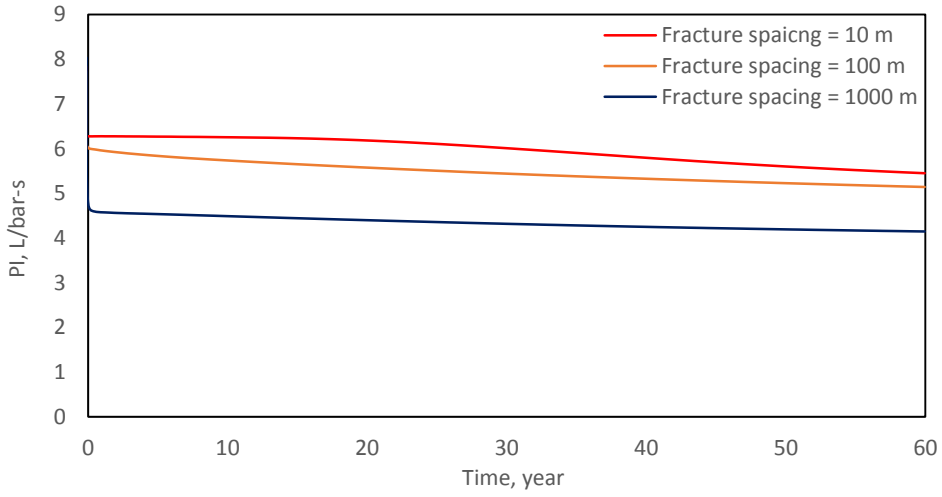

Figure 6-40 PI at production well for the models with varying fracture spacing in Table 6-35 – horizontal well with the reservoir zone stimulated.

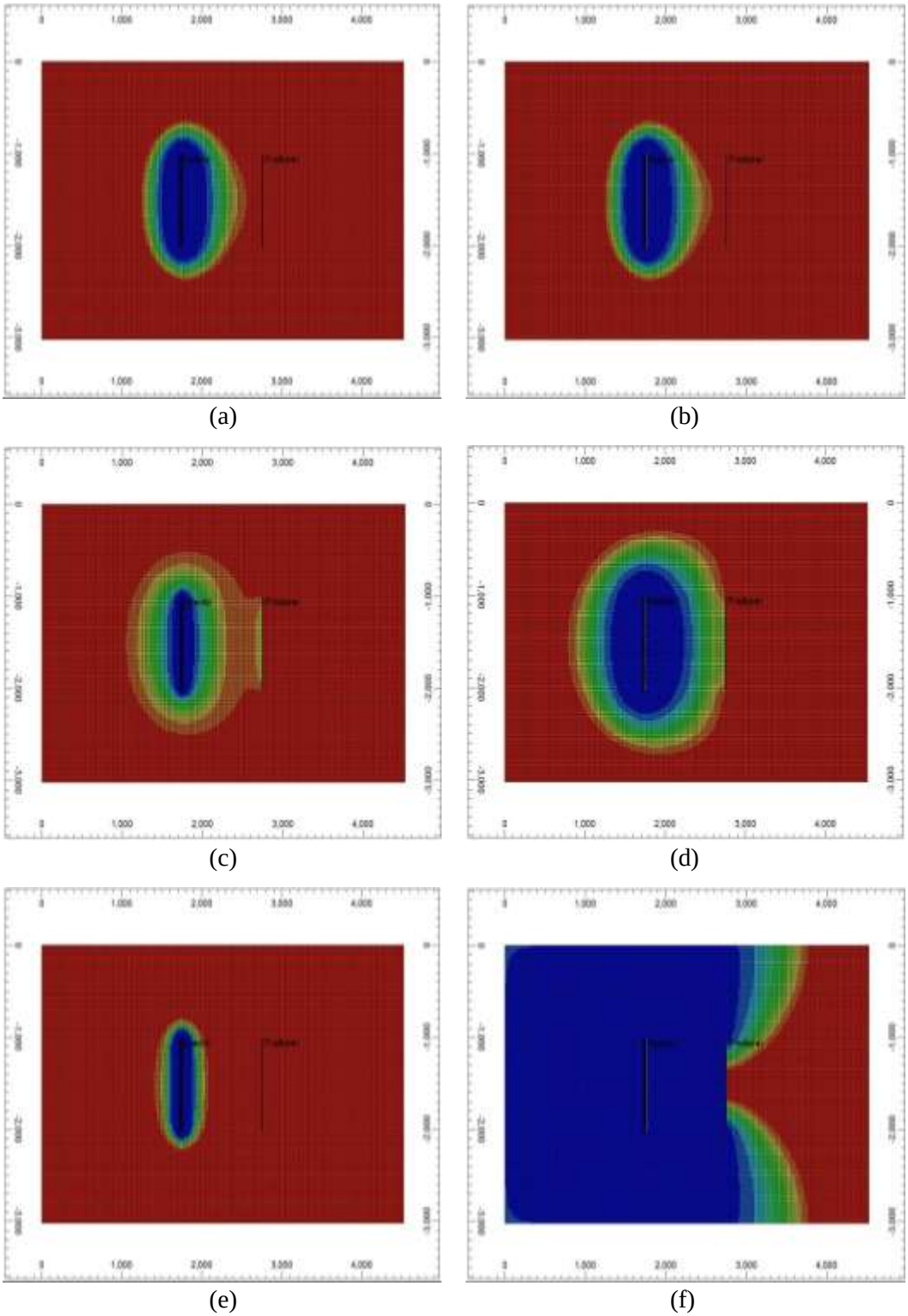

Figure 6-41 Horizontal well - comparison of the matrix temperature (left: (a), (c) and (e)) and the fracture temperature (right: (b), (d) and (f)) with a fracture spacing of 10, 100 and 1,000 after 15 years of production.

CHAPTER 7
CONCLUSION AND RECOMMENDATION

This chapter presents the conclusions of this study and recommendations for further research on geothermal reservoir development.

7.1 Conclusion

A list of conclusions made from this study is as follows,

- The Gringarten and Sauty's analytical solution is validated using a commercial thermal reservoir simulation. The numerical results are considerably affected by grid-block size, time step, and no-flow boundary effect. Especially, no-flow boundary effect significantly reduces thermal breakthrough time.
- The analytical tracer test model is validated using a numerical reservoir simulation. The correlation between thermal breakthrough time and water (tracer) breakthrough time in homogeneous and heterogeneous reservoirs is valid as long as water and rock properties are held constant.
- It is verified that heat conduction can be ignored when the dimensionless thermal Peclet number is much greater than unity for the given flow rate and reservoir parameters including heat capacity and thermal conductivity of typical rocks. This assumption is valid for typical geothermal reservoirs.
- Water density and viscosity as a function of temperature has a significant impact on thermal breakthrough time. The combined effect of temperature dependent properties of water results in a longer thermal breakthrough time. The analytical solution for predicting thermal breakthrough time can be used as a preliminary design criterion, which provides a conservative estimate.
- The target formation – the Permian Lyons sandstone formation in the Denver basin, is expected to have a favorable geothermal gradient based on the analysis of the borehole temperature data. The average productivity index in a 1,000 m well spacing doublet system is less than 0.75 L/bar-s, which is considered marginal or sub-marginal for the target flow rate (8068 m^3/day). Appropriate reservoir stimulation process could help overcome the low permeability of the target formation.
- Horizontal well and tensile fracturing which make the heat propagation linear between the wells help increase heat sweep efficiency, resulting in more heat energy produced for a given reservoir lifetime.

- It is shown that a significant amount of heat can be extracted from low permeability shale cap and bed rocks between the reservoir layers. This helps extending the thermal lifetime of geothermal reservoirs.
- It is crucial to strike a balance between hydraulic and thermal performance so that geothermal reservoirs are able to achieve the target flow rate and reliable operation for 30 years of lifetime. Particularly for an EGS in its strict term, engineered or naturally present fracture networks represented by fracture conductivity and shape factor in this study determines the reservoir performance.

7.2 Recommendations

- More detailed reservoir characterization for the target formation in connection with its geologic setting is required to estimate the reservoir drainage area as well as petrophysical properties
- Hydraulic fracturing scheme (i.e., water or gel-proppant treatment) in connection with stress regime in the target formation should be considered in the modeling work.
- THM (Thermal, hydraulic and mechanical) simulation will be more effective to evaluate the effects of natural or induced fractures on the reservoir performance.
- In addition to reservoir performance, parasitic energy consumption at production and injection wells and energy conversion efficiency of binary plants should be considered simultaneously to optimize the net electric power generation. Wellbore heat and pressure loss, pump performance curve and binary plant efficiency should be simulated for global optimization based on the target electric power generation.

LIST OF SYMBOLS

Symbol	Definition	Unit
Δt	Reservoir Lifetime	year
P	Pressure	kPa
D	Well distance	meter
h	Reservoir height	meter
Q	Flow rate	m^3/day
ρ	Density	kg/m^3
C	Heat Capacity	$kJ/kg/\,^{\circ}C$
μ	Viscosity	cp
k	Permeability	mD
$\emptyset$	Porosity	fraction
r_{well}	Well radius	meter
t	Time	year, day, second
T	Temperature	°C
$\vec{u}$	Darcy velocity	m/s
K	Thermal conductivity	W/m℃
κ	Thermal diffusivity	m^2/s
D_T	Retardation factor	dimensionless
t_T^{BT}	Thermal front breakthrough time	year
t_w^{BT}	Tracer(water) breakthrough time	year
G_P	Electric geothermal potential	MW_e
H_G	In place enthalpy	MJ

t_E	A period of commercial power generation	second
V_B	Reservoir rock volume	m^3
σ_p	Gilman and Kazemi shape factor	$1/m^2$
σ_T	Thermal transmissibility in the fracture-matrix conductive flow	m^3/s
L_i	Fracture spacing	meter
L_{fi}	Fracture width	meter
L_{mi}	Matrix size	meter
F_f	Fraction of fracture volume	dimensionless
$\emptyset_f$	Fracture porosity	dimensionless
$\emptyset_{f,eff}$	Effective fracture porosity	dimensionless
Subscript β	Phase	-
λ	Mobility	1/cp
x	Mole fraction	dimensionless
H	Enthalpy	Joule
U	Internal energy	Joule

REFERENCES CITED

Allis, R. Moore, J., Blackett, R.E., Gwynn, M., Kirby, S. and Sprinkel, D. 2011. The potential for basin-centered geothermal resources in the Great Basin. Geothermal Resources Council Transactions, Vol. 35.

Bjelm, L. and Alm, P-G. 2001. Reservoir Cooling After 25 Years of Heat Production in the Lund Geothermal Heat Pump Project. Proceedings, World Geothermal Congress 2010, Bali, Indonesia, 25-29 April.

Bundschuh, J. and Arriaga, M.C.S. 2010. Introduction to the Numerical Modeling of Groundwater and Geothermal Systems – Fundamentals of Mass, Energy and Solute Transport in Poroelastic Rocks, CRC Press, Taylor and Francis Group.

Butler, S.J., Sanyal, S.K. and Robertson-Tait, A. 2004. A numerical simulation study of the performance of enhanced geothermal systems. Proceedings, Twenty-ninth Workshop on Geothermal Reservoir Engineering, Stanford University, January, 2004.

Carslaw, H.S. and Jaeger, J.C. 1959. Conduction in Heat in Solids, 2nd ed., p. 396, Clarendon, Oxford.

Cheon, D. and Lee, T.J. 2013. Theoretical background and design of hydraulic fracturing in oil and gas production. Tunnel and underground space Vol. 23, No. 6, 2013, pp. 538-546

CMG. 2013. User's Guide of STARS: Advanced Process and Thermal Reservoir Simulator Version 2013. Computer Modeling Group Ltd. Calgary, Alberta, Canada.

CMG. 2013. Creating Models with Builder's Geological Modeling and Geostatistical Tools using Builder and IMEX. Computer Modeling Group Ltd. Calgary, Alberta, Canada.

Debra, K.H. and Dave, O.C. 2007. Oil and gas exploration and development along the Front Range in the Denver Basin of Colorado, Nebraska and Wyoming. U.S. Geological Survey Digital Data Series DDS-69-P.

Deo, M., Roehner, R., Allis, R. and Moore, J. 2013. Reservoir modeling of geothermal energy production from stratigraphic reservoirs in the Great Basin. Proceedings, Thirty-Eighth Workshop on Geothermal Reservoir Engineering Stanford University, Stanford, California, February 11-13, 2013 SGP-TR-198.

Du, C., Zhang, X., Zhan, L., Gu, H., Hay, B., Tushingham, K. and Ma, Y. 2010. Modeling hydraulic fracturing induced fracture networks in shale gas reservoirs as a dual porosity system. Paper SPE-131280 presented at the CPS/SPE International Oil and Gas Conference and Exhibition, Beijing, June 8-10.

Gringarten, A.C. and Sauty, J.P. 1975. A theoretical study of heat extraction from aquifers with uniform regional flow. Journal of Geophysical Research Vol. 80, No. 35.

Gringarten, A.C. 1978. Reservoir lifetime and heat extraction recovery factor in geothermal aquifers used for urban heating. Pageoph, Vol. 117.

Jung, R. 2013. EGS – Goodbye or back to the future. Proceedings of the International Conference for Effective and Sustainable Hydraulic fracturing. Brisbane, Australia.

Meyer, H.J. and McGee, H.W. 1985. Oil and gas fields accompanied by geothermal anomalies in Rocky Mountain region: American Association of Petroleum Geologists Bulletin, v. 69, p. 933-945.

MIT. 2006. The future of geothermal energy – Impact of enhanced geothermal systems (EGS) on the United States in the 21th century. An assessment by an MIT-led interdisciplinary panel, Massachusetts Institute of Technology, https://mitei.mit.edu/system/files/geothermal-energy-full.pdf.

Morgan, P. 2009. A Preliminary Analysis of Geothermal Resources in the Central Raton Bain, Colorado, from Bottom-Hole Temperature Data. GRC Transactions, Vol. 33.

Muskat, M. 1946. The flow of homogeneous fluids through porous media. J. W. Edwards, Inc., Ann Arbor, Michigan, 507-617.

Porro, C. and Augustine, C. 2012. An estimate of the geothermal energy resource in the major sedimentary basins in the United States. GRC Transactions, Vol. 36, 2012.

Romero, R. 2014. Lyons Sandstone Denver Basin, http:www.beg.utexas.edu/environqlty/co2seq/co2data/0lyons.htm (accessed 25 October 2014).

Sanyal, S.K., Morrow, J.W. and Butler, S.J. 2007. Net Power Capacity of Geothermal Wells versus Reservoir Temperature – A Practical Perspective. Proceedings, Thirty-Second Workshop on Geothermal Reservoir Engineering Stanford University, Stanford, California, January 22-24, 2007.

Satman, A. 2011. Sustainability of Geothermal Doublets. Proceedings, Thirty-Sixth Workshop on Geothermal Reservoir Engineering Stanford University, California, January 31 – February 2, 2011 SGP-TR-191.

Shook, G.M. 2001. Prediction of thermal breakthrough in heterogeneous media from tracer tests. Geothermics, 30 573-589.

Suarez, M.C. and Viggiano, J.L. 1992. Recovery factors and unused energy in a fractured reservoir. Proceedings International Conference on Industrial uses of Geothermal Energy, Reykjavik, Iceland.

Taylor, R.S., Stobo, B., Niebergall, G., Aguilera, R., Walter, J. and Hards, E. 2014. Optimization of Duvernay Fracturing Treatment Design Using Fully Compositional Dual Permeability Numerical Reservoir Simulation. Paper SPE-171602 presented at the SPE/CSUR Unconventional Resources Conference, Calgary, Alberta, Canada, September 30 – October 2.

APPENDIX A

Estimation of geothermal gradient

Bottomhole temperature data from well log headers are compiled and analyzed in order to estimate geothermal gradient of the area. There are a lot of different methods for correcting the temperature disturbance in association with the circulation of drilling fluid, the same approach Morgan (2009) has in his analysis of the Raton basin is used in this study.

The correction temperature,

$$T_{corrl} = -16.51213476 + 0.01826842109z - 0.000002344936959z^2 \quad \text{(A1)}$$

Intermediate corrected temperature,

$$T_{\text{int}} = BHT + T_{corrl} \quad \text{(A2)}$$

Second correction,

$$T_{corr2} = ((1.361609905ABG) - 33.21973078),$$
where ABG is the average geothermal gradient 46 °C/km for the Wattenberg field. (A3)

Final corrected temperature,

$$T_{final} = T_{\text{int}} + T_{corr2} \quad \text{(A4)}$$

Ground surface temperature,

$$T_{GST} = 23.69 - 0.005019Elev^n \quad \text{(A5)}$$

Geothermal gradient,

$$Grad = 1000(T_{final} - T_{GST}) / z_{BHT} \quad \text{(A5)}$$

Table A-1 Geothermal gradient estimated using bottomhole temperature recorded in log headers in the area of study in the Wattenberg field

Well	GL (m)	Log Depth (m)	Temp (°C)	T_{corrl} (°C)	T_{int} (°C)	T_{corr2} (°C)	T_{final} (°C)	T_{GST} (°C)	G_{rad} (°C/km)
1	2754	2754	103	49	152	30	182	10	63
2	1577	3458	152	52	203	30	233	16	63
3	1531	3119	121	51	171	30	201	16	59
4	1465	3049	111	50	162	30	191	16	57
5	1472	2940	112	50	162	30	192	16	60
6	1539	3199	126	51	177	30	206	16	60
7	1434	2823	107	49	156	30	186	16	60
8	1439	3025	154	50	205	30	235	16	72
9	2092	2846	135	50	185	30	214	13	71
10	1433	2743	85	49	134	30	164	16	54
11	1492	2846	136	50	185	30	215	16	70
12	1413	3192	164	51	215	30	245	17	72
13	1423	2651	133	48	182	30	212	17	74
14	1427	3175	142	51	193	30	223	17	65
15	2965	2965	129	50	180	30	208	9	77
16	1540	3087	156	51	206	30	236	16	71
17	1431	2404	95	47	142	30	172	17	65
18	1474	2623	102	48	151	30	180	16	63
19	1732	3104	91	51	142	30	172	15	50
20	1801	3373	103	51	155	30	185	15	50
21	1472	2673	104	49	152	30	182	16	62
22	1383	2504	113	48	160	30	190	17	69
23	1582	2198	78	45	123	30	153	16	62
24	1430	2530	95	48	143	30	173	17	62
25	1335	2511	96	48	143	30	173	17	62
26	1535	2392	84	47	131	30	161	16	60
27	1538	2447	95	47	142	30	172	16	64

APPENDIX B

Formulation of dual permeability (CMG User's guide, 2013)

The Gilman and Kazemi shape factor,

$$\sigma_p = 4V_b \sum_i \frac{\text{kmi,eff}}{L_i^2} \tag{B1}$$

Thermal transmissibility in the fracture-matrix conductive flow,

$$1/\sigma_T = \left[\sum_i \frac{L_{fi}}{A_{mi}\kappa_f} + \frac{L_{mi}}{A_{mi}\kappa_m} \right] \frac{V}{4V_b} \tag{B2}$$

Fracture and matrix width,

$$\begin{aligned} L_{fi} &= L_i \times \left[1-(1-F_f)\right]^{1/b} \\ L_{mi} &= L_i - L_{fi} \end{aligned} \tag{B3}$$

Porosity,

$$\begin{aligned} F_f &= V_f / V \\ \phi_{f,eff} &= \phi_f F_f \end{aligned} \tag{B4}$$

Dual permeability formulation is,

$$\text{fracture-fracture flow} = \sum_{\beta=1}^{n} \left[\Delta \left[T\rho_\beta \lambda_\beta x_{\beta,ic} (\Delta p + \Delta p_c - \gamma_\beta \Delta z) \right]_f \right]$$

$$\text{fracture-matrix flow} = \sigma \rho_\beta \lambda_\beta x_{\beta,ic} \Delta \phi_{fm}$$

$$\text{matrix-matrix fluid flow} = \sum_{\beta=1}^{n} \Delta \left[T\rho_\beta \lambda_\beta x_{\beta,ic} (\Delta p + \Delta p_c - \gamma_\beta \Delta z) \right]$$

$$\text{matrix-matrix heat flow} = \sum_{\beta=1}^{n} \Delta \left[T\rho_\beta \lambda_\beta H_{\beta,ic} (\Delta p + \Delta p_c - \gamma_\beta \Delta z) \right] + \Delta \left[T_c \Delta T \right]$$

$$\text{accumulation} = \left[\frac{V}{\Delta t} \Delta_t \sum_{\beta=1}^{n} \phi \rho_\beta S_\beta x_{\beta,ic} - q \right]_f$$

source/sink = q

Mass balance in fracture,

$$\sum\left[\text{fracture-fracture flow}\right]+\text{fracture-matrix flow} = \left[\text{accumulation - sink/source}\right]_f$$

$$\sum_{\beta=1}^{n}\left[\Delta\left[T\rho_\beta\lambda_\beta x_{\beta,ic}(\Delta p+\Delta p_c-\gamma_\beta\Delta z)\right]_f\right]+\sigma\rho_\beta\lambda_\beta x_{\beta,ic}\Delta\phi_{fm}=\left[\frac{V}{\Delta t}\Delta_t\sum_{\beta=1}^{n}\phi\rho_\beta S_\beta x_{\beta,ic}-q\right]_f \tag{B5}$$

Mass balance in matrix,

$$[\text{matrix-matrix flow}] - \sum\left[\text{fracture-matrix flow}\right] = \left[\text{accumulation - sink/source}\right]_f$$

$$\sum_{\beta=1}^{n}\Delta\left[T\rho_\beta\lambda_\beta x_{\beta,ic}(\Delta p+\Delta p_c-\gamma_\beta\Delta z)\right]-\sum_{\beta=1}^{n}\sigma_p\rho_\beta\lambda_\beta x_{\beta,ic}\Delta\phi_{fm}=\left[\frac{V}{\Delta t}\Delta_t\sum_{\beta=1}^{n}\phi\rho_\beta S_\beta x_{\beta,ic}-q\right]_f \tag{B6}$$

Energy balance in fracture,

$$\begin{aligned}&\sum\left[\text{fracture-fracture heat flow}\right]+\text{fracture heat conduction}+\sum\left[\text{fracture-matrix heat flow}\right]\\&=\left[\text{fluid accumulation + rock accumulation}\right]_f-\text{sink/source}\\&\sum_{\beta=1}^{n}\Delta\left[T\rho_\beta\lambda_\beta H_\beta(\Delta p+\Delta p_c-\gamma_\beta\Delta z)\right]_f+\Delta[T_c\Delta T]_f+\sum_{\beta=1}^{n}\sigma_p\rho_\beta\lambda_\beta x_{\beta,ic}\Delta\phi_{fm}+\sigma_T\Delta T_{fm}\\&=\left[\frac{V}{\Delta t}\Delta_t\sum_{\beta=1}^{n}\phi\rho_\beta S_\beta U_\beta+(1-\phi)\rho_r c_{pr}(T-T_r)\right]_f-qu\end{aligned} \tag{B7}$$

Energy balance in matrix,

$$\begin{aligned}&\left[\text{matrix-matrix heat flow}\right]-\sum\left[\text{fracture-matrix heat flow}\right]\\&=\left[\text{fluid accumulation + rock accumulation}\right]_m-\text{sink/source}\\&\sum_{\beta=1}^{n}\Delta\left[T\rho_\beta\lambda_\beta H_{\beta,ic}(\Delta p+\Delta p_c-\gamma_\beta\Delta z)\right]+\Delta\left[T_c\Delta T\right]+\sum_{\beta=1}^{n}\sigma_p\rho_\beta\lambda_\beta x_{\beta,ic}\Delta\phi_{fm}+\sigma_T\Delta T_{fm}\\&=\left[\frac{V}{\Delta t}\Delta_t\sum_{\beta=1}^{n}\phi\rho_\beta S_\beta U_\beta+(1-\phi)\rho_r c_{pr}(T-T_r)\right]_f-qu\end{aligned} \tag{B8}$$